UNRAVELLING THE MECHANISMS OF EXCITON TRANSPORT IN NATURAL LIGHT HARVESTING SYSTEMS

by

Katherine Parsons

Submitted in partial fulfillment of the requirements
for the degree of Master of Science

at

Dalhousie University
Halifax, Nova Scotia
Aug 2021

Table of Contents

List of Tables

List of Figures

List of Abbreviations and Symbols

LHCII	Light Harvesting Complex II
CP	Chlorophyll Protein
FMO	Fenna-Matthews-Olson
FBTS	Forward-Backward Trajectory Solution
HEOM	Hierarchical Equations of Motion
MT model	Mutant-type model
TD model	Tangent-dipole model
PD model	Parallel-dipole model
NN model	Nearest-neighbour model
MSD	Mean Squared Displacement
ps	Picosecond
Δ	Difference
cm^{-1}	Wavenumber Unit
Å	Angstrom
K	Kelvin
t	Time
U	Exciton Population
T	Temperature
λ	Reorganization energy
ω_c	Characteristic bath frequency

Abstract

Photosynthetic organisms contain light harvesting complexes comprised of pigments that absorb sunlight as electronic excitations. In this work, the transfer of this excitation energy in four natural light harvesting complexes is investigated; specifically, LHCII and CP26 from higher plants, along with FMO and the chlorosome from Green Sulfur Bacteria. For the LHCII, CP26, and FMO complexes, the mechanistic details from two different starting locations for the initial excitation at two temperatures were extracted and discussed. In order to study the transport through the chlorosome, natural and artificial nanotublar models were constructed to represent the arrangement of the pigments and details about the spread of the exciton are analyzed. This was all facilitated through the application of the approximate quantum-classical method known as the forward-backward trajectory solution (FBTS).

Acknowledgements

I would like to express my gratitude for my family. It was through their encouragement over these past years that has provided me the chance to see this work to completion. I would like to thank my friends for being great listeners and for their support. Finally, a special acknowledgement for my supervisor, Aaron Kelly, who helped me along this path and taught me so much.

Chapter 1

Introduction

1.1 Initial Steps of Photosynthesis

Organisms use the process of photosynthesis to convert the sun's energy into chemical energy [2, 3]. Figure 1.1 depicts the steps that initiate this essential process: the collection, transportation and capture of sunlight [1]. All of these steps are facilitated by pigment molecules. The sun's energy is harvested by pigments when it is absorbed, such that an electron is promoted to an excited state. Thus, the sun's energy has been transformed into excitation energy. This excitation energy must then be transported through an aggregation of pigments, known as light harvesting complexes, to the reaction center to cause charge separation which will power the subsequent steps of photosynthesis.

Between plants, algae, and bacteria there exists a diverse range of life and environments in which this photosynthetic apparatus responsible for these initial steps must efficiently operate [3]. This middle step, the excitation energy transfer, must be effective enough to deliver the energy to the required destination for the rest of the process of photosynthesis to proceed and much time has been dedicated to the investigation of the structure and the function behind these initial steps [4–8].
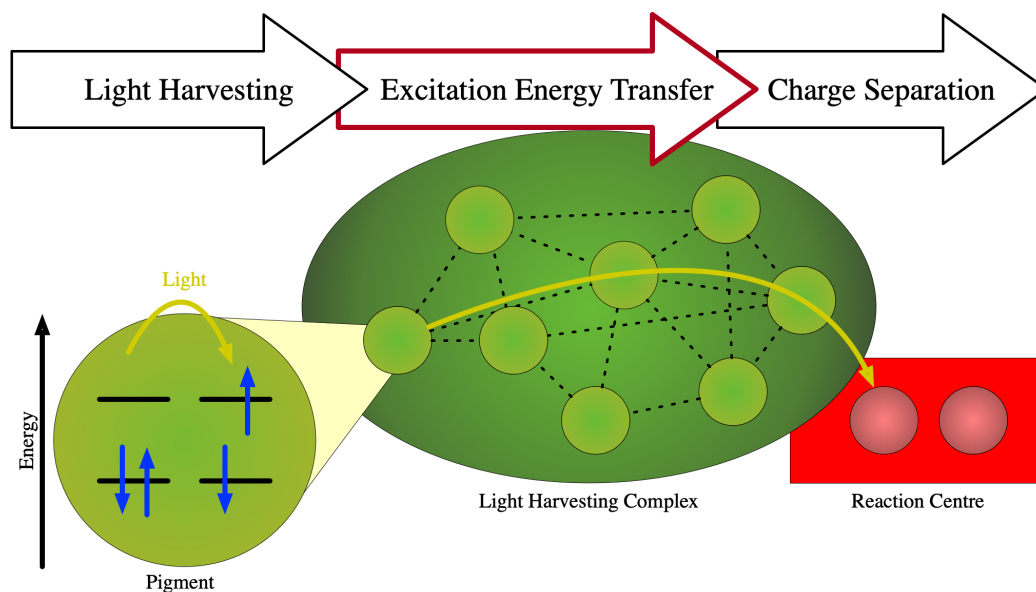
Figure 1.1: A basic overview of the initial steps of photosynthesis, wherein the sunlight is collected, transported and trapped [1]. The excitation energy transfer step will be the focus of this research.

1.2 Photosynthetic Pigments

The sun emits a wide range of wavelengths of light and the structure of the pigment molecule informs what parts of the spectrum will be absorbed [2,3]. An example of the chemical structure of a photosynthetic pigment is provided on the right of Figure 1.2. This is the structure of chlorophyll A, a major pigment found in higher plants and the cyclic tetrapyrrole is the structural foundation of the main pigments involved in the initial steps of the process of photosynthesis [3]. Additional photosynthetic pigments with distinct structural types are phycobilins and caroteniods; wherein caroteniods are also found in higher plants and assist in the dissipation of excess energy, without which detrimental effects such as the creation of singlet oxygen can occur [9].

The corresponding absorption spectrum for this molecule is provided on the left of Figure 1.2, which reveals that the significant peaks are located at approximately 430nm and 680nm, supporting the connection to higher plants. The lowest energy excitation at 680nm is in the Q_y direction as illustrated on the structure of chlorophyll A [10]. By altering the substituents on the ring and chain, this will result in different main photosynthetic pigments with different absorption spectra, such as

bacteriochlorophylls [9].
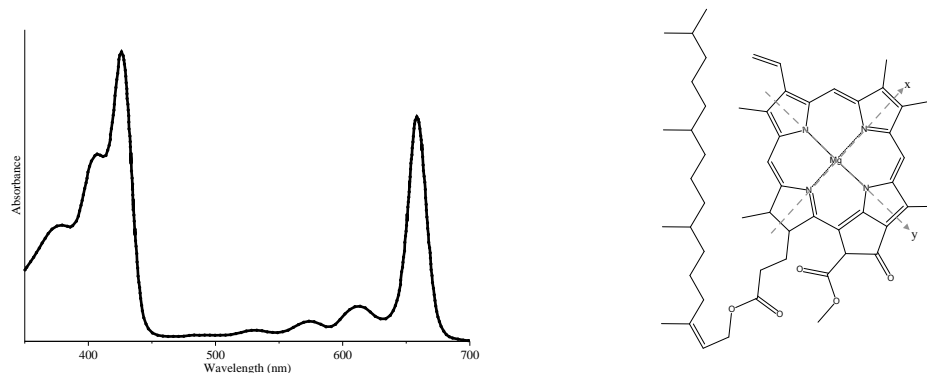
Figure 1.2: On the left is an absorption spectra adapted from Ref. [11] of chlorophyll A in diethyl ether. The structure on the right depicts chlorophyll A and the major peak that has the longest wavelength corresponds to the electronic transition along the y directional arrow as indicated on the structure [10].

These photosynthetic pigments must collect, but also transport, the excitation energy and this is achieved through the electronic coupling between neighbouring transition dipoles [6]. A significant coupling between pigments will result in the excitation energy being shared and a more general term to refer to this energy is implemented in this instance. An exciton, an electron-hole pair, can be delocalized and shared other many pigments when the strength of the coupling is strong, as compared to the strength of the coupling with the environment, that will destroy this delocalization [7].

1.3   Light Harvesting Complexes

A collection of pigments are situated in specific structural arrangements and an understanding of the spatial organization is important to the excitation energy transfer. There are two levels of this organization to consider, the first being that of an isolated light harvesting complex like the one provided in Figure 1.3, which depicts a crystal structure of a complex from higher plants called LHCII [12]. This structure reveals the location of each pigment, wherein the two types of pigments are delineated by the colours black (chlorophyll B) and red (chlorophyll A), with the surrounding protein as the light grey structure. Each pigment not only occupies a certain space but is also

arranged in a specific orientation, all facilitated by the protein. Additional crystal structures of light harvesting complexes illustrate pigments organized by a protein scaffold; [12–14] this is a common feature for natural light harvesting complexes [3]. This figure provides a sense of the spatial landscape as constructed by the protein for which the excitation energy transfer by the pigments will occur but the energetic landscape is also affected by the protein. This is because the protein environment will affect the electronic coupling and the absorption of the pigments, [15, 16] while also destroying the delocalization of the exciton.
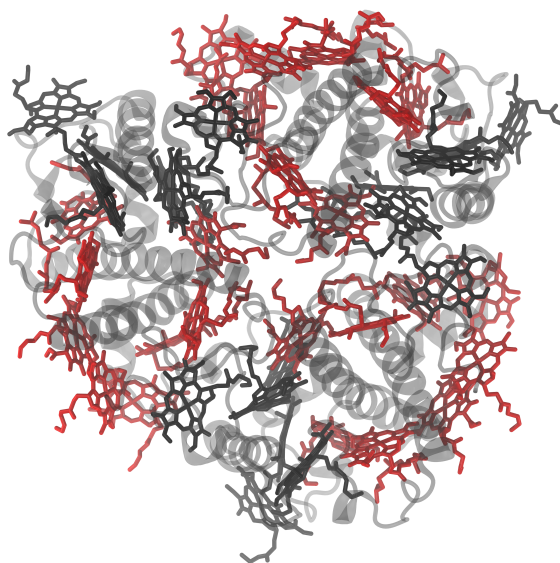
Figure 1.3: Structure of the light harvesting complex known as LHCII. The pigments are coloured black and red, corresponding to chlorophyll B and chlorophyll A, respectively and the protein is rendered in gray. From structure 3jcu in the protein data bank [12].

The surrounding environment has a large impact on the dynamics of excitation energy transfer. An environment that is further complicated by the knowledge of the larger organization of the pigments, that of the photosynthetic unit. A photosynthetic unit refers to the apparatus in which the initial steps of photosynthesis occurs, it is composed of multiple light harvesting complexes around a reaction center [9]. These units can be comprised of different light harvesting complexes and can change structure depending on external environmental conditions [12, 17]. There is a large variety of spatial and energetic landscapes between the photosynthetic organisms for which excitation energy transfer must occur.

1.4   Excitation energy transfer

There are two important interactions to consider in excitation energy transfer, the interactions between the pigments and the interactions with the surrounding environment, most notably the protein scaffold. This will affect substantially how the energy will be transferred. Two opposing ways in which the exciton moves through the light harvesting complex is either discretely, as in localized on a pigment, or fully delocalized, in which the energy is transferred between exciton states that are composed of contributions from multiple pigments [18]. These conditions for the mechanism of transfer will occur when considering the magnitudes of the electronic coupling between the pigments, which will cause the exciton to be shared and delocalized or, coupling between the pigment and the environment, which will inhibit the length of this delocalization and if strong enough localize the excitation energy on a single pigment. Thus, the motion of the exciton can be incoherent, hopping-type, transport versus coherent, flow-type, transport through the complex.

There are already two methods which can effectively calculate the hopping or flow-type motion of the exciton. These are Förster theory, [19] which describes the rate of transfer from one pigment to the next and Redfield theory, [20,21] which describes the rate of transfer from one exciton state to the next. Both of these theories have been applied to the excitation energy transfer in light harvesting complexes and both are fundamentally based on the two perturbative limits, either when the pigment-pigment coupling is small or pigment-environment coupling is small, respectively [22–26].

It is well established that in the large variety of photosynthetic units the excitation energy transfer occurs in an intermediate regime between the ratio of these two energy scales [6, 27]. This complicates the dynamics and brings a challenge to the methods employed for the study of excitation energy transfer. Even these seminal methods have been improved upon and combined together in order to better capture the dynamics in these regimes; in a real system such as the LHCII light harvesting complex there are pigments strongly coupled, where coherent transfer will occur and instances of weakly coupled pigments, like those pigments between monomers, where incoherent hopping occurs [22,26]. It is important to have a method that can simulate in all regimes of the system. One such method is the Hierarchical Equations of Motion

(HEOM), [25, 28, 29] that is numerically exact but can be prohibitive for larger systems. In this research we use an approximate mixed quantum-classical method called the Forward-Backward Trajectory Solution [30, 31] in order to investigate systems of various sizes and regimes.

1.5 Thesis Objectives

The scope of this thesis encompasses only the excitation energy transfer process of the primary steps of photosynthesis. An explicit focus is placed on isolated natural light harvesting complexes, such that there will not be the presence of a reaction centre to act as a sink for the energy, nor the addition of neighbouring complexes, as in the larger photosynthetic apparatus. Four natural light harvesting complexes are studied, sourced from two distinctive classes of organisms and covering a range of sizes. In this thesis we aim to address basic characteristics of the excitation energy transfer in these complexes.

A mixed quantum-classical dynamics method called the forward-backward trajectory solution (FBTS) is explained in Chapter 2 and was utilized to simulate the excitation energy transfer. The simple exciton dimer model, explored in Chapter 3, is the first example of the application of the FBTS method and serves to assist in supplying a deeper level of comprehension on how the various parameters of the system will affect the dynamics. The exciton dimer model also provides the opportunity to comment on the level of accuracy from the FBTS method through a comparison to results from the literature.

In Chapter 4, two isolated light harvesting complexes were chosen for study from higher plants: light harvesting complex II (LHCII) and chlorophyll protein 26 (CP26). In Chapter 5 two light harvesting complexes from bacteria are studied: the Fenna-Matthews-Olson (FMO) complex and the chlorosome, wherein, FMO is the smallest natural light harvesting complex investigated and the chlorosome is the largest. A discussion of the structure of these complexes is provided, containing only the main pigments involved, in order to supply a picture of the spatial and energetic landscape for which the excitation energy will travel. For the light harvesting complexes LHCII, CP26 and FMO there exists a crystal structure to provide the structural details. For the chlorosome, representative models of the structure were constructed with the

assistance of a collaboration with Dr. Luca Celardo.

All natural light harvesting complexes were studied with an initial excitation on a single site in the system. In this thesis the light harvesting complexes LHCII, CP26, and FMO were studied with two different initial conditions at two temperatures; this allowed for not only the mechanism of transfer to be determined but also to observe how the flow of energy changed. For the chlorosome the spread the excitation energy transfer was compared between the models, in order to ascertain which would be the most effective. This thesis serves to demonstrate that the FBTS method can provide a balance between accuracy and computational cost in order to provide mechanistic insights into the excitation energy transfer in a variety of isolated natural light harvesting complexes and form a foundation for further applications.

Chapter 2

Theoretical Background

An outline of the implementation of the forward-backward trajectory solution (FBTS) is provided in this chapter. The first section is a description of the Frenkel exciton model used to represent the light harvesting complexes. This model has precedence in the literature for the study of excitation energy transfer [24,25,28]. The following section will outline how the FBTS method can be used to calculate relevant observables. Specifically, the population of the exciton, which can be used to gain an understanding of the mechanism of transport through these constructed models. Details of the exact systems analyzed in this thesis will be given in subsequent chapters.

2.1 Construction of the Frenkel Exciton Model

In the Frenkel exciton model the total system is partitioned into a subsystem of interest and a bath or environment to capture all additional details. This is summarized in equation 2.1, where there are components to represent the subsystem $\hat{H}_s$, the bath $\hat{H}_b$, and the coupling between the two, $\hat{H}_{sb}$. The quantity $\hat{h}$ contains the components that have to do with the subsystem and is defined as the combination of the subsystem and the subsystem-bath Hamiltonians. The subsystem will be treated quantum mechanically and the bath will be treated classically; the subsystem-bath Hamiltonian contains how the bath influences the dynamics of the subsystem.

$$\hat{H}_{\text{total}} = \hat{H}_s + \hat{H}_b + \hat{H}_{sb} = \hat{h} + \hat{H}_b. \tag{2.1}$$

In this thesis the systems under study are isolated natural light harvesting complexes; on the left of Figure 2.1 one such example known as the Fenna-Matthews-Olson (FMO) complex is depicted (the real-time dynamics of which will be explored in Chapter 5). This picture is complex and a focused is placed on the pigments which are the most relevant degrees of freedom for the transportation of the excitation energy. Therefore, in the central picture the protein scaffold is removed. However, even

the pigments will be further simplified; such that the subsystem will only contain the S_0 to S_1 electronic transition for the pigment that corresponds to the Q_y transition [28]. The right of Figure 2.1 contains the degrees of freedom that will constitute the subsystem Hamiltonian which will be treated quantum mechanically.
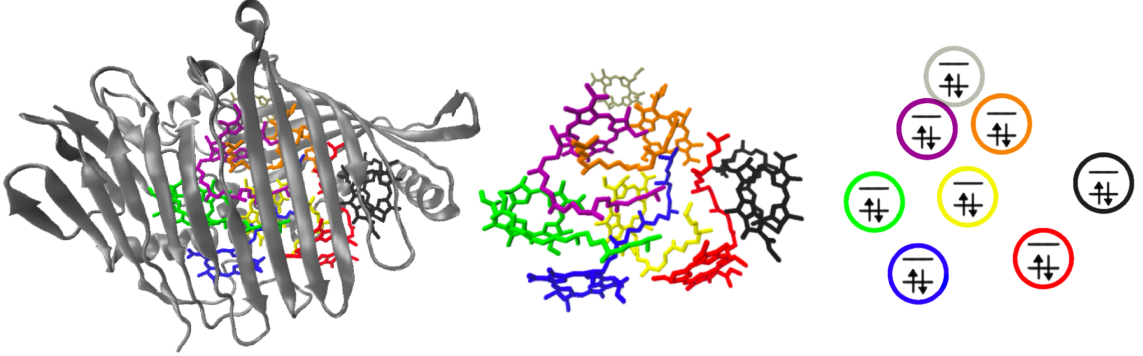
Figure 2.1: This figure, from left to right, serves to illustrate how the subsystem of interest in the Frenkel exciton model is obtained from a natural light harvesting complex. Shown on the left is FMO, complete with a protein (rendered in grey) and pigments (the coloured structures). Next the protein scaffold has been stripped away to reveal only the pigments, wherein on the left each pigment is finally simplified as a two level electronic transition.

Through the utilisation of the site basis, $|i\rangle$ that describes a collection of $i,....,N$ total pigments wherein only site i is excited, the subsystem Hamiltonian can be written as equation 2.2. The difference between the two-level system that describes each pigment is referred to as the site energy, ϵ. The electronic coupling, J_{ij}, connects site i and j together facilitating the transport of the exciton through the system.

$$\hat{H}_s = \sum_{i=1}^{N} \epsilon_i |i\rangle\langle i| + \sum_{i\neq j}^{N} J_{ij} |i\rangle\langle j|, \tag{2.2}$$

All other surrounding degrees of freedom are captured in the environment or bath and are represented as a collection of K harmonic oscillators. What constitutes this bath can be consider as the vibrational modes that were stripped away from Figure 2.1, such as the surrounding protein and the atoms constituting the pigments. Each of the κth harmonic oscillators are described by a particular position, R, momentum, P, and frequency, ω [32]. Equation 2.3 contains the bath Hamiltonian:

$$\hat{H}_b = \frac{1}{2} \sum_{i=1}^{N} \sum_{\kappa=1}^{K} \left(\hat{P}_{i,\kappa}^2 + \omega_{i,\kappa}^2 \hat{R}_{i,\kappa}^2 \right) \tag{2.3}$$

Lastly, the third component of the total system Hamiltonian, the subsystem-bath coupling, is provided in equation 2.4 and encapsulates how the bath will affect the dynamics of the subsystem. In this model each site experiences and interacts with an independent and linear bath. We introduce the variable $c_{i,\kappa}$ as the coupling constant and represents the strength of each harmonic oscillator on a site i.

$$\hat{H}_{sb} = - \sum_{i=1}^{N} \sum_{\kappa=1}^{K} c_{i,\kappa} \hat{R}_{i,\kappa} |i\rangle\langle i| \tag{2.4}$$

Information about the coupling constant is contained in the spectral density, $(J(\omega))$, the equation for which is provided in 2.5. Both experiment and theory can provide information on the spectral density, with methods such as difference fluorescence line spectroscopy [33] or through the employment of molecular dynamics simulations [34, 35]. For computational simulations, the spectral density has been captured realistically [36] or simplistically, using a function to model the spectral density [37]. In this thesis an approximate form is used, known as the Debye spectral density provided in equation 2.6 [38].

$$J(\omega) = \sum_{\kappa} c_{\kappa}^2 \delta(\omega - \omega_{\kappa}) \tag{2.5}$$

$$J_{\mathrm{D}}(\omega) = \frac{2\lambda\omega_c\omega}{\omega^2 + \omega_c^2} \tag{2.6}$$

The motivation for this form of the bath is to compare with literature results in the effort to benchmark this approximate method [25, 29]. The parameters that make up the Debye spectral density in equation 2.6, λ and ω_c are the reorganization energy and the characteristic frequency of the bath, respectively. The reorganization energy is a measure of the strength of the bath to the subsystem and the inverse of the characteristic frequency is related to the relaxation time of the bath [28, 39]. The coupling constants between each site and oscillator can be calculated using equation 2.7. The quantity, $\rho_D(\omega_{\kappa})$ is the density of frequencies, that for the simulations is made discrete and given a functional form with equations, 2.8 and 2.9, respectively. In this work ω_{max} is set equal to $\omega_{max} = 5\omega_c$.

$$c_{i,\kappa}^2 = \omega_\kappa \frac{2}{\pi} \frac{J_\mathrm{D}(\omega_\kappa)}{\rho_D(\omega_\kappa)} \tag{2.7}$$

$$\int_0^{\omega_\kappa} \rho_D(\omega)d\omega = \kappa, \kappa = 1, ..., K \tag{2.8}$$

$$\rho_D(\omega) = \frac{K}{2\sqrt{\omega\omega_\mathrm{max}}} \tag{2.9}$$

In summary each pigment is a two-level system with a particular site energy and coupling strength to the other pigments in the system. The bath is a collection of harmonic oscillators and the interaction of the bath with the subsystem is described by the Debye spectral density. Upon the application of the model as outlined above the relevant details about the complicated light harvesting systems can be captured and then studied. This model is highly simplified but is still useful since is can be linked to linear spectra which can be used to determine the parameters of these systems.

2.2 The Forward-Backward Trajectory Solution

2.2.1 Observables in Quantum Mechanics

An investigation into the real-time dynamics of the models outlined in the previous section will provide information into the excitation energy transfer in natural light harvesting systems. The quantum-classical liouville equation describes these dynamics [40, 41]. An approximate solution was developed by Hsieh and Kapral and was named after the form of the quantum-classical liouville equation used for the derivation [30,31,42]. This forward-backward trajectory solution (FBTS) is computationally efficient due to casting both subsystem and environmental degrees of freedom into a continuous phase space representation. This allows for the FBTS method to evolve an ensemble of Monte Carlo sampled trajectories according to classical-like equations of motion. The population of the exciton on a particular site is the observable of interest for this research and FBTS can be used to approximate the expectation value of a general time-dependent observable $\hat{B}(t)$, which is defined as the trace of the observable with the density matrix, ρ, of the system (as shown in equation 2.10).

$$\langle B(t) \rangle = \text{Tr}\left(\hat{B}(t)\hat{\rho} \right) \tag{2.10}$$

2.2.2 Continuous Phase Space Transformation

A primary element of the FBTS method is that both subsystem and environmental degrees of freedom evolve according to classical-like equations of motion [30, 31, 42]. The continuous variables that represent the bath degrees of freedom are, $X = (R,P) = (R_1,...R_K, P_1,...,P_K)$ and, as a consequence of this method, two sets of coherent state variables represent the subsystem degrees of freedom: $(x, x') = (q, p, q', p') = (q_1,...q_N, p_1,...,p_N, q'_1,...q'_N, p'_1,...,p'_N)$. The classical-like equations of motion for these variables are provided in equation 2.11, with the effective Hamiltonian, H_e given in equation 2.12.

$$
\begin{aligned}
\frac{dq_\mu}{dt} &= \frac{\partial H_e(X, x, x')}{\partial p_\mu}, \frac{dp_\mu}{dt} = -\frac{\partial H_e(X, x, x')}{\partial q_\mu}, \\
\frac{dq'_\mu}{dt} &= \frac{\partial H_e(X, x, x')}{\partial p'_\mu}, \frac{dp'_\mu}{dt} = -\frac{\partial H_e(X, x, x')}{\partial q'_\mu}, \\
\frac{dR}{dt} &= \frac{P}{M}, \frac{dP}{dt} = -\frac{\partial H_e(X, x, x')}{\partial R}
\end{aligned}
\tag{2.11}
$$

$$H_e(X, x, x') = H_b(R, P) + \frac{1}{2}\sum_{\lambda\lambda'} h^{\lambda\lambda'}(R)(q_\lambda q_{\lambda'} + p_\lambda p_{\lambda'} + q'_\lambda q'_{\lambda'} + p'_\lambda p'_{\lambda'}) \tag{2.12}$$

The subsystem degrees of freedom are cast into a continuous phase space with a mapping representation [43]. A particular state $|\lambda\rangle$ of the subsystem is related to a mapping state $|m_\lambda\rangle$ of a fictitious harmonic oscillator, which can be described by a coherent state $|z_\lambda\rangle$, with continuous momenta and position variables, $z_\lambda = (q_\lambda + ip_\lambda)/\hbar$. These coherent state variables will be scaled by a factor of $\frac{1}{\sqrt{2}}$ and $\hbar$ will be set equal to 1 for simplicity.

In order for the bath degrees of freedom to be cast into a continuous phase space a partial Wigner transform was employed only over the bath. A definition of the partial Wigner transform with respect to an operator is provided in equation 2.13 and whose presence is now denoted by the subscript, W [40]. By introducing the partial Wigner transform over the bath for a general observable, which introduces

the integral over the bath degrees of freedom, and then taking the trace over the subsystem degrees of freedom culminates in equation 2.14. From this equation it is clear that with appropriate knowledge of the matrix elements of a time-evolved general observable, $B_W^{\lambda\lambda'}(X, t)$, and the partially Wigner transformed density matrix of the system, $\rho_W^{\lambda'\lambda}(X)$, the exciton population can be determined and the excitation energy transfer studied.

$$\hat{B}_W(R, P) = \int dZ e^{iPZ/\hbar} \langle R - \frac{Z}{2}|\hat{B}|R + \frac{Z}{2}\rangle \tag{2.13}$$

$$\langle B(t)\rangle = \mathrm{Tr}_s \int dX \hat{B}_W(X, t)\hat{\rho}_W(X) = \sum_{\lambda\lambda'} \int dX B_W^{\lambda\lambda'}(X, t)\rho_W^{\lambda'\lambda}(X) \tag{2.14}$$

2.2.3   Propagation of the Variables

In order to determine the real-time dynamics, the continuous variables that represent the bath, $X = (R,P)$ and the subsystem degrees of freedom, $(x, x') = (q, p, q', p')$, must be propagated through time. This was achieved using a velocity-Verlet-type integration method [44]. This integration algorithm is outlined in equation 2.15 with attention to the application in the FBTS method. The variable Δt is the time-step used.

$$P_{\mu\kappa}\left(\frac{\Delta t}{2}\right) = P_{\mu\kappa}(0) + \frac{\Delta t}{2}F_{\mu\kappa}(0),$$

$$p_{\mu}\left(\frac{\Delta t}{2}\right) = p_{\mu}(0) - \frac{\Delta t}{2}\sum_{\mu'} h^{\mu\mu'}(R(0))q_{\mu'}(0),$$

$$p'_{\mu}\left(\frac{\Delta t}{2}\right) = p'_{\mu}(0) - \frac{\Delta t}{2}\sum_{\mu'} h^{\mu\mu'}(R(0))q'_{\mu'}(0),$$

$$R_{\mu\kappa}(\Delta t) = R_{\mu\kappa}(0) + \Delta t P_{\mu\kappa}\left(\frac{\Delta t}{2}\right),$$

$$q_{\mu}(\Delta t) = q_{\mu}(0) + \Delta t \sum_{\mu'} h^{\mu\mu'}(R(\Delta t))p_{\mu'}\left(\frac{\Delta t}{2}\right),$$

$$q'_{\mu}(\Delta t) = q'_{\mu}(0) + \Delta t \sum_{\mu'} h^{\mu\mu'}(R(\Delta t))p'_{\mu'}\left(\frac{\Delta t}{2}\right),$$

$$p_{\mu}(\Delta t) = p_{\mu}\left(\frac{\Delta t}{2}\right) - \frac{\Delta t}{2}\sum_{\mu'} h^{\mu\mu'}(R(\Delta t))q_{\mu'}(\Delta t),$$

$$p'_{\mu}(\Delta t) = p'_{\mu}\left(\frac{\Delta t}{2}\right) - \frac{\Delta t}{2}\sum_{\mu'} h^{\mu\mu'}(R(\Delta t))q'_{\mu'}(\Delta t),$$

$$P_{\mu\kappa}(\Delta t) = P_{\mu\kappa}\left(\frac{\Delta t}{2}\right) + \frac{\Delta t}{2}F_{\mu\kappa}(\Delta t),$$

(2.15)

The only quantity yet to be defined is the force, which can be calculated using the following.

$$F_{\mu\kappa} = -\frac{\partial H_e}{\partial R_{\mu\kappa}} = -\omega_{\mu\kappa}^2 R_{\mu\kappa} + \frac{1}{2}c_{\mu\kappa}(q_\mu q_\mu + p_\mu p_\mu + q'_\mu q'_\mu + p'_\mu p'_\mu)$$

(2.16)

2.2.4 Calculation of the Exciton Population

For the calculation of the exciton population observable the partially Wigner transformed density matrix is further simplified by the partition into the subsystem and bath components. Thus, equation 2.17 contains the initial conditions for the subsystem $\hat{\rho}_s$ and the bath $\rho_{b,W}(X)$.

$$\hat{\rho}_W(X) = \hat{\rho}_s \rho_{b,W}(X)$$

(2.17)

The initial conditions of the subsystem must be specified and there are multiple ways in which this can be done. The initial excitation can be on a single pigment in the light harvesting complex or be a particular eigenstate $|E_n\rangle$, such that $\hat{H}|E_n\rangle = e_n|E_n\rangle$

and $|E_n\rangle = \sum_{i=1}^{N} C_{n,i}|i\rangle$. Thus, upon the consideration that site λ'' or eigenstate n, is initially excited this will result in the following expressions for the initial subsystem density in equations 2.18 and 2.19, respectively.

$$\hat{\rho}_s = |\lambda''\rangle\langle\lambda''| \tag{2.18}$$

$$\hat{\rho}_s^{\lambda'\lambda} = C_{n,\lambda'}^* C_{n,\lambda} \tag{2.19}$$

In the case of the initial conditions for the bath, the partial Wigner transformed canonical density matrix of the bath is provided in equation 2.20 [32]. The initial values of the bath degrees of freedom can be sampled from this equation.

$$\rho_{b,W}(X) = \prod_{i,k} \frac{\tanh(\beta\omega_{i,k}/2)}{\pi} exp\Big(- \frac{\tanh(\beta\omega_{i,k}/2)}{\omega_{i,k}} \Big(P_{i,k}^2 + \omega_{i,k}^2 R_{i,k}^2 \Big) \Big), \tag{2.20}$$

where $\beta = (k_B T)^{-1}$ and k_B is the boltzmann constant.

The calculation of the matrix elements of a time-dependent observable can be completed using the FBTS method with equation 2.21 [30, 31]. For each trajectory the initial values of the two sets of coherent state variables and the bath variables must be sampled. The coherent state variables are sampled from the nomalized Gaussian functions $\phi(x)$ and $\phi(x')$, defined as $\phi(x) = \hbar^{-N} e^{-\sum(q_v^2 + p_v^2/\hbar)}$. In this equation there is a contribution from the initial $((q_\lambda + ip_\lambda)(q'_{\lambda'} - ip'_{\lambda'}))$ and time-dependent coherent state variables $((q_\mu(t) - ip_\mu(t))(q'_{\mu'}(t) + ip'_{\mu'}(t)))$ that will be propagated through time.

$$B_W^{\lambda\lambda'}(X,t) = \sum_{\mu\mu'} \int dx dx' \phi(x)\phi(x')(q_\lambda + ip_\lambda)(q'_{\lambda'} - ip'_{\lambda'})B_W^{\mu\mu'}(X_t)$$

$$\times (q_\mu(t) - ip_\mu(t))(q'_{\mu'}(t) + ip'_{\mu'}(t)) \tag{2.21}$$

In this research we go beyond the calculation of a general observable and are interested in the determination of the population of the exciton (denoted now as $U(t)$). By specifying that the initial condition of the excitation energy is on a single site, this will result in equation 2.22 for the expectation value of the population.

Alternatively, when the initial condition is a particular eigenstate n, this will result in equation 2.23. The integral over the many-dimensional bath and the subsystem degrees of freedom was calculated by evolving Monte Carlo trajectories.

$$\langle U(t)\rangle = \sum_{\mu\mu'} \int dXdxdx'\phi(x)\phi(x')(q_{\lambda''}+ip_{\lambda''})(q'_{\lambda''}-ip'_{\lambda''})U_W^{\mu\mu'}(X_t)$$
$$\times (q_\mu(t)-ip_\mu(t))(q'_{\mu'}(t)+ip'_{\mu'}(t))\rho_{b,W}(X) \quad (2.22)$$

$$\langle U(t)\rangle = \sum_{\lambda\lambda'}\sum_{\mu\mu'} \int dXdxdx'\phi(x)\phi(x')(q_\lambda+ip_\lambda)(q'_{\lambda'}-ip'_{\lambda'})U_W^{\mu\mu'}(X_t)$$
$$\times (q_\mu(t)-ip_\mu(t))(q'_{\mu'}(t)+ip'_{\mu'}(t))\rho_{b,W}(X)C^*_{n,\lambda'}C_{n,\lambda} \quad (2.23)$$

Through either equations 2.22 or 2.23 the elements of the system density matrix, ρ, describing the exciton can be determined. The population of the exciton on a particular site is contained in the diagonal elements of this matrix and will sum to 1, while the off-diagonal elements correspond the coherences. A measure of the delocalization of the exciton can be completed through a consideration of the inverse participation ratio, that describes only the delocalization over each of the sites in the light harvesting complex, or the coherence length, that takes in account these off-diagonal elements, calculated using equations 2.25 and 2.24 respectively [45, 46]

$$L_p = \frac{1}{N}\frac{(\sum_{ij}|\rho_{ij}|)^2}{\sum_{ij}|\rho_{ij}|^2} \quad (2.24)$$

$$\text{IPR}(t) = \frac{1}{\sum_i \rho_{ii}(t)^2} \quad (2.25)$$

The calculation of the weak coupling limit or Boltzmann steady state populations for each site is useful to compare to the long-term steady states reached by the FBTS method. This boltzmann population U is calculated using equation 2.26.

$$U_{\text{stationary}}^k = \frac{e^{-(E_k-E_{gs})/k_BT}}{Z} \quad (2.26)$$

where,

$$Z = \sum_k e^{-(E_k-E_{gs})/k_BT}. \quad (2.27)$$

The Frenkel exciton model captures the important details for excitation energy transfer of the natural light harvesting systems. The FBTS method can be used to calculate the population of the exciton on a particular pigment within this model. Through the propagation of the continuous variables through time can the real-time dynamics of the exciton be observed. Thus, this provides an effective way analyze the excitation energy transfer in light harvesting complexes. A version of the FBTS code can be found with Appendix A.

Chapter 3

The Exciton Dimer Model

The exciton dimer model represents a simple pedagogical example in which theoretical methods can be applied to examine the real-time dynamics of the excitation energy transfer [25, 39, 47–49]. A pictorial representation is provided in Figure 3.1. In this chapter the FBTS method is applied to the exciton dimer model and the influence of the system parameters on the excitation energy transfer is investigated.
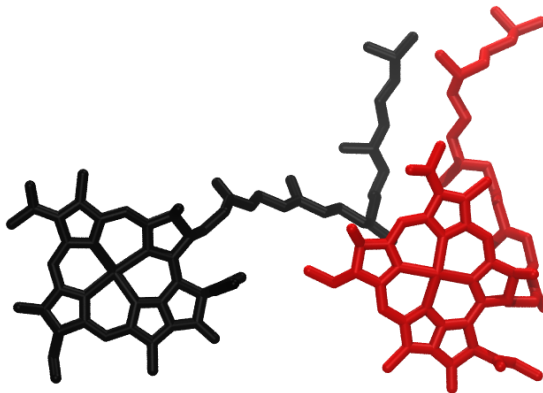
Figure 3.1: Representation of the simple exciton dimer model. The pigment in black represents site 1 and red represents site 2. Choice of relative orientation, distance and pigment type between sites is arbitrary.

The low number of electronic states and simplicity of this model provides an opportunity to delve into how the subsystem and subsystem-bath Hamiltonian are composed for this system. This will assist in providing a foundation into these components as found in the larger light harvesting complexes studied in this thesis. Equation 3.1 contains the subsystem Hamiltonian; wherein ϵ_1 and ϵ_2 corresponds to the site energy for pigments 1 and 2, respectively, and J_{21} is the coupling between the pigments. Since the coupling between site 1 and site 2 is equivalent to the coupling between site 2 and site 1, the subsystem Hamiltonian is symmetric such that $J_{ij} = J_{ji}$. The subsystem Hamiltonian used in the study of the exciton dimer model is from Ref. [25] and was chosen for the opportunity to benchmark the FBTS method to the results

within (more detail is given later in the chapter). Therefore, the difference in the site energies are set too $\epsilon_1 - \epsilon_2 = 100cm^{-1}$ and the coupling strength between the sites will be, $J_{12} = 100cm^{-1}$.

$$H_s = \begin{bmatrix} \epsilon_1 & J_{12} \\ J_{12} & \epsilon_2 \end{bmatrix} = \begin{bmatrix} 100 & 100 \\ 100 & 0 \end{bmatrix} \quad (3.1)$$

The surrounding environment is simplified as a collection of K harmonic oscillators described by a particular coupling constant, c_κ, and position, R_κ. The influence of the bath enters the exciton dimer model through the subsystem-bath Hamiltonian, provided in equation 3.2. Specifically, this means that each site will receive an independent but equivalent bath; thus the coupling strength and bath coordinates variables lose the site basis subscript. The bath is described using three parameters, the reorganisation energy, λ, the characteristic bath frequency, ω_c, (through the approximate Debye spectral density) and finally the temperature, T.

$$H_{sb} = \begin{bmatrix} -\sum_\kappa^K c_\kappa R_\kappa & 0 \\ 0 & -\sum_\kappa^K c_\kappa R_\kappa \end{bmatrix} \quad (3.2)$$

The small and artificial nature of this model allows for parameters that effect the excitation energy transfer to be easily studied; specifically for this work, the temperature, characteristic bath frequency, reorganization energy, and the intersite couplings between the pigments were examined. Each simulation in the exciton dimer model has resulted from an initial condition where site 1 was excited; then the subsystem and bath degrees of freedom were propagated through time in order to calculate the population of the exciton on each of these two sites.

3.1 Influence of the Environment on the Population Dynamics

In order to clearly and concisely communicate the impact of the bath on the excitation energy transfer through this simple exciton dimer model and other natural light harvesting complexes, Figure 3.2 is provided. This figure represents the first results from the FBTS method, the basic characteristics of this figure is highlighted since similar graphs will reoccur throughout this thesis. Each curve corresponds to

the population of the exciton on a particular site. Since time is on the x-axis, by following the magnitude of the curves from left to right the excitation energy transfer can be observed. In Figure 3.2 there are two sets of dynamics, the solid curves correspond to the case where there is no bath effecting the system and the dashed curves correspond where there is the presence of the bath.
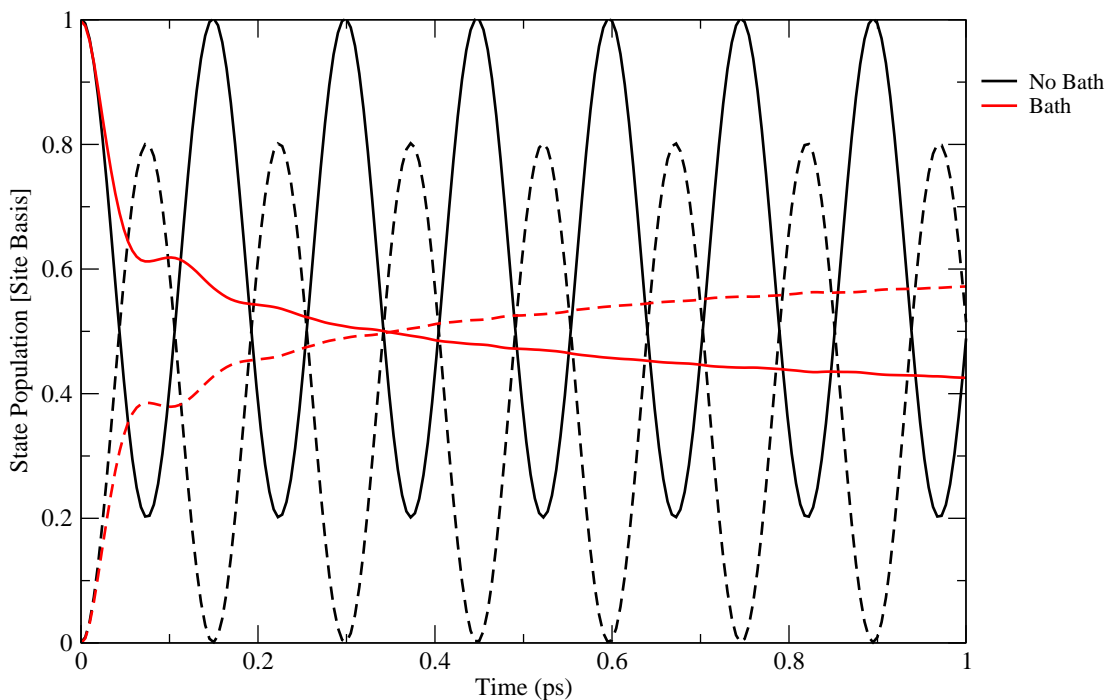
Figure 3.2: Exemplification of the dissipative effects from the environment on the excitation energy transfer dynamics in the exciton dimer model. The black line corresponds to the dynamics without the bath and the red line is the dynamics with the bath. The population on site 1 and 2 corresponds to the solid and dashed line, respectively.

In the case where the dynamics of the subsystem do not experience the effects of the bath the population repetitively oscillates between the two sites. With the addition of the bath the site populations experience a dampening effect and will eventually reach a steady state value as the energy is dissipated [18]. A steady state value is recognised when the site population does not change in time. In terms of

a real light harvesting complex the exciton possesses a purposeful direction to the transport of energy, the reaction centre [3]. In these simulations there is no trap so the population dynamics arrive at a steady state value.

These population graphs determined through the FBTS method can allow for details about the transfer to be extracted. Specifics regarding the population of the exciton, such as the steady state values for each site and the identification of the sites that receive a significant portion of the exciton. Along with the particulars about the time frame, such as the time to reach this steady state value and the time it takes for the system to lose coherence (the oscillatory motion of the population). Additionally, details on the time for the exciton to considerably populate a particular site can be determined (a more important aspect for larger systems).

3.1.1   Effect of the Reorganization energy, λ

The reorganization energy characterizes the strength of the coupling of the bath to the system and due to the dissipative effect of the bath, this parameter is highly important for the dynamics of the system. The other coupling in the system is between each pigment and there is an interplay between the magnitude of these two couplings (that of the system-bath, λ, and pigment-pigment, J_{ij}). There are three regimes upon comparing the magnitude of these couplings; in the case that $\lambda < J_{ij}$ this is the weak coupling regime, when λ and J_{ij} are close in value, the intermediate regime, and finally when $\lambda > J_{ij}$ this is the strong coupling regime [24]. Absorption and fluorescence spectra can reveal the Stokes shift which is directly related to the reorganization energy [7]. In Figure 3.3 the effect of the reorganization energy in these coupling regimes in the exciton dimer model is investigated.

From the top panel of Figure 3.3 it is observed that with an increase in the reorganization energy there is a large suppression in the oscillatory nature of the dynamics between sites 1 and 2 (distinguished by a solid and dashed line). This is realized for all four of the reorganization energies represented here, from the weak regime to the strong. Through a comparison of the dynamics when $\lambda = 2\ cm^{-1}$ and $\lambda = 100\ cm^{-1}$, the time it takes to reach a steady state population is faster for a larger reorganization energy. From the bottom panel the three smallest reorganization energies, $\lambda = 2$, 20 and $100cm^{-1}$, illustrate a relationship between the reorganization energy and the
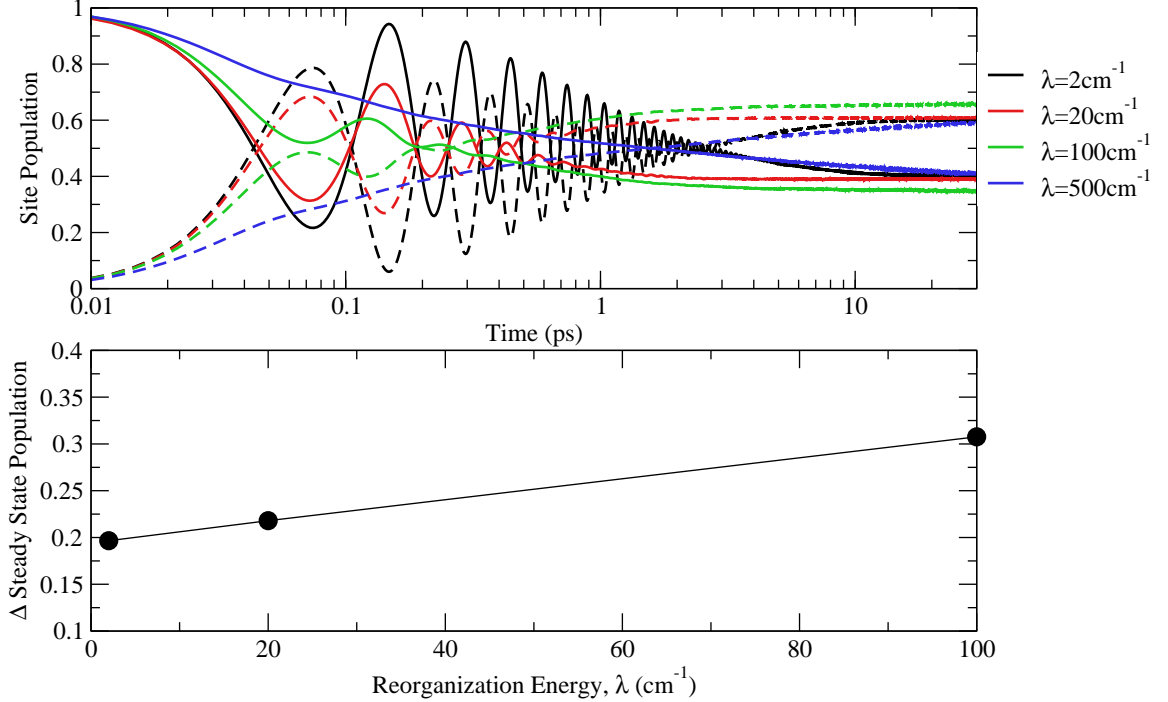
Figure 3.3: Depiction of the effect of different reorganization energies (λ) on the population dynamics in the exciton dimer model. The temperature (T) is $300K$ and the characteristic bath frequency (ω_c) is $50cm^{-1}$. The top panel contains the excitation energy transfer, wherein the population on site 1 and 2 corresponds to the solid and dashed line, respectively. The bottom panel is the difference in the steady state population between the sites. Under the timescale simulated a value for a reorganization energy of $500cm^{-1}$ was unable to be extracted.

difference in the steady state population. Specifically, as the coupling strength to the bath increased the population of the exciton is more unevenly distributed between the two sites of the system, with site 2 (the site with the lowest site energy) consistently receiving the greater portion of the exciton. However, the largest reorganization energy, $\lambda = 500cm^{-1}$, does not follow the two previous trends; the dynamics took the longest to reach a steady state and thus is not included in the bottom panel of Figure 3.3, since it did not reach the steady state population. Therefore, it is clear that the reorganization energy has an effect on the dynamics of the system, increasing the speed to which the steady state is reached and the distribution between the two sites.

However, the dynamics when, $\lambda = 500cm^{-1}$, reveal that these trends are not general over the full range or reorganization energies.

3.1.2 Effect of the Characteristic Frequency, ω_c

The approximate Debye spectral density is also parameterized by the characteristic bath frequency, ω_c, and the effect on the exciton dimer model is provided in Figure 3.4. From the top panel, the excitation energy transfer at a short time scale showed that the dynamics for the four characteristic bath frequencies analyzed are similar. Again, the population of the exciton will oscillate between the two sites before reaching a steady state value. The dynamics at $\omega_c = 10cm^{-1}$, the smallest value, show the presence of larger and more numerous oscillations. From the bottom panel, that contains the difference in the steady state population between the two sites, only this characteristic bath frequency depicts a significantly different and smaller gap. From $\omega_c = 50cm^{-1}$ and above, for the parameter values studied, approximately the same steady state population difference is reached; wherein, $\omega_c = 100$ and $200cm^{-1}$ reached this steady state value in a similar timeframe but $\omega_c = 50cm^{-1}$ took a longer time. Changing the characteristic bath frequency also has an affect on the excitation energy transfer dynamics in the exciton dimer model.
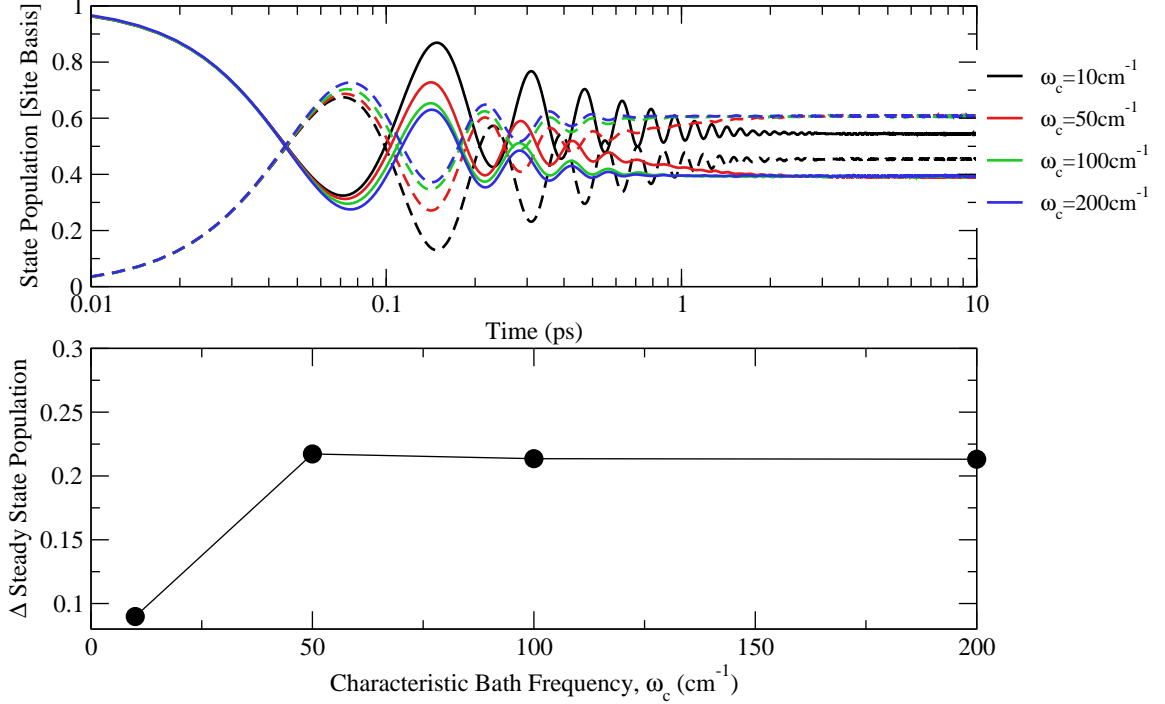
Figure 3.4: Depiction of the effect of different characteristic bath frequencies (ω_C) on the population dynamics in the exciton dimer model. The temperature (T) is $300K$ and the reorganization energy (λ) is $20cm^{-1}$. The top panel contains the excitation energy transfer, wherein the population on site 1 and 2 corresponds to the solid and dashed line, respectively. The bottom panel is the difference in the steady state population between the sites.

3.1.3 Effect of the Temperature, *T*

Another influence on the dynamics of the excitation energy transfer is the temperature, the effect of which enters the simulation through the sampling of the initial momenta and positions of the bath. The influence of the temperature on the dynamics can be seen depicted in Figure 3.5. The temperature range between $T = 10K$ to $T = 300K$ was simulated in order capture the dynamics at room temperature and contrast with the dynamics at colder temperatures.

From the top panel, the change in the temperature has little effect on the very short term exciton population on the two sites. Additionally, the time in which the sites
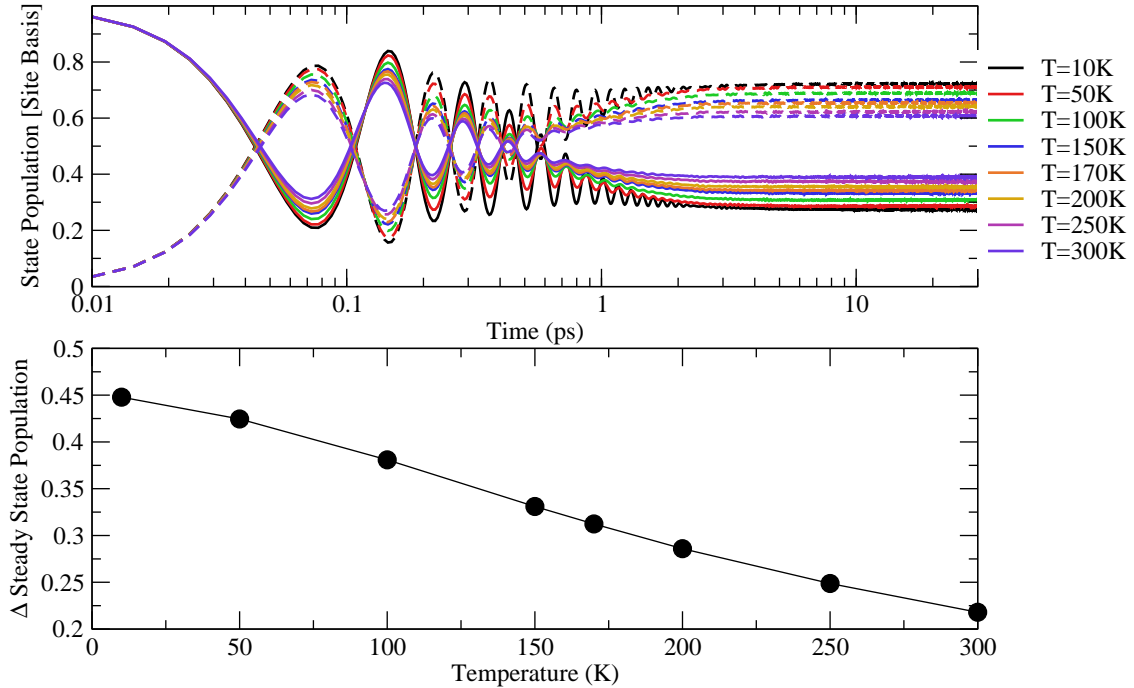
Figure 3.5: Depiction of the effect of different temperatures (T) on the population dynamics in the exciton dimer model. The characteristic bath frequency (ω_c) is $50cm^{-1}$ and the reorganization energy (λ) is $20cm^{-1}$. The top panel contains the excitation energy transfer, wherein the population on site 1 and 2 corresponds to the solid and dashed line, respectively. The bottom panel is the difference in the steady state population between the sites.

reach a steady-state population is similar for all choices of the temperature. However, the amplitudes of the population oscillations between the sites are diminished as the temperature increased. At high temperatures the site population fluctuates for less time, the bath dampens the dynamics more. From the bottom panel, it is observed that at high temperatures the steady state population of the exciton is spread more evenly between the two sites, and as the temperature decreases, this gap increases.

3.2 Effect of the Difference in Site Energy, $\Delta\epsilon$

The above sections are dedicated to the analysis of the consequence of the bath on the system, this section will see the effect of an increase or decrease in the site energy gap between the two pigments. Figure 3.6 depicts the the result of changing the the site energy gap of the pigments between a range of $\epsilon_1 - \epsilon_2 = 0$ to $200cm^{-1}$.
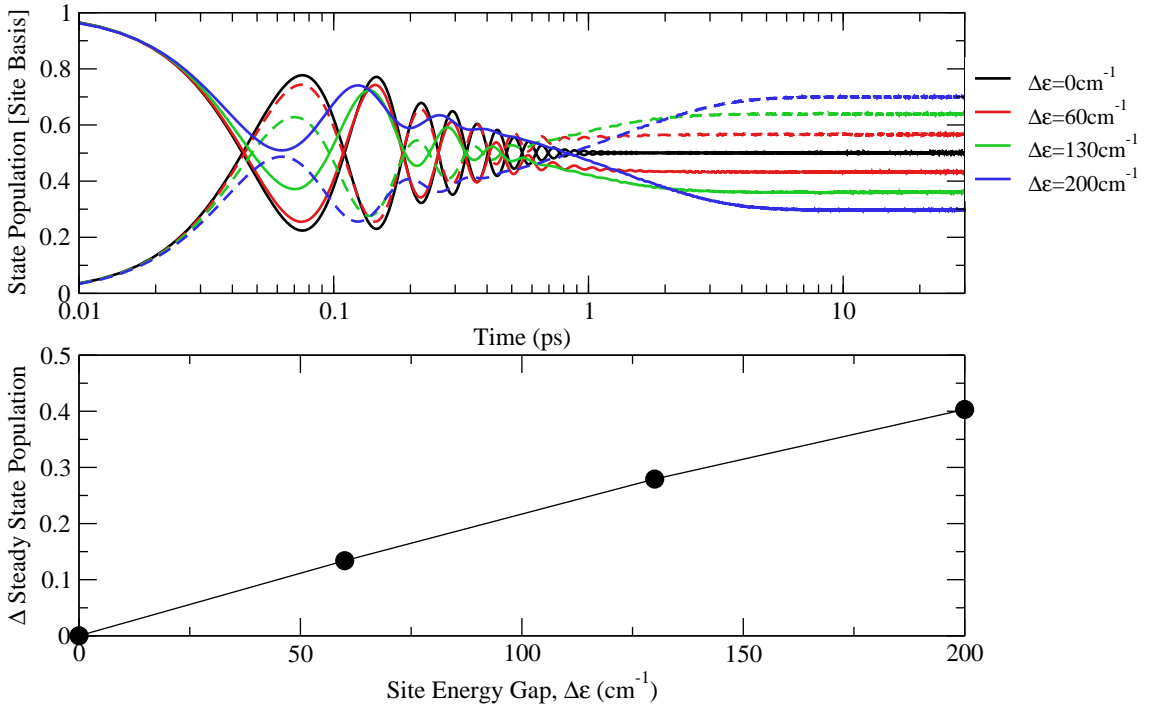
Figure 3.6: Depiction of the effect of different site energy gaps ($\Delta\epsilon$) on the population dynamics in the exciton dimer model. The temperature (T) is $300K$, the characteristic bath frequency (ω_c) is $50cm^{-1}$ and the reorganization energy (λ) is $20cm^{-1}$. The top panel contains the excitation energy transfer, wherein the population on site 1 and 2 corresponds to the solid and dashed line, respectively. The bottom panel is the difference in the steady state population between the sites.

The population is less evenly distributed between the two sites as the site energy gap is increased. This means that the exciton is more localized on a single site. When there is no difference in the site energy gap the population is equally shared between the two sites at long times.

3.3 Evaluation of the Accuracy of the FBTS method

As this is an approximate method, it is of particular importance to provide some insight into the level of accuracy and validity of this method. This is most easily obtained through a comparison to numerically exact results. The Hierarchical Equations of Motion (HEOM) method is one such numerically accurate and in principle exact method with the model under study. The FBTS method was compared against results from Ishizaki and Fleming [25] using this exciton dimer model. A further comparison is made with another approximate theory, Redfield, that calculates the matrix elements of the reduced density matrix in the eigenstate basis. Through a basis conversion the exciton population on a site can be determined. The approximations made in the Redfield equation, taking the system-bath coupling as a perturbation and the Markov approximation, performs best in regimes of small reorganization energies and with a high characteristic bath frequency [24, 25, 48]. Figure 3.7 and 3.8 contain this comparison.

A multitude of reorganization energies were examined, from a range of weak to strong coupling with the bath. Both the FBTS and Redfield theory are in good agreement with the exact results, from the HEOM method, at a small reorganization energy of $\lambda = 2cm^{-1}$. Upon an increase in strength it is observed that the Redfield theory is no longer in good agreement with the HEOM results, while the FBTS method has some slight deviations.

Additionally, another comparison was made to the exact results using the same model but with another choice of the characteristic bath frequency, in this case $\omega_c = 10.61cm^{-1}$. Again the FBTS method is able to sufficiently reproduce the exact results even under higher reorganization energies where the Redfield theory results in more deviation. In comparison to the previous system, the FBTS method is worst in the regime with the lower characteristic bath frequency. It should be noted that the comparison graphs only encapsulate the very beginning of the excitation energy transfer dynamics since the temporal aspect ends after 1 picosecond, this leaves in question whether or not the FBTS method captures the long-term steady state limits. However, this comparison does serve to inform that the FBTS method can capture the excitation energy dynamics best with a higher characteristic frequency and smaller reorganization energies.
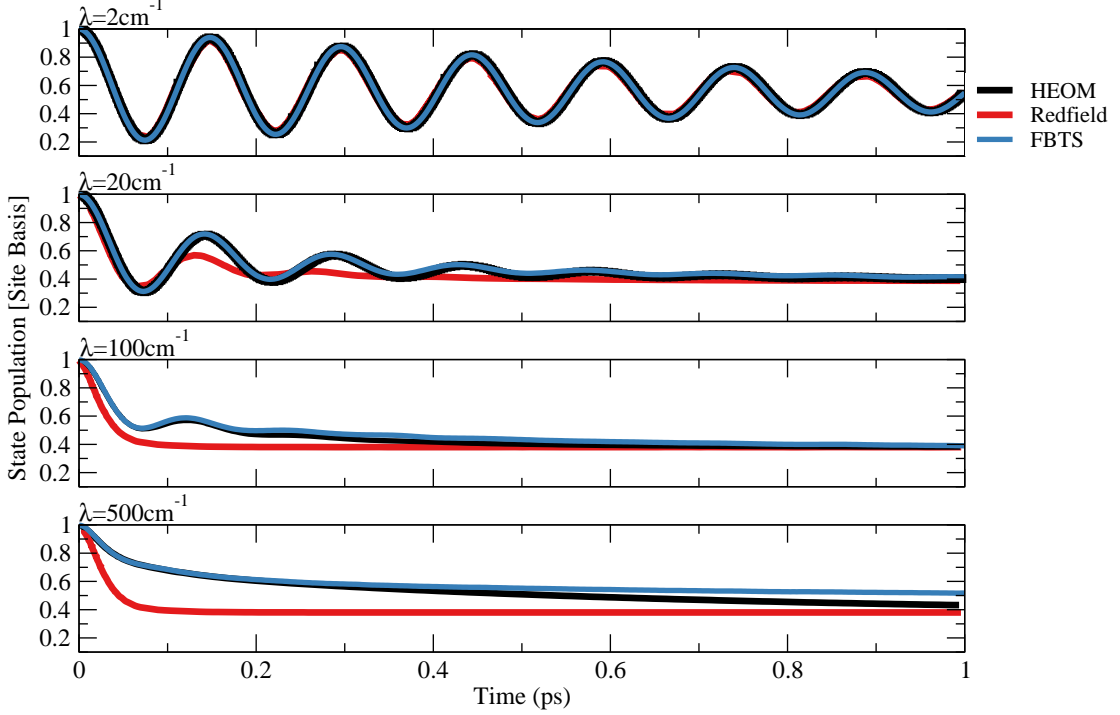
Figure 3.7: Comparison of the excitation energy transfer in the exciton dimer model with the HEOM and Redfield Theory methods from Ref. [25] with FBTS. The initial excitation is on site 1 and only the population of this site is shown. Each panel depicts the dynamics under a different reorganization energy from a range of $\lambda = 2\text{-}500cm^{-1}$. The temperature ($T$) is $300K$ and the characteristic bath frequency (ω_c) is $53.08cm^{-1}$.

A more through investigation into the accuracy of the FBTS method with the exciton dimer model was completed in the literature; [48] from this study it is clear that the parameters that characterize the bath, the reorganization energy, the characteristic bath frequency and the temperature, along with the site energies and couplings between pigments, all have an effect on the accuracy of this approximate method. Again this evaluation of accuracy was achieved with a comparison to the HEOM method; as FBTS is used to investigate larger systems beyond what can be reasonably examined by the HEOM method, it will be important to gauge the accuracy of this method against the observables that can be obtained through experiments
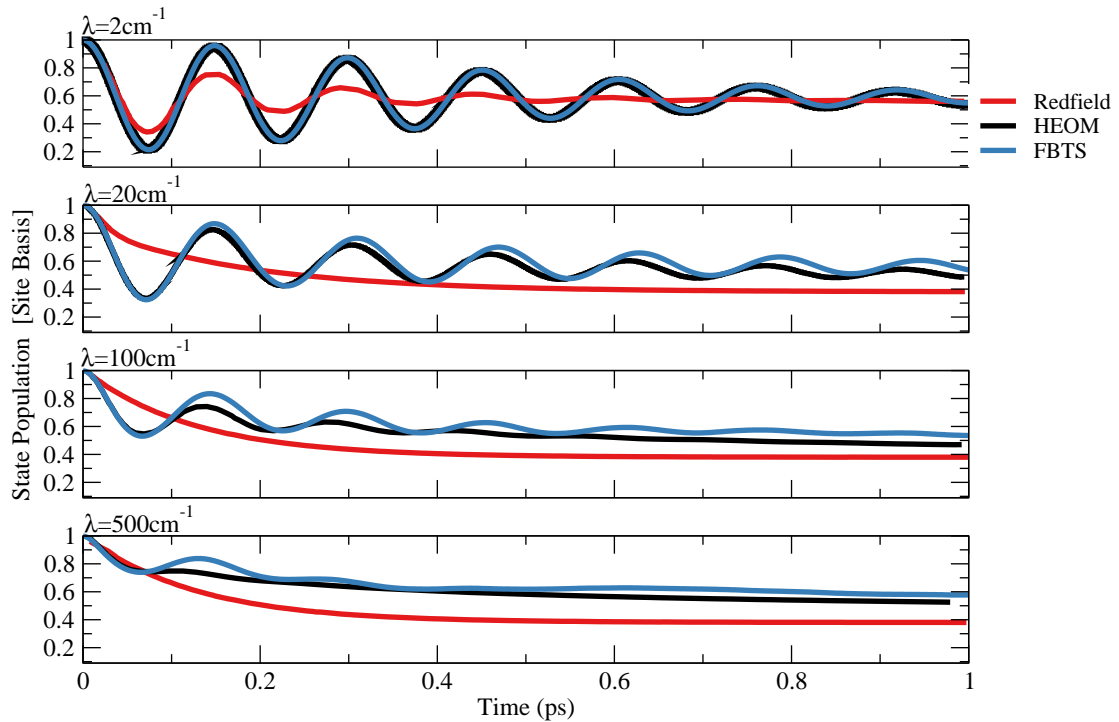
Figure 3.8: Comparison of the excitation energy transfer in the exciton dimer model with the HEOM and Redfield Theory methods from Ref. [25] with FBTS. The initial excitation is on site 1 and only the population of this site is shown. Each panel depicts the dynamics under a different reorganization energy from a range of $\lambda = 2\text{-}500 cm^{-1}$. The temperature ($T$) is $300K$ and the characteristic bath frequency (ω_c) is $10.61 cm^{-1}$.

on these real systems, such as the comparison to absorption, fluorescence and linear dichroism spectra. More specific information about the excitation energy transfer can be determined using experiments such as two-dimensional (2D) electronic spectroscopy [50].

Chapter 4

Plant Light Harvesting Complexes

The light harvesting complexes in higher plants are components of a larger apparatus composed of photosystem I (PSI) and photosystem II (PSII), both contain a reaction centre [12]. Surrounding the reaction centre in PSII is a multitude of light harvesting complexes, including the major complex, LHCII, which has been previously studied both experimentally and theoretically [23, 27, 50–55]. Conversely, CP26 a minor light harvesitng complex is PSII, represents a fairly new avenue for study due to the fact that the definite structure was not determined until recently [12].

In this thesis, this is the first exploration of the dynamics of a natural light harvesting complex. This chapter investigates the excitation energy transfer in LHCII and CP26 separately, as opposed to taking a view of the flow of the exciton through PSII [56]. Each section begins with a summary of the structure, both spatial and energetic, to provide context for the excitation energy transfer function, that is presented in the next section. The exciton transport mechanisms for two different site locations for the initial excitation and at two different temperatures are presented.

4.1 LHCII

4.1.1 Description of the Structure

The structure of the LHCII light harvesting complex is known with atomistic detail due to the information provided by crystallography studies [12]. This allows for the spatial organization of the structure to be shown; Figure 4.1 depicts one monomer, since LHCII is a trimer. Since the primary focus of this thesis is the excitation energy transfer, only the main pigments involved will be shown in this figure and all subsequent figures that contain structures of natural light harvesting complexes. Thus, only the 14 chlorophyll pigments in the LHCII monomer are labelled in Figure 4.1 and not any other pigments present (such as caroteniods). Each pigment is identified

by a number from 1 to 14, with pigments 1, 5, 6, 7, 8 and 9 being chlorophyll B and pigments 2, 3, 4, 10, 11, 12, 13, and 14 being chlorophyll A. The relationship between the notation used in this thesis and the literature is provided in Appendix B in Table B.1. The surrounding light grey structure is the protein scaffold.
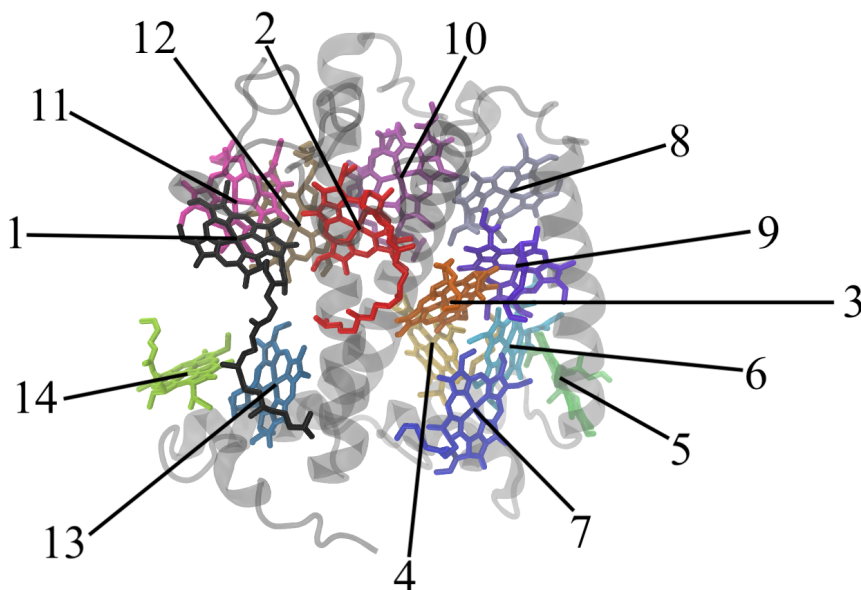
Figure 4.1: Depiction of the LHCII monomer from spinach; wherein the coloured molecules are the pigments and the grey structure is the protein. There are 14 chlorophyll pigments in the LHCII monomer labelled succinctly from 1 to 14 in this thesis. Sites 1, 5, 6, 7, 8, and 9 are chlorophyll B and sites 2, 3, 4, 10, 11, 12, 13, and 14 are chlorophyll A. The intersection between the chosen labelling convention and the alternate one found in the literature is provided in Table B.1 of Appendix B. This structure was adapted from RCSB PDB (rcsb.org) of PDB ID: 3jcu [12] using VMD [57].

The subsystem Hamiltonian for the LHCII monomer was taken from references [52, 58], where the numerical values are supplied in Appendix C in Table C.1. A pictorial summary of this information is provided in Figure 4.2, and allows for the energetic landscape of the LHCII monomer to be displayed. The relative site energies are included on the left of Figure 4.2, revealing that the sites with the highest energies are all chlorophyll B. The two sites with the highest relative site energies are 1 and 6, whereas 2, 10, 11, and 12 have the lowest energy. The intersite couplings between each site in the LHCII monomer is depicted on the right of Figure 4.2, (wherein the
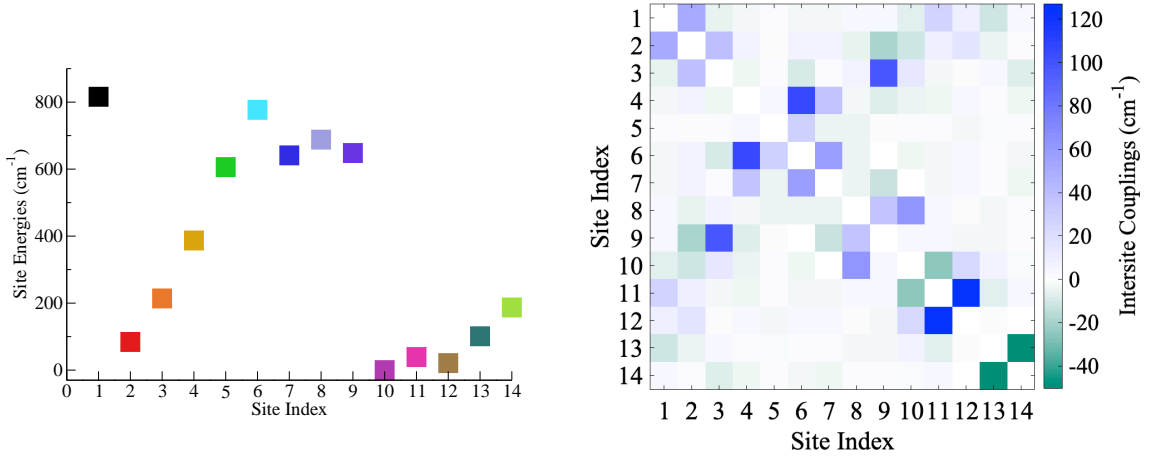
Figure 4.2: Energetic landscape of the LHCII monomer with the site energies on the left and the intersite couplings on the right for each of the 14 pigments given in units of cm^{-1} [52]. These are the relative site energies with respect to the lowest lying pigment, in this instance site 10. The magnitude of the intersite coupling between each pigment is represented by a colour tone between green and blue, with the more vivid the colours corresponding to larger negative or positive number, respectively. For LHCII the sites 1, 5, 6, 7, 8, and 9 are chlorophyll B and the sites 2, 3, 4, 10, 11, 12, 13, and 14 are chlorophyll A. The exact subsystem Hamiltonian is provided in Table C.1 from Appendix C.

vivid tone of the colour corresponds to a stronger coupling) revealing a few groups of sites that are strongly coupled, such as sites 10, 11 and 12.

In this thesis the excitation energy transfer through one monomer of LHCII and through the full light harvesting complex was studied with the FBTS method. For the monomer the subsystem Hamiltonian used is the one outlined above but for the full LHCII complex, composed of three of the monomers depicted in Figure 4.1, required a larger subsystem Hamiltonian, that was supplied from Ref. [52]. Now, for each of the 42 pigments in the trimer there must be a particular coupling between a pigment from one monomer to the next. The form of this trimeric Hamiltonian is provided in equation 4.1 [47]. Wherein, the notation H_{mono} is the site energies and couplings for one monomer and H_{inter} is the intersite couplings between each monomer. The numerical values of these components can be found in Appendix C in Tables C.2 and C.3.

$$H_{trimer} = \begin{bmatrix} H_{mono} & H_{inter} & H_{inter}^{\dagger} \\ H_{inter}^{\dagger} & H_{mono} & H_{inter} \\ H_{inter} & H_{inter}^{\dagger} & H_{mono} \end{bmatrix} \qquad (4.1)$$

The approximate Debye spectral density is used for the study of the excitation energy transfer through the LHCII monomer and trimer in this chapter. The parameters that will characterize the bath were taken from Ref. [51], these values are $100cm^{-1}$ for the characteristic bath frequency and $85cm^{-1}$ for the reorganization energy. Other approximate forms of the spectral density have been used to study the transfer in the LHCII light harvesting complex as explored by Aspuru-Guzik et. al. [58]. These approximate forms are more complex and serve to try and capture the characteristics of the real spectral density for LHCII, an obvious point of improvement.

4.1.2   Excitation Energy Transfer Mechanisms

In natural light harvesting complexes there is a rise in complexity due to the increase in sites and the particular energetic landscape. In the case of the LHCII monomer there are 14 possible sites to receive the initial excitation and to observe the mechanism of transport through the complex. Two choices for the initial excitation were analyzed in this chapter; the two sites with the highest relative site energy were selected to order to examine how the energy will flow to lower energy sites. These sites are 1 and 6 (both are chlorophyll B). The affect of the temperature was also inspected through the simulation of the dynamics at room temperature: $T = 300K$ and cryogenic temperature: $T = 77K$.

Figure 4.3 depicts the excitation energy transfer in the LHCII monomer with an initial excitation on site 1. The dynamics that have resulted are not too intricate with only a few sites receiving a significant portion of the exciton. At a temperature of $T = 300K$ (in the top panel), site 1 maintains the highest population until approximately 7 picoseconds. Site 2 will receive a significant amount of the population then decrease over time. The sites that receive the majority of exciton population at the end of the simulation are 10, 11, and 12. For the other sites not previously mentioned, 3 and 13 maintain a population below 0.07 for the duration of the simulation, sites 4 and 14 stay below 0.04 and sites 5, 6, 7, 8, and 9 stay below 0.015. Thus, even though there

are 14 sites in this system, the mechanism of transfer for the exciton only involves a select number of pigments.

Similar dynamics are observed at cryogenic temperature ($T =$ is $77K$), provided in the bottom panel of Figure 4.3, with some deviations. Site 1 maintained the highest exciton population until a later time of approximately 16 picoseconds. Site 2 reached a smaller maximum population but again the sites with the majority of the exciton at the end of the simulation were sites 10, 11 and 12; with a difference in the orientation of the ending populations. The sites that end with the majority of the exciton are all chlorophyll A and represent the sites with the lowest energy, independent of temperature. The remaining sites received even less of the exciton population, sites 4 and 13 stay below 0.055, sites 3 and 5 stay below 0.027, site 7 stays below 0.018, and sites 6, 8, 9 and 14 stay below 0.013. The cryogenic temperature resulted in a lower contribution from the sites that are not the initial or ending sites.

Figure 4.3: The real-time dynamics in the LHCII monomer with an initial excitation on site 1. The parameters describing the Debye spectral density are, for the characteristic bath frequency (ω_c), $100cm^{-1}$ and, for the reorganization energy (λ), $85cm^{-1}$. The top panel corresponds to the dynamics at room ($T = 300K$) temperature and the bottom panel is at cryogenic ($T = 77K$) temperature.

From the simulations of excitation energy transfer, the general behaviour of the population dynamics on each site can be divided into three basic regimes. The first regime describes the site that has been initially excited. This site will start with a population of 1 and experience a decrease over time. The second regime describes the behaviour of transient sites for the exciton. These sites are characterized by reaching a maximum population and afterwards experiencing a decrease as a portion of the population is transferred to other sites. Lastly, the third regime contains the sites that receive the majority of the exciton at the end of the simulation and only experience an increase in the population.

Figure 4.4 is a summarization of the mechanistic transport of the exciton through

the LHCII monomer as shown in Figure 4.3; similar figures will be presented in subsequent chapters and the pertinent details are expanded on here. This figure is arranged by relative site energy versus site index and only includes the sites that contribute significantly to the transfer, the general threshold is if a particular site's population goes above 0.10. This serves to highlight and emphasize the sites that contribute to the transport mechanism. Additional information on the general regimes of transfer for each site is communicated through the presentation of the x-axis. The initially excited site occupies the left-most position on the figure, the transient sites are organized by increasing site index in the middle and the right-most position contains the ending sites, further designated by an ellipse. In order to provide more concrete information concerning the time scale of the excitation energy transfer and assist in quantifying the speed of transfer on and off a site, where appropriate, text is provided to demarcate certain moments, such as when a site reached a 0.50 or 0.10 population threshold, or a transition site reached a maximum population. The exciton population of the ending sites at the conclusion of the simulation are also provided.
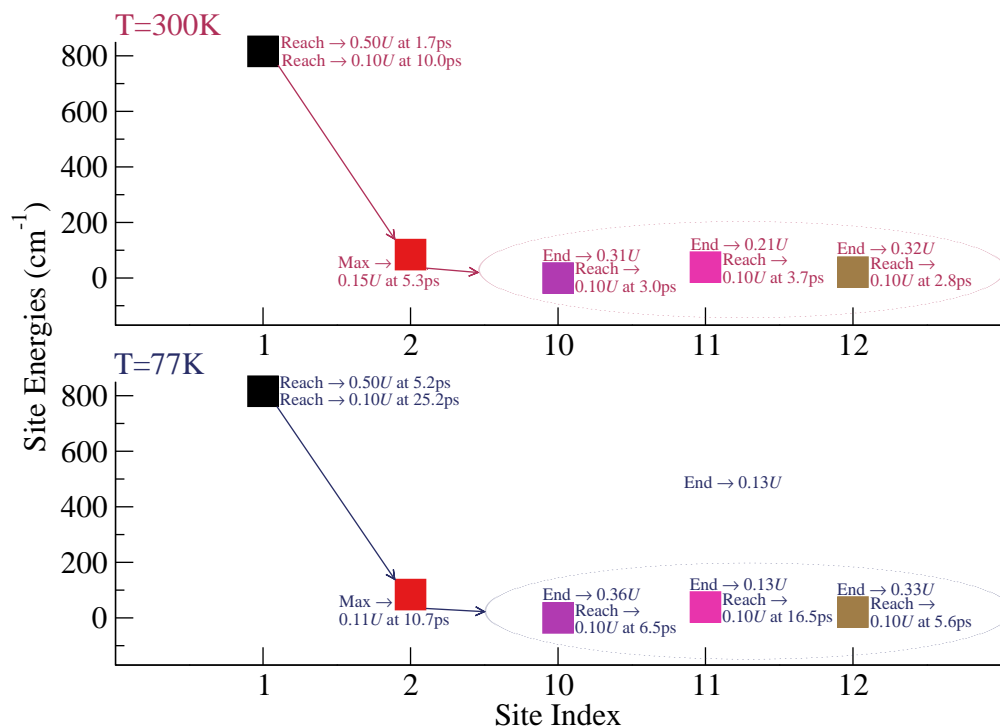
Figure 4.4: Mechanistic summary of the excitation energy transfer in the LHCII monomer with an initial excitation on site 1. The top and bottom panel correspond to the dynamics at room and cryogenic temperature, respectively. The panels are arranged such that the initially excited state is on the left, the transiently populated sites occupy the middle and the ending sites are encased in an ellipse and are found to the right. The text inserts are a selection of extracted population (U) and time (t) data.

Figure 4.4 captures the mechanistic transport of the exciton through the LHCII monomer with the sites that play the most substantial role. The main pigments involved in the transfer of energy are sites 1 and site 2 with the exciton ending on sites 10, 11, and 12. An examination of the structure of the LHCII monomer in Figure 4.1 reveals that the sites involved in this transfer are spatially close to each other. At room temperature, the initially excited site 1 hits a population of 0.10 at 10.0 picoseconds and at a cryogenic temperature this time was much later at 25.2 picoseconds. The next site to receive a significant portion of the exciton population is site 2 and will reach a maximum population of 0.15 for $T = 300K$ and 0.11 for T

$= 77K$ at a time of 5.2 and 10.7 picoseconds, respectively. Finally, the population will grow and a majority of the exciton population will end up on sites 10, 11, and 12. At the lower temperature the real-time dynamics are slower with a larger spread in the population of the sites that receive the majority of the population at the end of the simulation.

Upon changing the location of the initial excitation to the site with the next highest site energy, site 6, an alternative route for the excitation energy transfer is observed. Figure 4.5 contains the real-time dynamics at room and cryogenic temperature for this new initial excited state. The timescale for this figure was changed to begin at 0.01 picoseconds in order to capture the notable dynamics that occur within a short time.
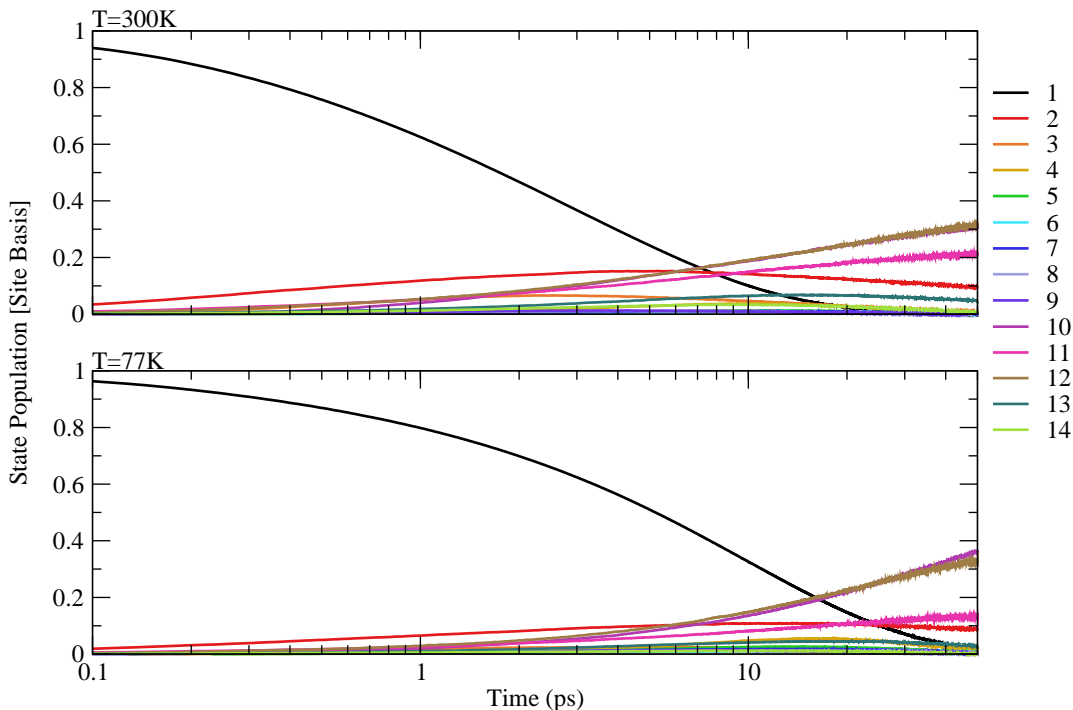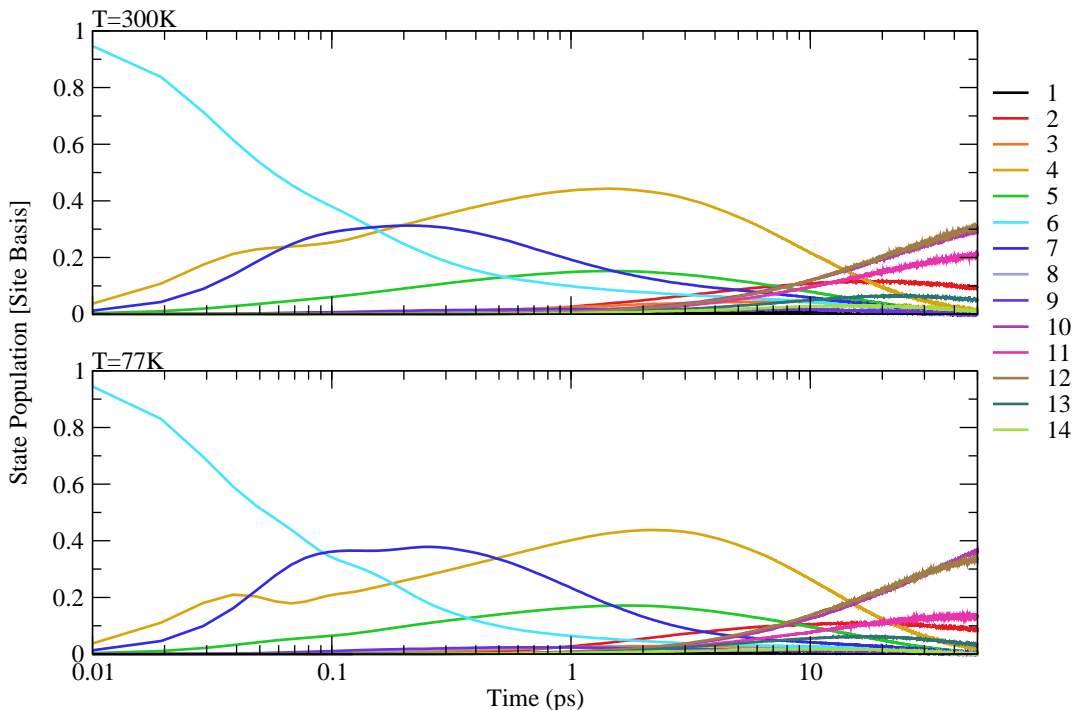
Figure 4.5: The real-time dynamics in the LHCII monomer with an initial excitation on site 6. The parameters describing the Debye spectral density are, for the characteristic bath frequency (ω_c), $100 cm^{-1}$ and, for the reorganization energy (λ), $85 cm^{-1}$. The top panel corresponds to the dynamics at room ($T = 300K$) temperature and the bottom panel is at cryogenic ($T = 77K$) temperature.

When the initial excitation is on site 6 the population is rapidly transferred when compared to an initial excitation on site 1. The real-time dynamics that occur with an initial excitation on site 6 are similar for both temperatures. The population decays quickly off the site 6 onto sites 4 and 7, site 6 no longer has the highest population by around 0.1 picoseconds. The population on site 6 will then be significantly depleted by 1 picosecond. Site 5 will also act as a transient site but will reach a lower maximum population than sites 4 and 7; these two sites will receive a large percentage of the population and represent considerable transition sites for the exciton. It is only after approximately 2 picoseconds that the exciton population increased on sites 10, 11 and 12. These sites will receive the majority of the population at the end of the

simulation. The dynamics of the excitation energy transfer depend on the choice of the initial site but the ending sites for the exciton are the same.
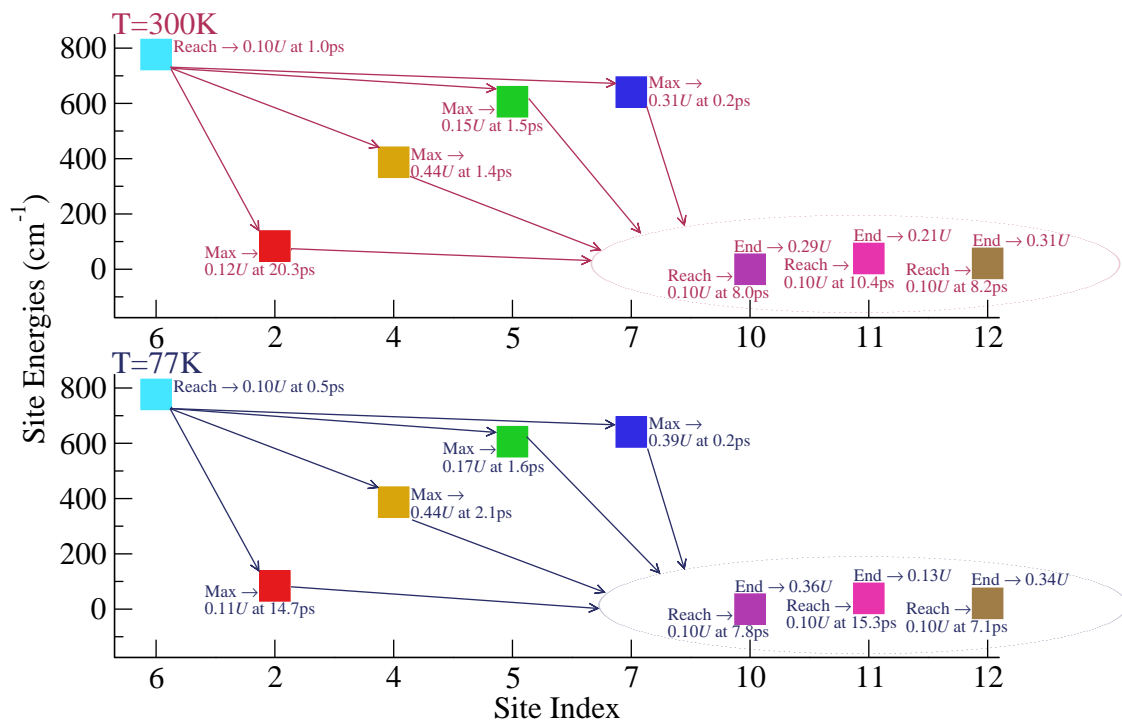
Figure 4.6: Mechanistic summary of the excitation energy transfer in the LHCII monomer with an initial excitation on site 6. The top and bottom panel correspond to the dynamics at room and cryogenic temperature, respectively. The panels are arranged such that the initially excited state is on the left, the transiently populated sites occupy the middle and the ending sites are encased in an ellipse and are found to the right. The text inserts are a selection of extracted population (U) and time (t) data.

Figure 4.6 summarizes the transport mechanism with an initial excitation on site 6; again only the sites with a substantial population are included and this comprises 2, 4, 5, and 7 as the transition sites and 10, 11 and 12 as the ending sites. Again, the basic mechanism is equivalent for both temperatures with only slight variations. One difference in the dynamics between the two temperatures, is that at $T = 77K$, sites 5 and 7 reached a larger maximum population of 0.17 and 0.39 compared to 0.15 and 0.31 at $T = 300K$. Additionally, at the colder temperature, site 11 received

a lower population at the end of the simulation. Site 2 will reach a similar maximum population of 0.12 and 0.11 at a time of 20.3ps and 14.7ps for $T = 300K$ and $T = 77K$, respectively. Even through most of the interesting dynamics of this particular simulation is at a shorter timescale, site 2 represents a small transition site that occurs much later in the dynamics to eventually end up as the fourth highest populated site at the end.

The excitation energy transfer in the full LHCII light harvesting complex was also studied; the same numbering system to identify a particular site in a monomer is used. However, now with three monomers (that compose the full complex) a specific site is differentiated such that site 2 is in monomer 1, site 2' is in monomer 2 and site 2" is in monomer 3. The subsystem Hamiltonian for LHCII is taken from Ref. [52], which has defined three monomers beyond a strictly structural prospective, such that site 1 (located structurally in monomer 1) is included Monomer 3, site 1' is included in Monomer 2 and site 1" is included in Monomer 1. Figure 4.7 contains the flow of the exciton through the three monomers with site 1 (included in Monomer 3) receiving the initial excitation. From this figure it is observed that the excitation energy is transferred to monomer 1, then to a lesser extent to monomer 2, from monomer 3. At the lower temperature, monomers 1 and 2 receive less of the exciton population over the course of the simulation.

In contrast, Figure 4.8 provides more detailed information on the real-time dynamics by depicting the exciton population on a select number of individual sites. The transfer off the site that was initially excited occurs rapidly and by 1 picosecond a significant amount of population has been lost onto site 9", then to site 3" and 8", then to site 2", and finally ending on sites 10" 12" and 11". Monomer 3 contains the significant transient sites for the exciton and the first site that received a considerable portion of the exciton on another monomer is site 2 of monomer 1.

For the LHCII monomer, the application of the FBTS method is able to illustrate that the choice of initial site is independent for the final sites that receive the majority of the population under the timescale that was simulated. However, the choice of initial site did lead to two distinct mechanisms for the excitation energy transfer; wherein, when site 1 was excited the decay of the exciton population from this site was significantly longer than in the case for site 6. Even through the LHCII natural light
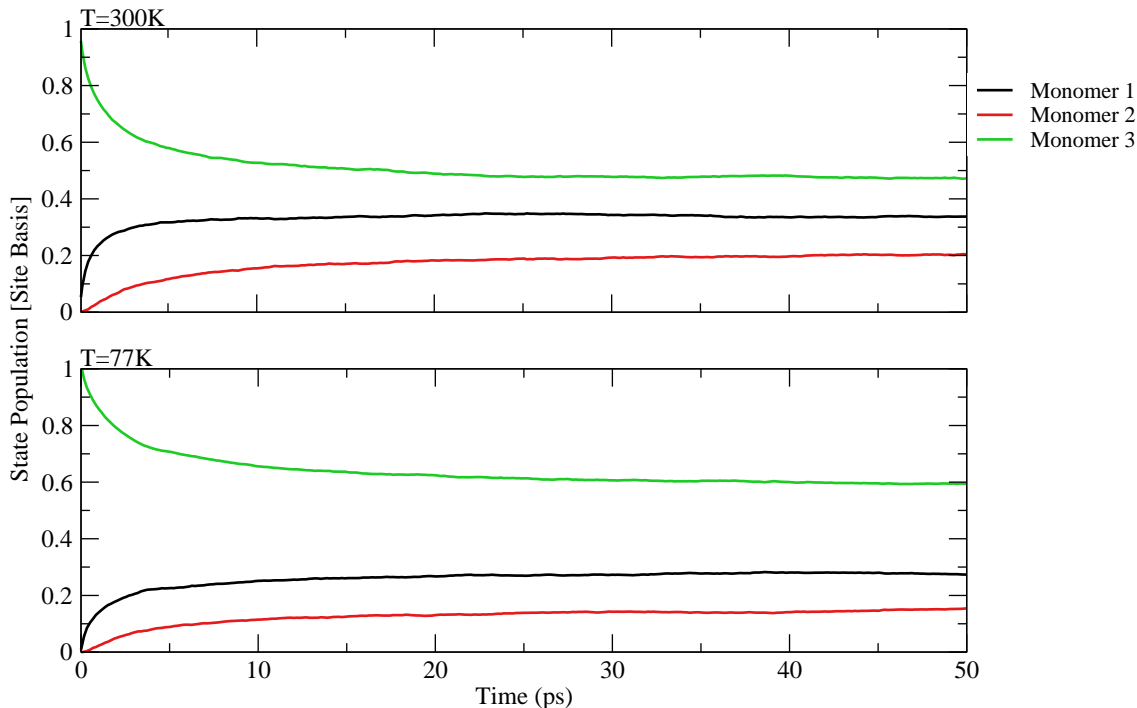
Figure 4.7: The real-time dynamics in the LHCII trimer with an initial excitation on site 1. The subsystem Hamiltonian is organized such that monomer 1 contains site 1", monomer 2 contains site 1' and monomer 3 contains site 1. The aggregated population dynamics for each of the three monomers at room ($T = 300K$) temperature is in the top panel and at cryogenic ($T = 77K$) temperature is in the bottom panel. The parameters describing the Debye spectral density are, for the characteristic bath frequency (ω_c), $100cm^{-1}$ and, for the reorganization energy (λ), $85cm^{-1}$.

harvesting complex is composed of many sites with each pigment in some capacity coupled to the other pigments, not all the sites are unitised in the pathway for the exciton. Through a comparison of the excitation energy transfer in the previously studied exciton dimer model (Chapter 3), the dynamics in the LHCII monomer occurs on a longer timescale; with a simulation of 50 picoseconds insufficient to capture the steady state values.
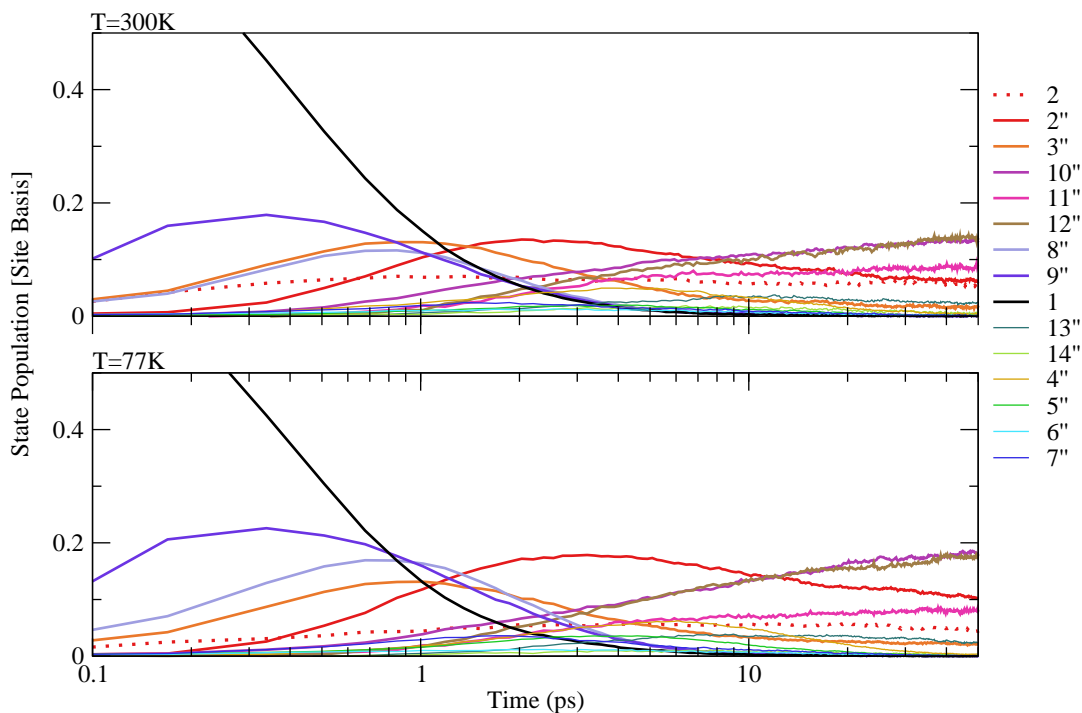
Figure 4.8: The real-time dynamics in the LHCII trimer with an initial excitation on site 1. A site in monomer (1, 2, 3) is defined as (1, 1', 1"). The subsystem Hamiltonian is organized such that monomer 1 contains site 1", monomer 2 contains site 1' and monomer 3 contains site 1. This figure only contains the population dynamics of the sites contained in monomer 3 and site 2 of monomer 1. The parameters describing the Debye spectral density are, for the characteristic bath frequency (ω_c), $100 cm^{-1}$ and, for the reorganization energy (λ), $85 cm^{-1}$. The top panel corresponds to the dynamics at room $(T = 300K)$ temperature and the bottom panel is at cryogenic $(T = 77K)$ temperature.

4.2 CP26

4.2.1 Description of the Structure

For CP26, a minor light harvesting complex in the plant photosynthetic apparatus, there are only 13 chlorophyll pigments total. The protein scaffold and position of these pigments are provided in Figure 4.9 [12]. In this complex, sites 2, 3, 4, 8, 9, 10, 11, 12, 13, and 14 are chlorophyll A and sites 1, 5, 6, and 7 are chlorophyll B. The relationship between the notation used in this thesis and the literature is also provided in Appendix B in Table B.2.
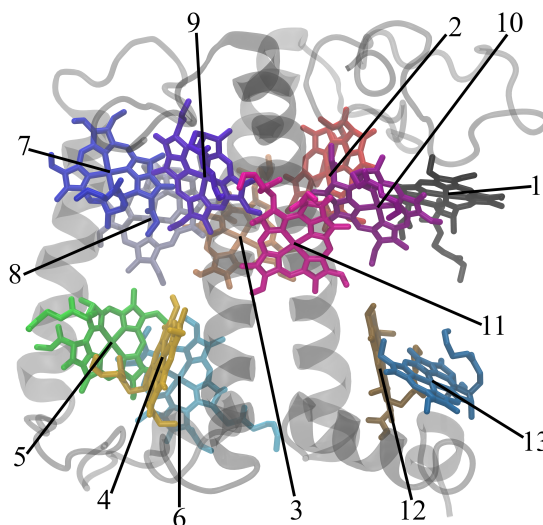
Figure 4.9: Depiction of the CP26 light harvesting complex from spinach; wherein the coloured molecules are the pigments and the grey structure is the protein. There are 13 chlorophyll pigments in the CP26 labelled from 1 to 13 in this thesis. Sites 1, 5, 6, 7 are chlorophyll B and sites 2, 3, 4, 8, 9, 10, 11, 12, 13 are chlorophyll A. The intersection between the chosen labelling convention and the alternate one found in the literature is provided in Table B.2 of Appendix B. This structure was adapted from RCSB PDB (rcsb.org) of PDB ID: 3jcu [12] using VMD [57].

The subsystem Hamiltonian was calculated by Khokhlov et. al. [59] and with this information the dynamics of this complex can be studied and some preliminary transfer mechanisms of the exciton determined. Figure 4.10 contains the relative site energies and intersite couplings in this natural light harvesting complex. From Figure 4.10, it is observed that the pigments with the highest energies are 1 and 7 (chlorophyll B), and the pigments with the lowest energy are 8 and 12 (chlorophyll A). This
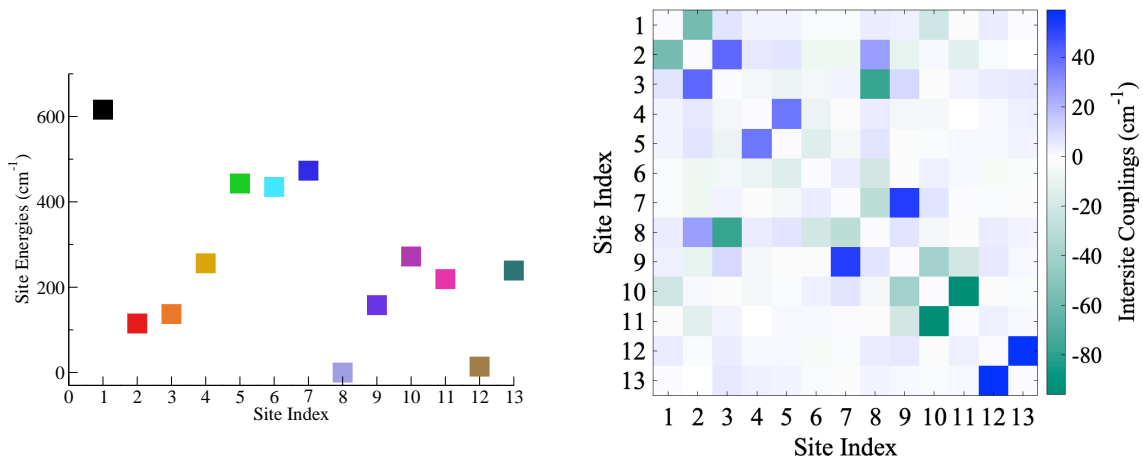
Figure 4.10: Energetic landscape of CP26 with the site energies on the left and the intersite couplings on the right for each of the 13 pigment given in units of cm^{-1} [59]. These are the relative site energies with respect to the lowest lying pigment, in this instance site 8. The magnitude of the intersite coupling between each pigment is represented by a colour tone between green and blue, with the more vivid the colour corresponding to a larger negative or positive number, respectively. For CP26 the sites 1, 5, 6, and 7 are chlorophyll B and sites 2, 3, 4, 8, 9, 10, 11, 12, and 13 are chlorophyll A. The exact subsystem Hamiltonian is provided in Table C.4 from Appendix C.

subsystem Hamiltonian is provided in Appendix C in Table C.4. The parameters that characterize the approximate Debye spectral density for the CP26 complex are the same as was used previously for the investigation into the dynamics of the LHCII light harvesting complex [51]. Specifically, $100cm^{-1}$ for the characteristic bath frequency and $85cm^{-1}$ for the reorganization energy.

4.2.2 Excitation Energy Transfer Mechanisms

The excitation energy transfer mechanisms in the CP26 light harvesting complex was similarly studied with two initial conditions and two temperatures. The sites chosen to receive the initial excitation again possessed the highest site energy: sites 1 and 7. The results from the FBTS method applied to the CP26 system with an initial excitation on site 1 (a chlorophyll B) at two different temperatures, room ($T = 300K$) and cryogenic ($T = 77K$), is provided in Figure 4.11.
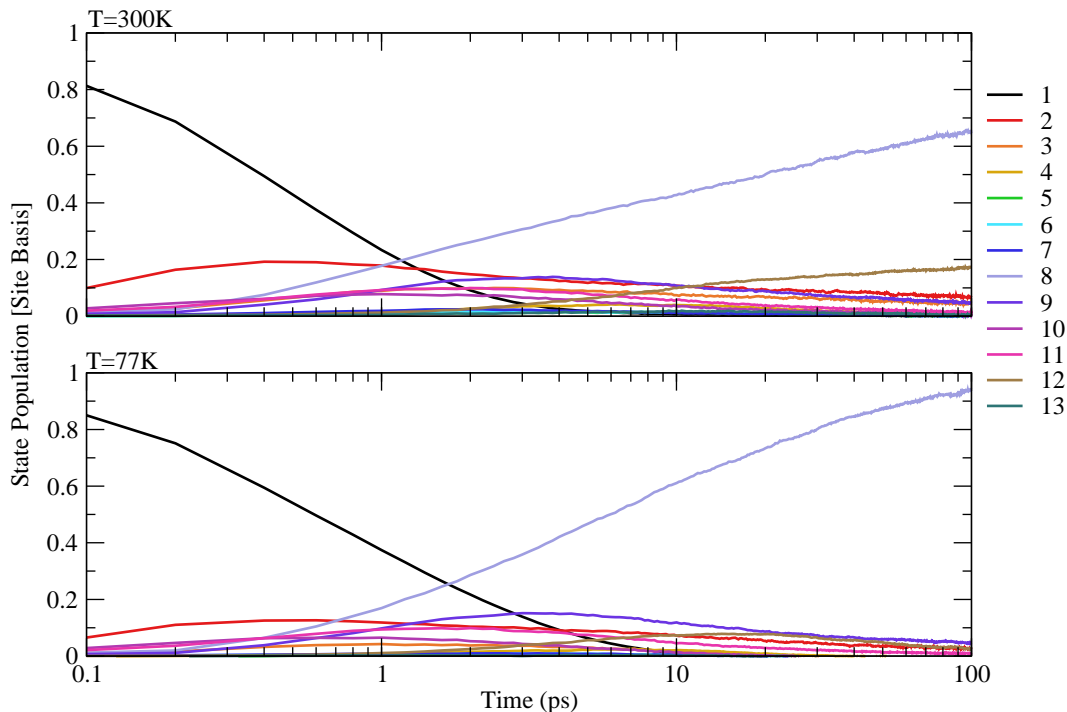
Figure 4.11: The real-time dynamics in CP26 with an initial excitation on site 1. The parameters describing the Debye spectral density are, for the characteristic bath frequency (ω_c), $100cm^{-1}$ and, for the reorganization energy (λ), $85cm^{-1}$. The top panel corresponds to the dynamics at room $(T = 300K)$ temperature and the bottom panel is at cryogenic $(T = 77K)$ temperature.

As the population on the site 1 decreased, the next site that received a significant population is site 2. This site will act as a short transient site for the exciton as it hits a maximum population below 1 picosecond. Site 9 will also act a transient site, albeit a small one since the ending site for the majority of the exciton will maintain the highest population with certainty after 2 picoseconds for both temperatures for the rest of the simulation. For CP26, (under these simulation conditions) there is a clear ending site for the exciton on site 8, which began increasing in population below 1 picosecond and continued to grow over 100 picoseconds. The real-time dynamics are similar between the two temperatures, the most notable difference is that at room temperature the exciton ends on site 8, with a much smaller but still considerable

population on site 12; while at cryogenic temperature the ending site is clearly site 8 and received a larger portion of the exciton population.
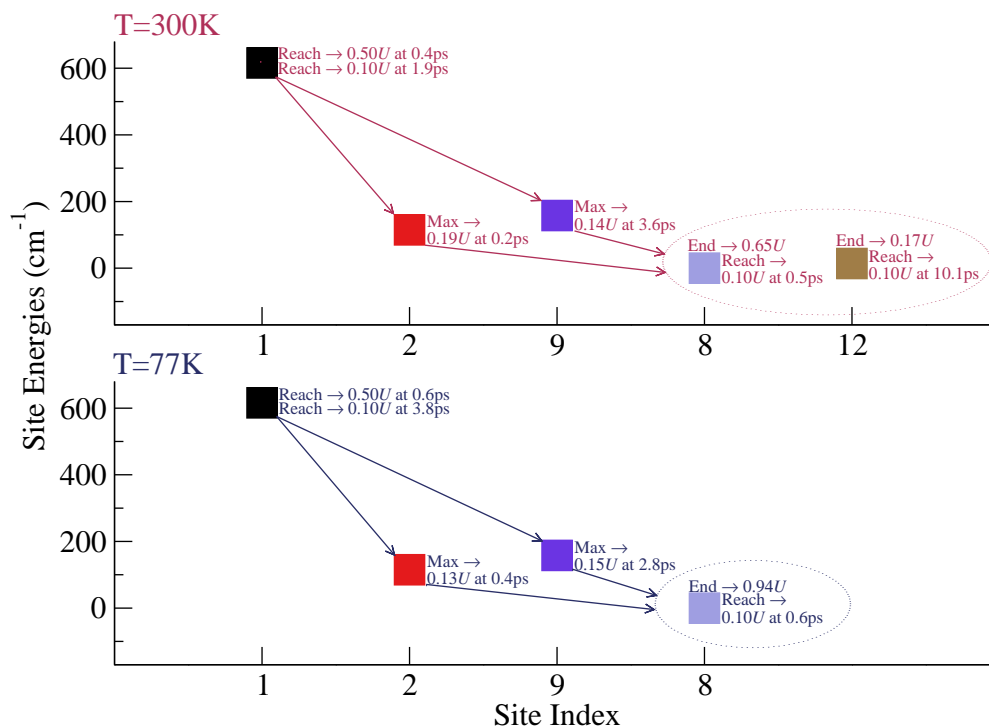
Figure 4.12: Mechanistic summary of the excitation energy transfer in CP26 with an initial excitation on site 1. The top and bottom panel correspond to the dynamics at room and cryogenic temperature, respectively. The panels are arranged such that the initially excited state is on the left, the transiently populated sites occupy the middle and the ending sites are encased in an ellipse and are found to the right. The text inserts are a selection of extracted population (U) and time (t) data.

Figure 4.12 contains the basic mechanism of transfer in CP26 with an initial excitation on site 1. From this figure additional differences between the transfer of the excitation energy at the two temperatures can be clarified; such as the slower decrease in the population on site 1 at cryogenic temperature, at room temperature site 1 reached 0.10 population at 1.9 picoseconds as opposed to 3.8 picoseconds. As previously noted, only a select number of sites have a significant role in the real-time dynamics, with most sites maintaining a low population. Figure 4.12 in particular

highlights sites 1, 2, 8, 9 and 12 for the dynamics at room temperature and only sites 1, 2, 8 and 9 at cryogenic temperature.

The real-time dynamics with a different site for the initial excitation, in this case site 7, is contained in Figure 4.13. A few details are similar to the previous mechanism of transfer, the short timescale for the decay for the initially excited site, having lost a considerable amount of the population by 1 picosecond. Along with the participation of site 9 as a transient site and that the ending site for the exciton are sites 8 and 12 at room temperature and only site 8 at cryogenic temperature.
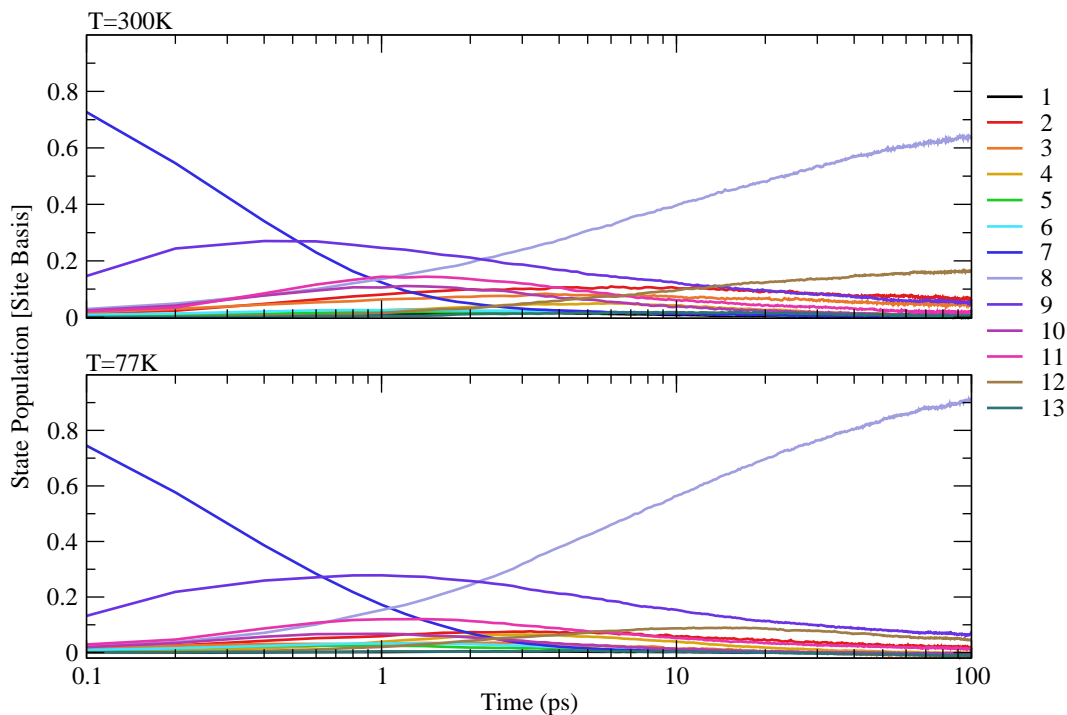
Figure 4.13: The real-time dynamics in CP26 with an initial excitation on site 7. The parameters describing the Debye spectral density are, for the characteristic bath frequency (ω_c), $100cm^{-1}$ and, for the reorganization energy (λ), $85cm^{-1}$. The top panel corresponds to the dynamics at room ($T = 300K$) temperature and the bottom panel is at cryogenic ($T = 77K$) temperature.

The excitation energy transfer mechanism is captured in Figure 4.14. The basic mechanism at both temperatures can be summarized as follows, the initially excited

site 7 decays as a portion of the population goes onto site 9 and finally onto site 8, the primary ending location. Site 9 is a transient site for the exciton and receives the largest amount of the population excluding the beginning and ending sites. This maximum population is 0.27 at room temperature and 0.28 at cryogenic temperature and this value is reached quickly at 0.2 and 0.8 picoseoncds, respectively. The mechanistic picture between room and cryogenic temperature provided in Figure 4.14 is notably different; however, this is due to the fact that at room temperature there are 3 additional transient sites that received a population marginally above 0.10 (the designated exciton population cut-off to be included in the mechanism diagrams in this thesis). These sites are 2, 10 and 11 which will all reach a maximum population of 0.11, 0.11 and 0.14 then experience a decay. At a cryogenic temperature the transient sites are 9 and 11, with both receiving a similar maximum population as was observed previously at room temperature. In the case of site 11 this maximum value of the population is 0.12. Otherwise, the other sites that were involved in the transfer mechanism at room temperature do not attain a significant population at the lower temperature.
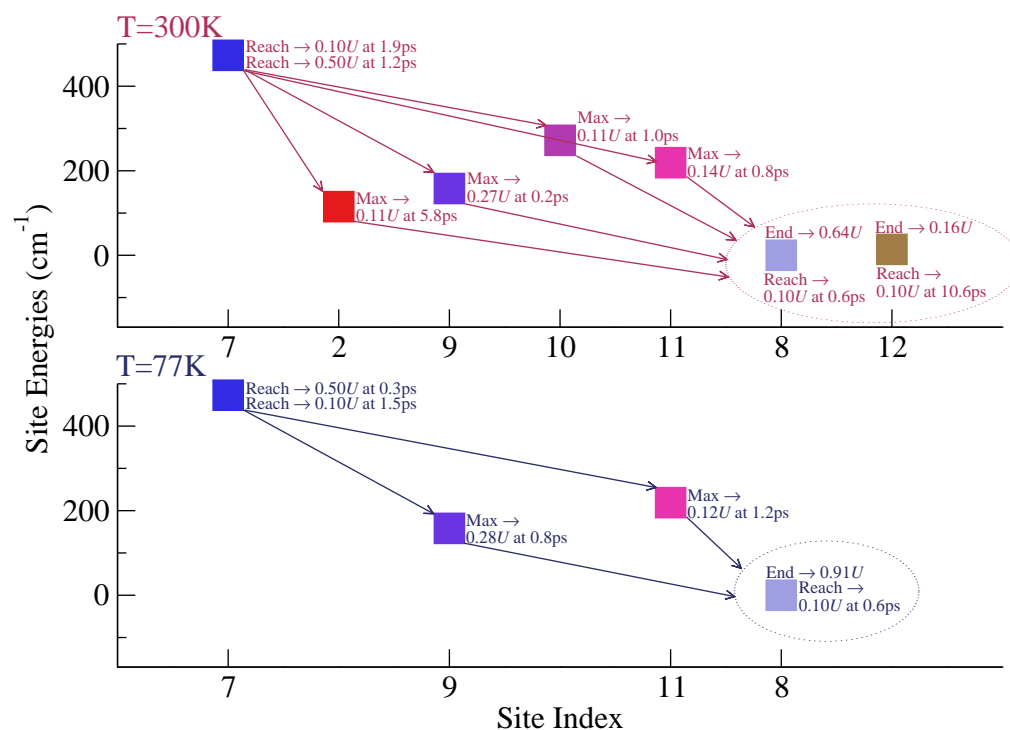
Figure 4.14: Mechanistic summary of the excitation energy transfer in CP26 with an initial excitation on site 7. The top and bottom panel correspond to the dynamics at room and cryogenic temperature, respectively. The panels are arranged such that the initially excited state is on the left, the transiently populated sites occupy the middle and the ending sites are encased in an ellipse and are found to the right. The text inserts are a selection of extracted population (U) and time (t) data.

The mechanism of excitation energy transfer with two initial conditions and using two different temperatures was determined through an analysis of the simulations provided by the FBTS method. Again in CP26 as in LHCII the timescale for the dynamics were in the tens of picoseconds. It was observed that independent of initial site, the exciton ended on site 8, a chlorophyll A pigment with the lowest site energy, and a lower temperature resulted in a higher ending population on this site. One difference in the comparison between the real-time dynamics between LHCII and CP26 is in the ending location for the exciton, in the case of CP26 the majority of the population clearly ended up on a single site.

Chapter 5

Bacterial Light Harvesting Complexes

The bacterial light harvesting complexes in Green Sulfur Bacteria allow for survival in environments with little access to light [60,61]. Figure 5.1 depicts the basic spatial organization of this photosystem composed of the chlorosome, Fenna-Matthews-Olson (FMO) protein and the reaction centre [62,63]. The organisation of the movement of the excitation energy through this apparatus is the collection by the chlorosome, and the transfer through the baseplate to the FMO complex and into the reaction centre [64]. This is all facilitated by the bacteriochlorophyll pigments present in the photosynthetic apparatus (not depicted in Figure 5.1).

It is the organization of these pigments that make the chlorosome unique among known biological light harvesting complexes. This can be illustrated through a comparison with the other light harvesting complex in Green Sulfur Bacteria, FMO, which embodies typical structural features. FMO contains 24 bacteriochlorophylls, the previously studied complexes, LHCII and CP26, had 42 and 13 pigments; the chlorosome can contain up to six figures of bacteriochlorophylls [62, 63, 65]. More notably, these pigments are arranged as tubes and sheets all without a protein scaffold, which is found in FMO [63, 65–67]. For many years crystallography research has provided structural information on the FMO light harvesting complex; this level of detail is not available for the chlorosome [63, 68]. However, representative models have been constructed and the excitation energy transfer examined [67, 69]. In this work we utilized the models from the Celardo group [45]. Similar tubular strucutres of pigments can be experimentally crafted and obtaining a fuller understanding of the excitation energy transfer in this efficient natural chlorosome system can provide a foundation for applications in artificial light harvesting [70].

In this chapter two natural light harvesting complexes will be studied, FMO and the chlorosome. For the FMO light harvesting complex an overview of the structure is followed by an investigation into the mechanisms of excitation energy transfer.
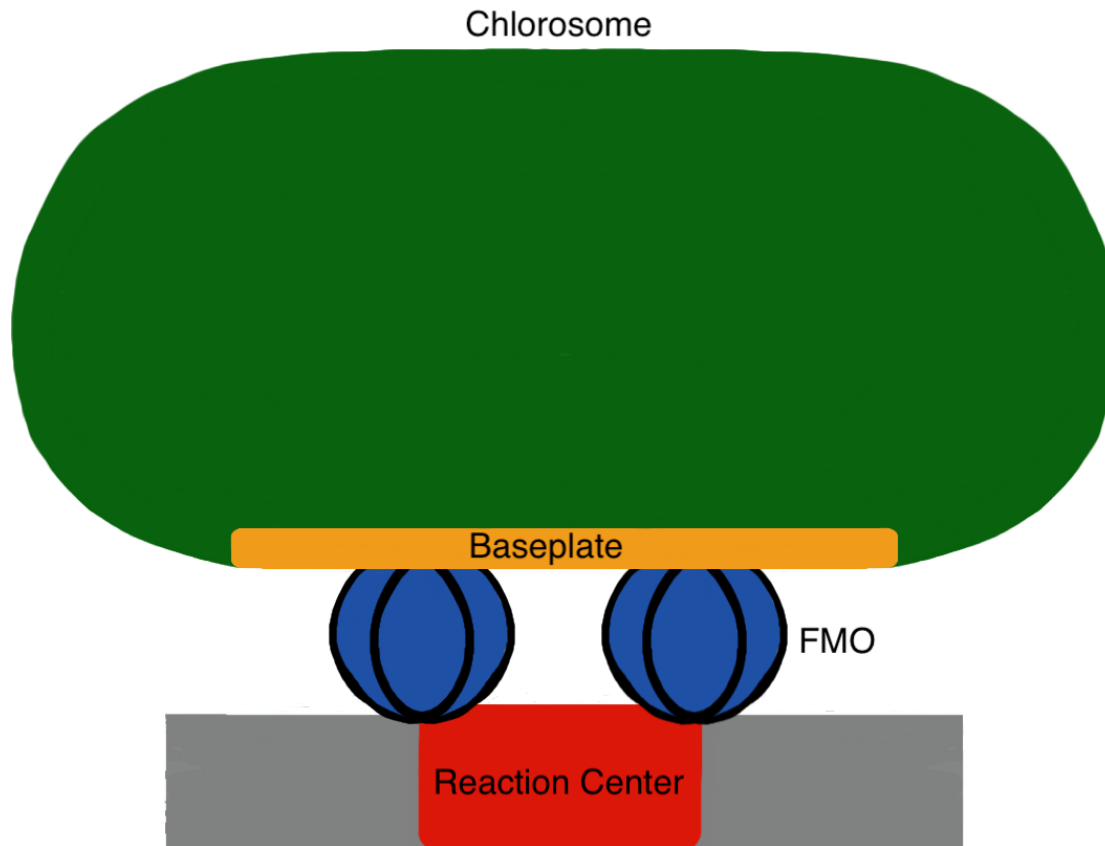
Figure 5.1: Basic cartoon diagram of the light harvesting apparatus in Green Sulfur Bacteria [62].

A benchmark of the FBTS method was completed with this complex. The many degrees of freedom that result as a consequence of the numerous pigments in the chlorosome can be numerically challenging but the approximate nature and thus lower computational cost of the FBTS method provided an opportunity to investigate the dynamics. A discussion of the structural models used to represent the chlorosome are included and a particular focus was placed on the characterization of the spread of the excitation energy through these models.

5.1 FMO

5.1.1 Description of the Structure

In Figure 5.2 the eight bacteriochlorophyll A pigments that comprise one monomer of the FMO trimer light harvesting complex are concisely labelled [65]. The presence

of the eighth pigment was determined after much research was already completed on a model that contained 7 pigments per monomer [71–75]. A graphical representation of the 7-site FMO model subsystem Hamiltonian used in Ref. [28] and from Ref. [76] is provided in Figure 5.3. This subsystem Hamiltonian is provided in Appendix C in Table C.5. From this figure it can be observed that the highest site energy pigments are 2 and 6. The lowest site energy pigment is 3 and from the intersite couplings it is most strongly coupled to site 4.
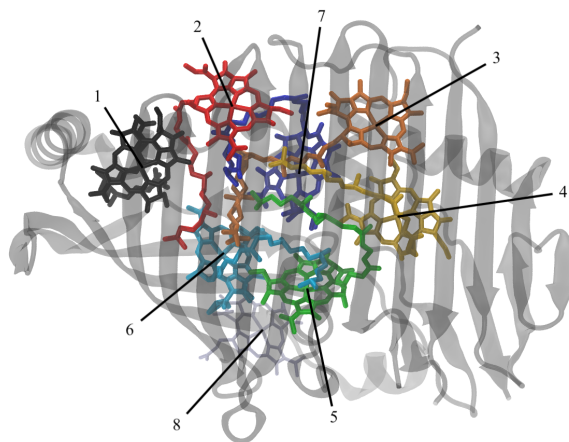
Figure 5.2: Depiction of the FMO monomer from *Chlorobaculum tepidum*; wherein the coloured molecules are the pigments and the grey structure is the protein. Each of the 8 pigments are bacteriochlorophyll A. This structure was adapted from RCSB PDB (rcsb.org) of PDB ID: 3eni [65] using VMD [57].
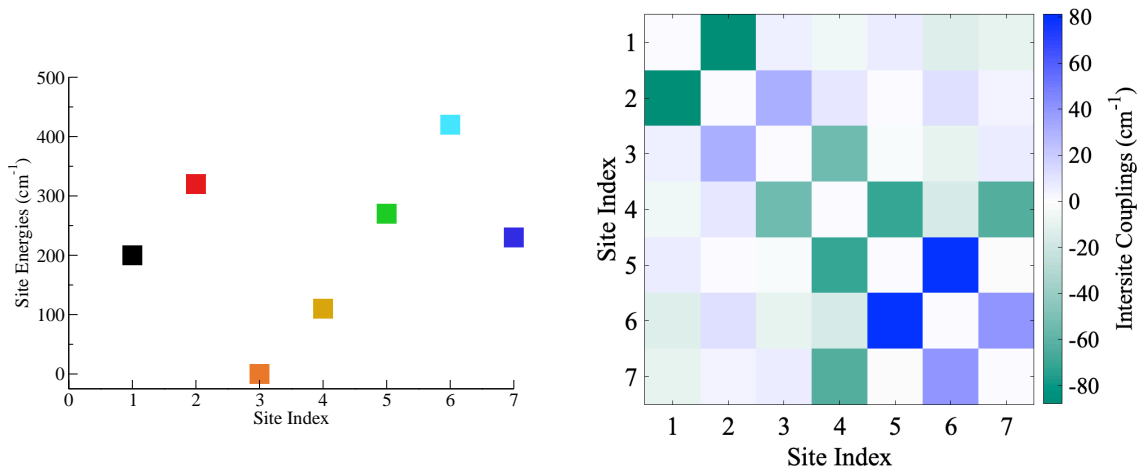
Figure 5.3: Energetic landscape for the 7-site FMO model with the site energies on the left and the intersite couplings on the right given in units of cm^{-1} [28] [76]. These are the relative site energies with respect to the lowest lying pigment, in this instance site 3. The magnitude of the intersite coupling between each pigment is represented by a colour tone between green and blue, with the more vivid the colour corresponding to a larger negative or positive number, respectively. The exact subsystem Hamiltonian is provided in Table C.5 from Appendix C.

An alternative subsystem Hamiltonian was used for the investigation into the excitation energy transfer in an isolated 8-site monomer and the full trimer structure of the FMO light harvesting complex [47, 77, 78]. From the graphical representation for the 8-site monomer subsystem Hamiltonian in Figure 5.4, the pigment with the highest site energy is 7; conversely, sites 3 and 5 had the lowest site energy. The divergence in the energetic landscapes of the site energies for the 7-site and 8-site systems is due to two alternative approaches to the calculation. The intersite couplings reveal that the eighth pigment is strongest coupled to site 1. All simulations in this chapter use the parameters for the Debye spectral density as outlined in Ref. [28], which correspond to a value of $106.18cm^{-1}$ for the characteristic bath frequency and $35cm^{-1}$ for the reorganization energy.
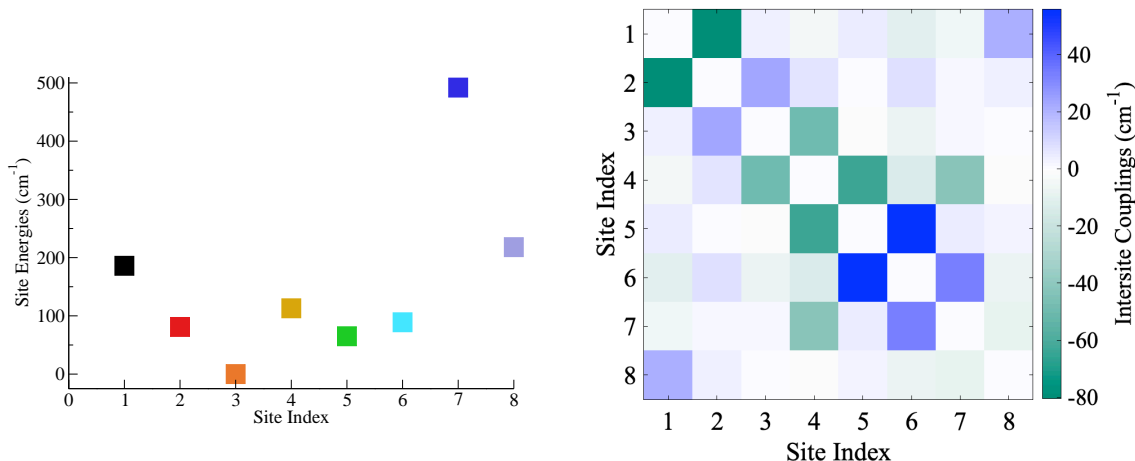
Figure 5.4: Energetic landscape for the 8-site FMO model with the site energies on the left and the intersite couplings on the right given in units of cm^{-1} [47,77]. These are the relative site energies with respect to the lowest lying pigment, in this instance site 3. The magnitude of the intersite coupling between each pigment is represented by a colour tone between green and blue, with the more vivid the colour corresponding to a larger negative or positive number, respectively. The exact subsystem Hamiltonian is provided in Table C.6 from Appendix C.

5.1.2 Excitation Energy Transfer Mechanisms

7-site FMO Model

The real-time dynamics of the FMO 7-site model were studied with the FBTS method using two different initial conditions for the excitation (sites 1 and 6) and two different temperatures (room and cryogenic, $T{=}300K$ and $T{=}77K$, respectively). These chosen conditions emulate Wilkins and Dattani [29] which completed a study of the 7-site FMO model using the HEOM method. This provides an useful benchmark for this approximate method since a natural light harvesting complex contains a more complicated energetic and spatial landscape as opposed to the simple exciton dimer model.

Figure 5.5 contains the excitation energy transfer through the FMO 7-site model with an initial excitation on site 1, where the solid line corresponds to the FBTS results and the dashed line the HEOM results. The top panel contains the simulation of the real-time dynamics at room temperature. The sites that participate in the transfer are 1, 2, 3 and 4; whereas there is minimal involvement from sites 5, 6, and

7. As the initial population in site 1 decreases the population in site 2 increases. Below 1 picosecond the population oscillates between site 1 and site 2 and after experiences a steady decay on both of these sites. The population in sites 3 and 4 will increase at approximately the same time and will continue until reaching a steady-state population. The majority of the exciton ends up on site 3; with a lower but still significant population on site 4. The population of the other sites at the end of this simulation will occupy an approximate range between 0.1 and 0.04 for the exciton population.

The bottom panel of Figure 5.5 contains the excitation energy transfer with the only change being the temperature, to cryogenic ($T=77K$). In this instance the sites that participate in the mechanism are 1, 2 and 3; site 4 does not receive a significant population over the course of the simulation. Again, oscillations between the population of sites 1 and 2 occur below 1 picosecond. These oscillations are noticeably more numerous and pronounced. The major difference between the real-time dynamics between the two temperatures is that a larger share of the exciton ends on site 3.

In order to provide a more succinct summarization of the mechanism of the excitation energy transfer in the 7-site FMO model the results from Figure 5.5 are simplified in Figure 5.6. In this case the excitation begins on site 1, transiently populates site 2 and ends on sites 3 and 4 at room temperature. A similar mechanism occurs at cryogenic temperature but without a significant participation from site 4. At the higher temperature the population in site 1 decreases by half quicker than at lower temperatures. However, both reach a maximum population for site 2 at the same time. A more quantitative picture is provided in how the excitation energy is spread between the sites for the two temperatures, at room temperature site 4 has approximately one half the population in site 3 and at lower temperatures the population on site 3 is approximately double what it was at room temperature. From the way that this mechanism graph is organised it is possible to make some clear observations with respect to the relative energies of the sites involved in the excitation energy transfer. Even through site 2 is higher in energy then site 1, this local energy barrier is overcome resulting in an ending population on the two lowest energy sites in the model, sites 3 and 4.

Additionally, the real-time dynamics of the 7-site FMO model when the initial
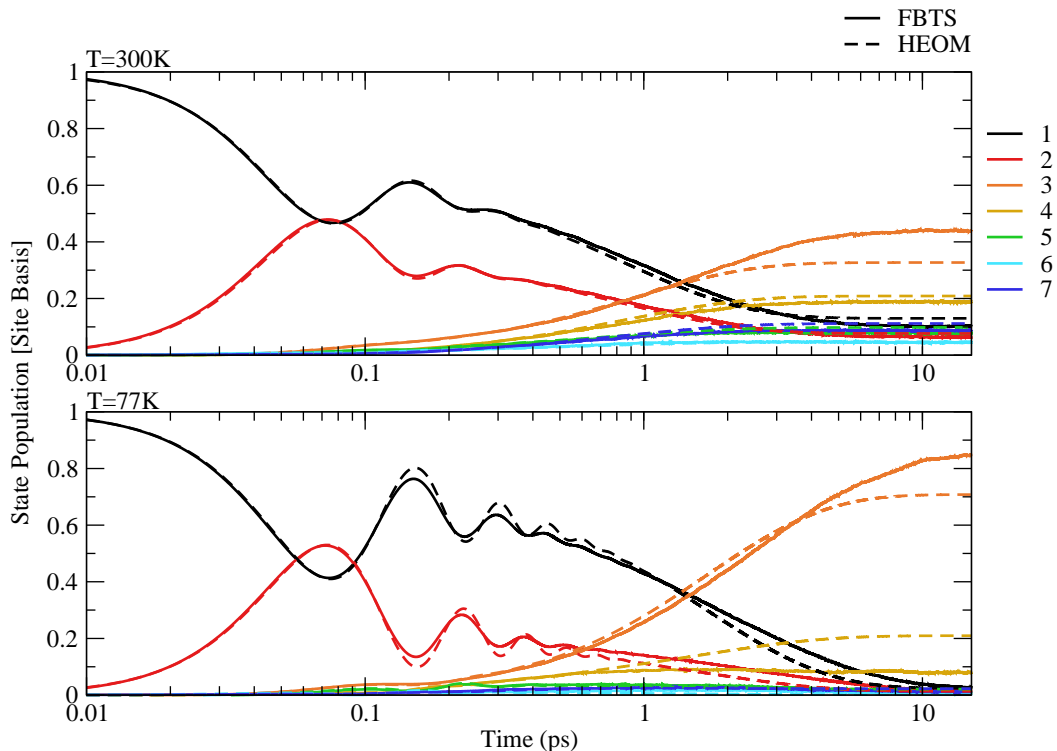
Figure 5.5: Comparison of the excitation energy transfer between the HEOM and FBTS theoretical methods for the 7-site FMO model with an initial excitation on site 1. The HEOM results were obtained from Ref. [29]. The parameters describing the Debye spectral density are, for the characteristic bath frequency (ω_c), $106.18cm^{-1}$ and, for the reorganization energy (λ), $35cm^{-1}$. The top panel corresponds to the dynamics at room ($T = 300K$) temperature and the bottom panel is at cryogenic ($T = 77K$) temperature.

excitation was placed on site 6, (the site with the highest relative site energy) is provided in 5.7. The excitation energy transport has changed; at room temperature the major sites that partake in the transfer are sites 5, 6, 7, 3 and 4. Sites 1 and 2 no longer attain a significant population. An oscillation of the population is again observed to occur below 1 picosecond but in this instance the oscillation is between sites 5 and 6 with a small contribution from site 4. As site 6 decreases in population the first site to gain in population is site 5, followed closely by sites 4 and 7 that begin to grow in population below 0.1 picoseconds. The majority of the excitation ends on site 3, with a portion on site 4.
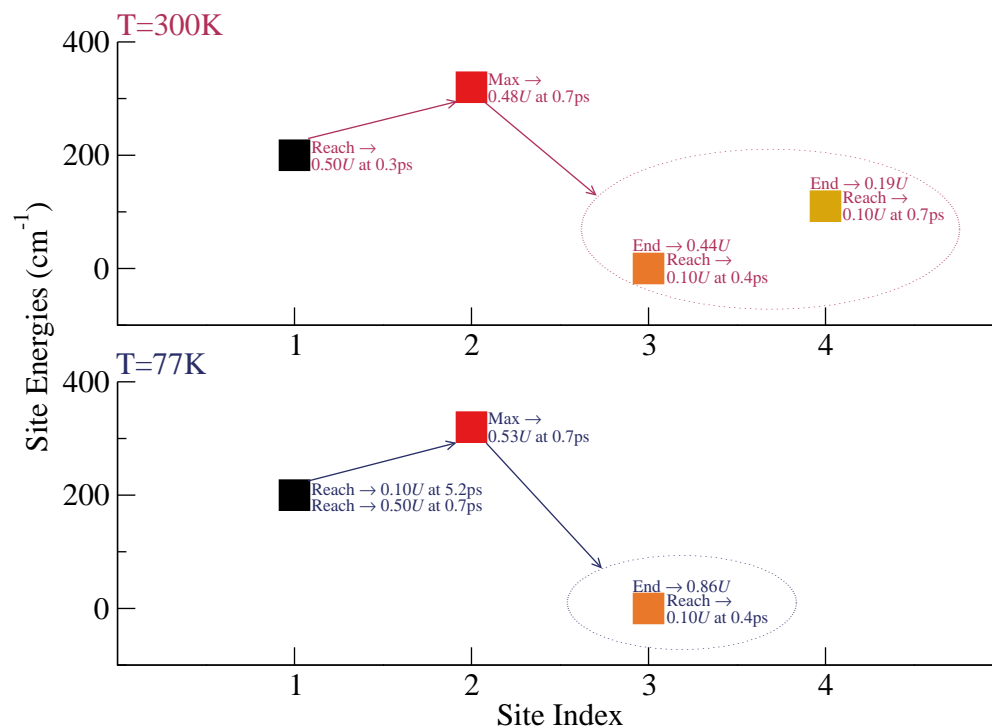
Figure 5.6: Mechanistic summary of the excitation energy transfer in the 7-site FMO model with an initial excitation on site 1. The top and bottom panel correspond to the dynamics at room and cryogenic temperature, respectively. The panels are arranged such that the initially excited state is on the left, the transiently populated sites occupy the middle and the ending sites are encased in an ellipse and are found to the right. The text inserts are a selection of extracted population (U) and time (t) data.

The bottom panel of Figure 5.7 contains the real-time dynamics wherein the temperature has been set to $T{=}77K$. A notable difference are the more numerous and larger oscillations between sites 5 and 6. Additionally, site 4 no longer has a significant exciton population at the end of the simulation and has taken on the characteristics of a transient state, reaching a maximum then decreasing.
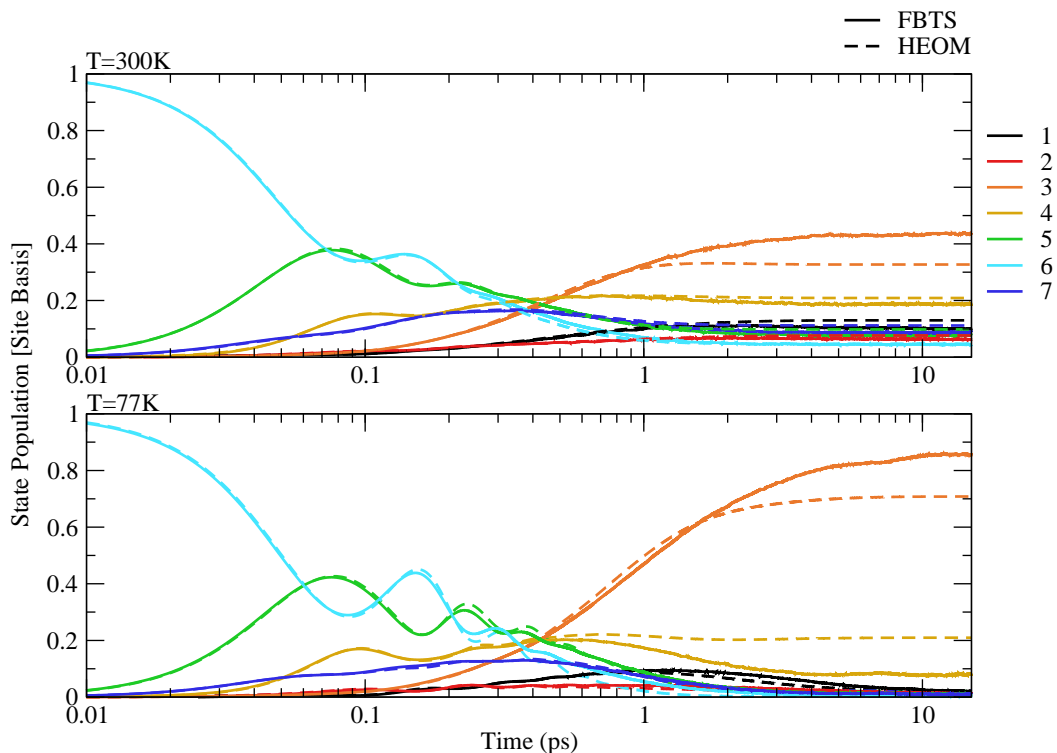
Figure 5.7: Comparison of the excitation energy transfer between the HEOM and FBTS theoretical methods for the 7-site FMO model with an initial excitation on site 6. The HEOM results were obtained from Ref. [29]. The parameters describing the Debye spectral density are, for the characteristic bath frequency (ω_c), $106.18cm^{-1}$ and, for the reorganization energy (λ), $35cm^{-1}$. The top panel corresponds to the dynamics at room ($T = 300K$) temperature and the bottom panel is at cryogenic ($T = 77K$) temperature.

Figure 5.8 contains the mechanistic details from Figure 5.7 for the transfer at room and cryogenic temperature that occupy the top and bottom panel, respectively. The excitation energy transfer with an initial excitation on site 6 involves more sites. At room temperature the transitional sites are 5 and 7; wherein site 5 received a more significant portion of the excitation, having reached a max population of 0.38, compared to 0.16 for site 7. The ending sites are 3 and 4 at room temperature. At the lower temperature, the mechanism slightly changes: site 4 no longer receives a significant portion of the exciton at the end of the simulation and is thus not included in the ellipse of Figure 5.8 but is now present as a transient site in the mechanism.

The maximum population for transient sites are quickly reached, occurring below 0.5 picoseconds.

Figure 5.8: Mechanistic summary of the excitation energy transfer in the 7-site FMO model with an initial excitation on site 6. The top and bottom panel correspond to the dynamics at room and cryogenic temperature, respectively. The panels are arranged such that the initially excited state is on the left, the transiently populated sites occupy the middle and the ending sites are encased in an ellipse and are found to the right. The text inserts are a selection of extracted population (U) and time (t) data.

The comparison of the FBTS and HEOM method in the 7-site FMO model for all the conditions under study reveals good agreement at short time scales and a deviation at longer time scales; this discrepancy must stem from the approximate nature of the FBTS method. The other benchmark comparison completed within this thesis on the exciton dimer model (Chapter 3) was only at room temperature and therefore did not provide an opportunity to comment on the accuracy of the FBTS method under different temperatures. Here for the 7-site FMO model it was

observed that the dynamics at the higher temperature are in better agreement then the colder temperature. Thus, this shows that the FBTS method provides sufficiently accurate results. Since the focus of this research is on the real-time dynamics and not obtaining the steady state population this method captures the area of greatest interest. Comparing the two initial conditions, the choice does not affect the ending place of the excitation population. Comparing the two temperatures, the presence of the larger and more numerous oscillations at lower temperature reveals that the greater effect of the bath dampens these oscillations. Additionally, the ending site receives a different spread of the population on the sites. In the 7-site system, there is clear directed transport with the initial excitation on a site. The excitation energy is not simply populated and explores every single complex in the model.

8-site FMO Model

In the case of the 8-site FMO model, the real-time dynamics were investigated similarly using two different initial conditions and temperatures. However, the initial excitation was placed on site 1 and site 8; whereas site 8 has been suggested to be the connection for the excitation energy from the chlorosome [71, 72]. Figure 5.9 contains the results from the FBTS method for an initial excitation on site 1, the top and bottom panel corresponds to room ($T{=}300K$) and cryogenic temperature ($T{=}77K$), respectively. The dynamics of the eighth site is represented by the light purple line.

With an initial excitation on site 1 there is a quick and oscillatory exchange to site 2 within the first picosecond. Sites 3 and 8 begin to increase in population as sites 1 and 2 decrease. Site 3 will continue to gain in population before reaching a steady state, while site 8 will be a transient state for the population. Sites 4, 5 and 6 will also slowly increase in population before reaching a steady state. Finally, site 7 will contain the lowest amount of the exciton at the end of the simulation. Site 3 will end with the majority of the exciton, followed by site 5.

Upon the temperature being lowered to $T = 77K$, again there is a quick exchange from site 1 to site 2, with a more pronounced oscillatory behaviour with the population. Site 8 is again a transient state for the excitation but the main difference between the two sets of real-time dynamics for these conditions is in the ending populations for the exciton. Site 3 will end with a significant majority of the exciton,

Figure 5.9: The real-time dynamics in the 8-site FMO model with an initial excitation on site 1. The parameters describing the Debye spectral density are, for the characteristic bath frequency (ω_c), $106.18 cm^{-1}$ and, for the reorganization energy (λ), $35 cm^{-1}$. The top panel corresponds to the dynamics at room ($T = 300K$) temperature and the bottom panel is at cryogenic ($T = 77K$) temperature.

followed by site 5. Sites 4, 5, and 7 do not receive a significant portion of the exiton population over the course of the simulation. With an initial excitation on site 1 in the FMO 8-site model, the mechanism of exciton transport is summarized in Figure 5.10.

The basic mechanism for the 8-site FMO model with an initial excitation on site 1, is for site 2 and 8 to act as transient states, with site 2 being dominant. Site 2 will reach a maximum population of 0.52 and 0.61 at room and cryogenic temperature, respectively. Even through site 8 possesses a site energy greater then for site 1 it still acts as a transient site. The majority of the excitation ended up on site 3, more prominently at a lower temperature with a exciton population of 0.61 compared
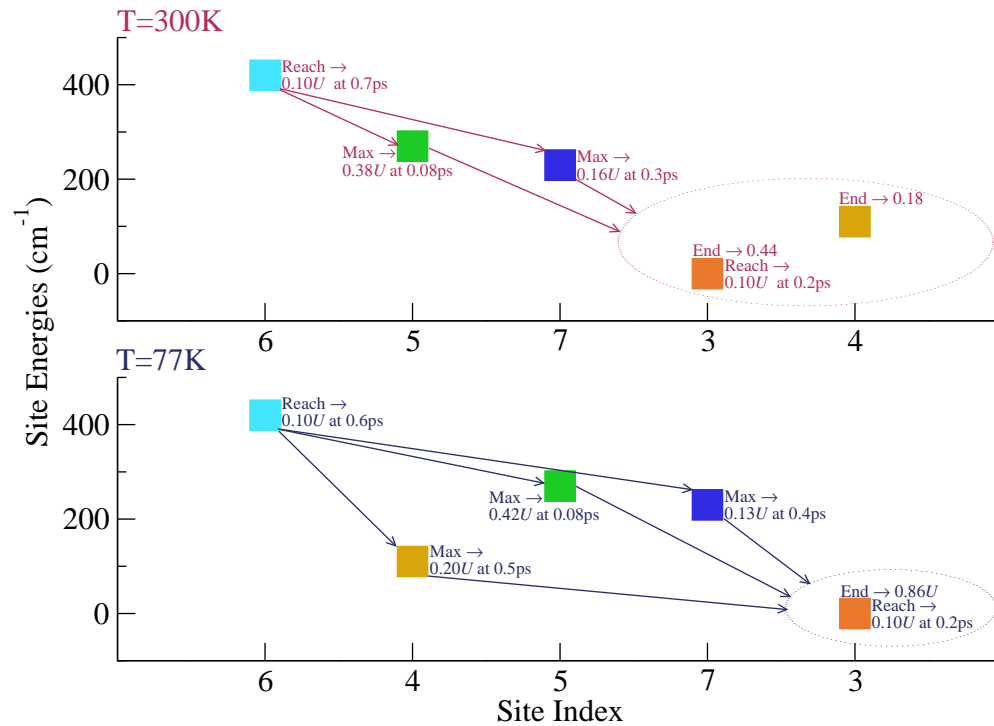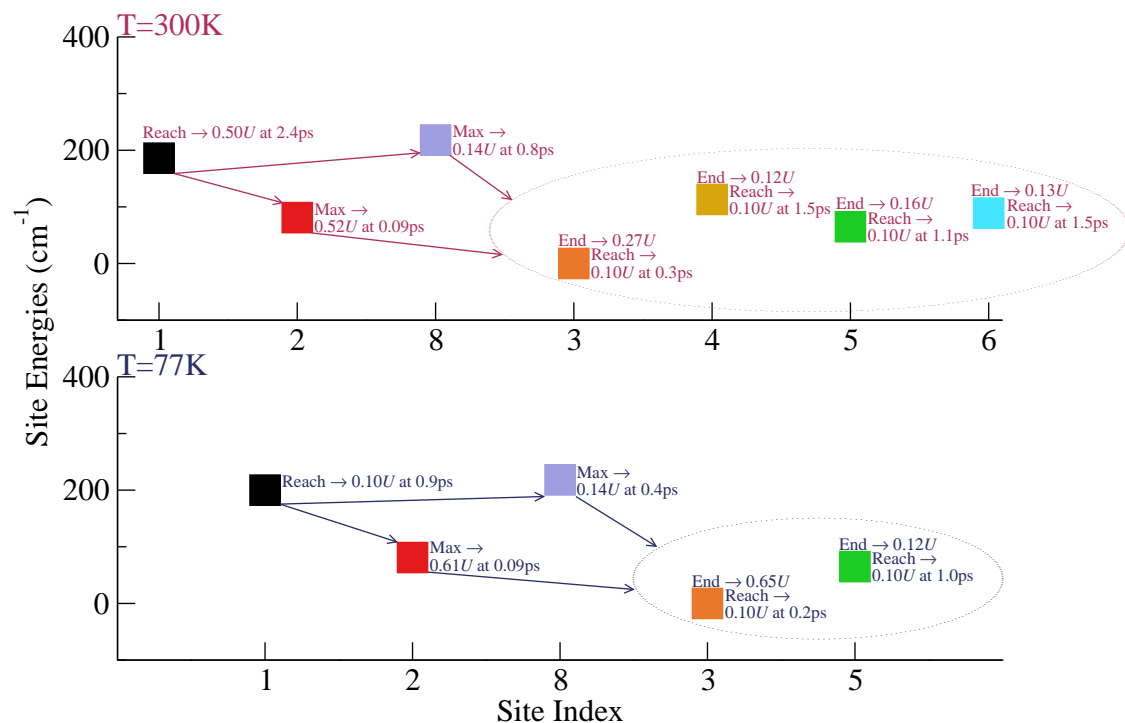
Figure 5.10: Mechanistic summary of the excitation energy transfer in the 8-site FMO model with an initial excitation on site 1. The top and bottom panel correspond to the dynamics at room and cryogenic temperature, respectively. The panels are arranged such that the initially excited state is on the left, the transiently populated sites occupy the middle and the ending sites are encased in an ellipse and are found to the right. The text inserts are a selection of extracted population (U) and time (t) data.

to 0.27 at room temperature, followed by site 5. This is the mechanism at both temperatures. At the higher temperature, other sites, 2 and 6, receive a significant amount of a population at the end.

In the case of an initial excitation on site 8 at room temperature, the real-time dynamics of which are provided in the top panel of Figure 5.11, there is no more oscillatory behaviour in the dynamics, site 8 still has a significant population at 1 picosecond and will reach a population of 0.10 at 3.7 picoseconds. Site 2 will reach the second largest population of 0.21 over the course of the dynamics and represents a transition state along with site 1. The majority of the exciton will end up on site 3

but there is a close spread with the exciton population on sites 4, 5 and 6 at the end.
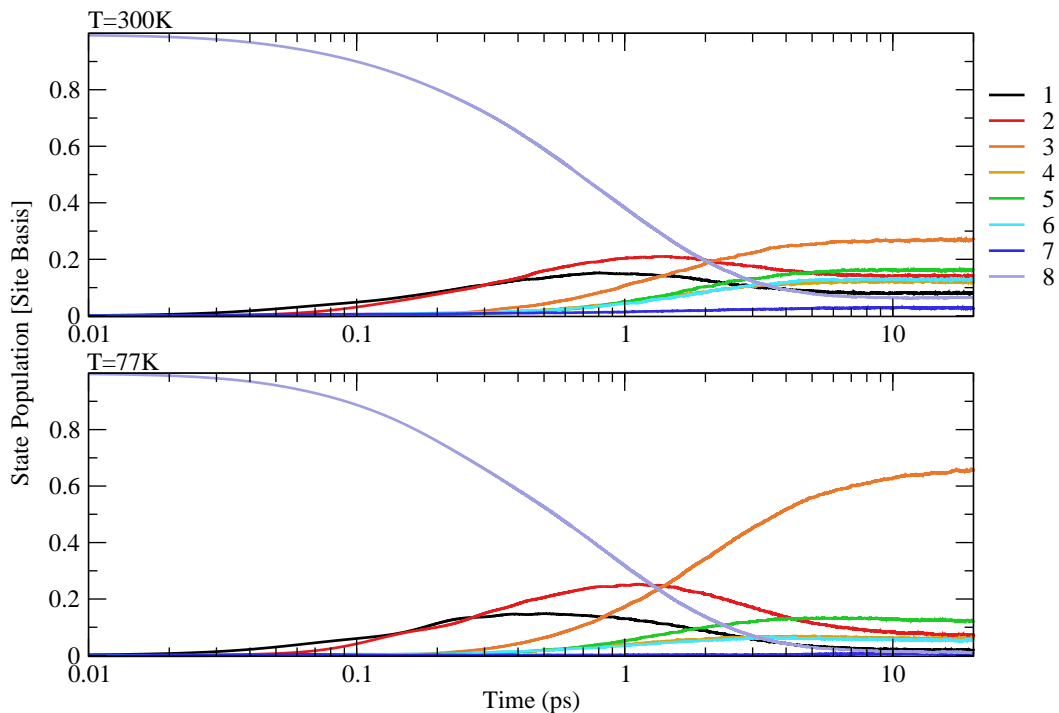
Figure 5.11: The real-time dynamics in the 8-site FMO model with an initial excitation on site 8. The parameters describing the Debye spectral density are, for the characteristic bath frequency (ω_c), $106.18cm^{-1}$ and, for the reorganization energy (λ), $35cm^{-1}$. The top panel corresponds to the dynamics at room ($T = 300K$) temperature and the bottom panel is at cryogenic ($T = 77K$) temperature.

In the case of the simulation with a temperature of $77K$, (the bottom panel of Figure 5.11) the major difference is that the more of the exciton ends up on site 3, 0.66 compared to 0.27, and sites 4 and 6 no longer receive a significant ending exciton population. Once again there is minimal participation from site 7. The mechanism of the excitation energy transfer in the FMO 8-site model with an initial exciation on site 8 is summarised in Figure 5.12.
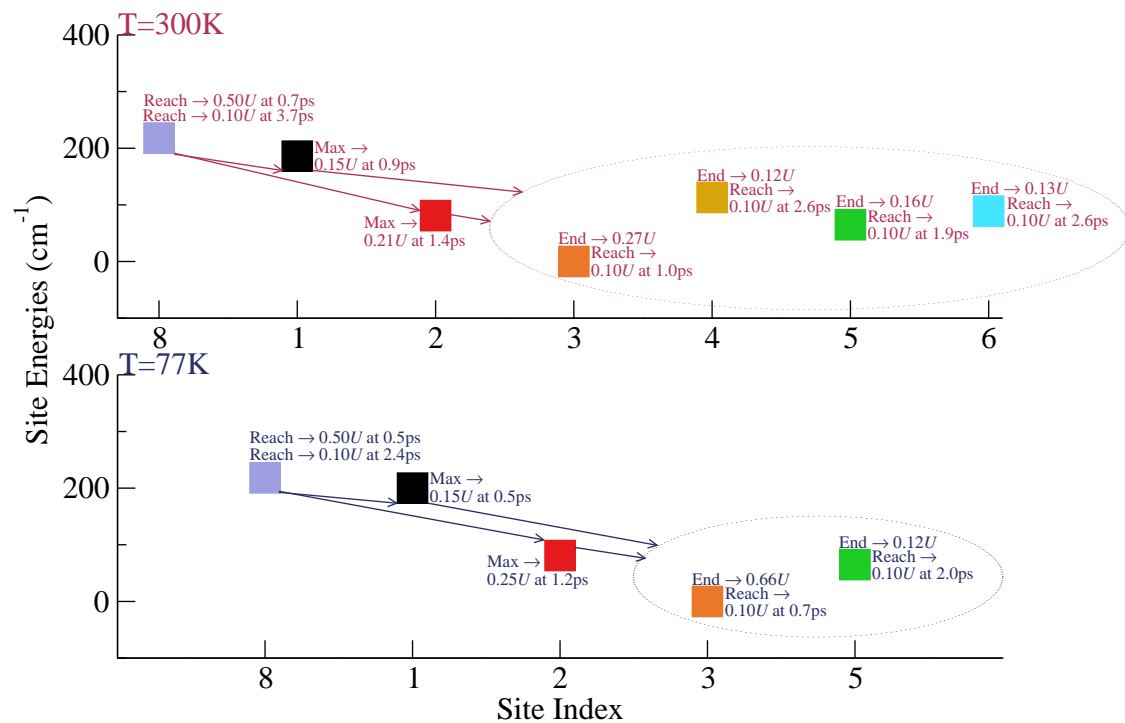
Figure 5.12: Mechanistic summary of the excitation energy transfer in the 7-site FMO model with an initial excitation on site 8. The top and bottom panel correspond to the dynamics at room and cryogenic temperature, respectively. The panels are arranged such that the initially excited state is on the left, the transiently populated sites occupy the middle and the ending sites are encased in an ellipse and are found to the right. The text inserts are a selection of extracted population (U) and time (t) data.

24-site FMO Model

By incorporating the three other monomers in the FMO complex, the FBTS method can be used to simulate the dynamics. With an initial excitation on monomer 1, the next monomer to receive population is monomer 2, followed closely by monomer 3. This is observed at both temperatures; however, at room temperature the population is evenly shared between between all three monomers. At cryogenic temperature, the population transfer is slower and monomer 1 contains a majority of the population by the end.
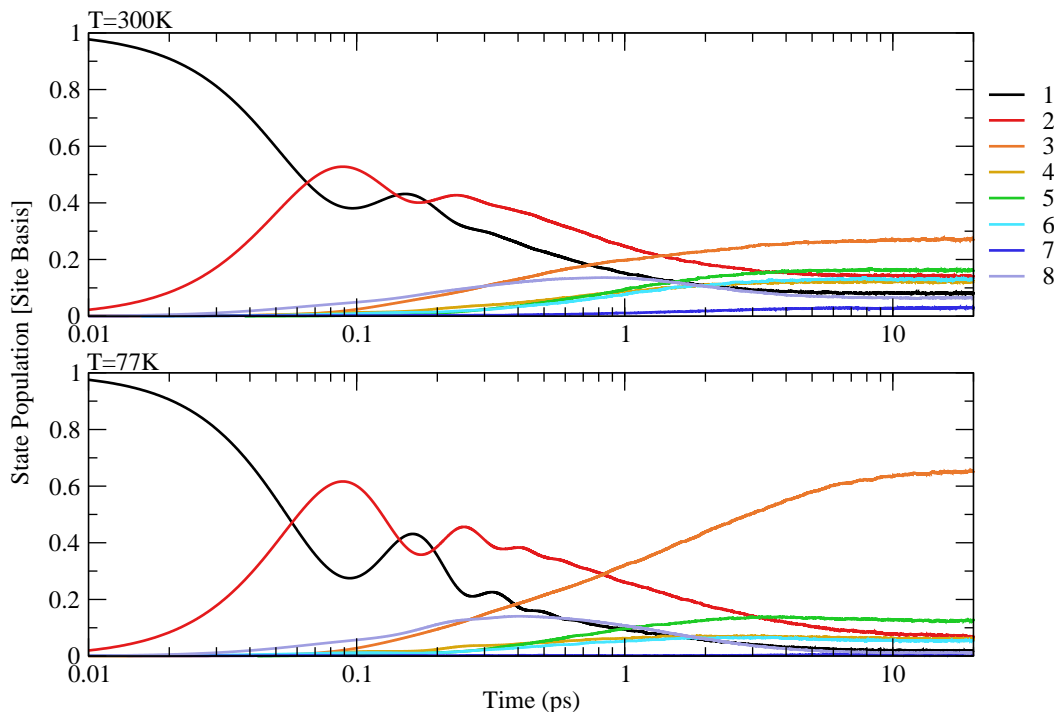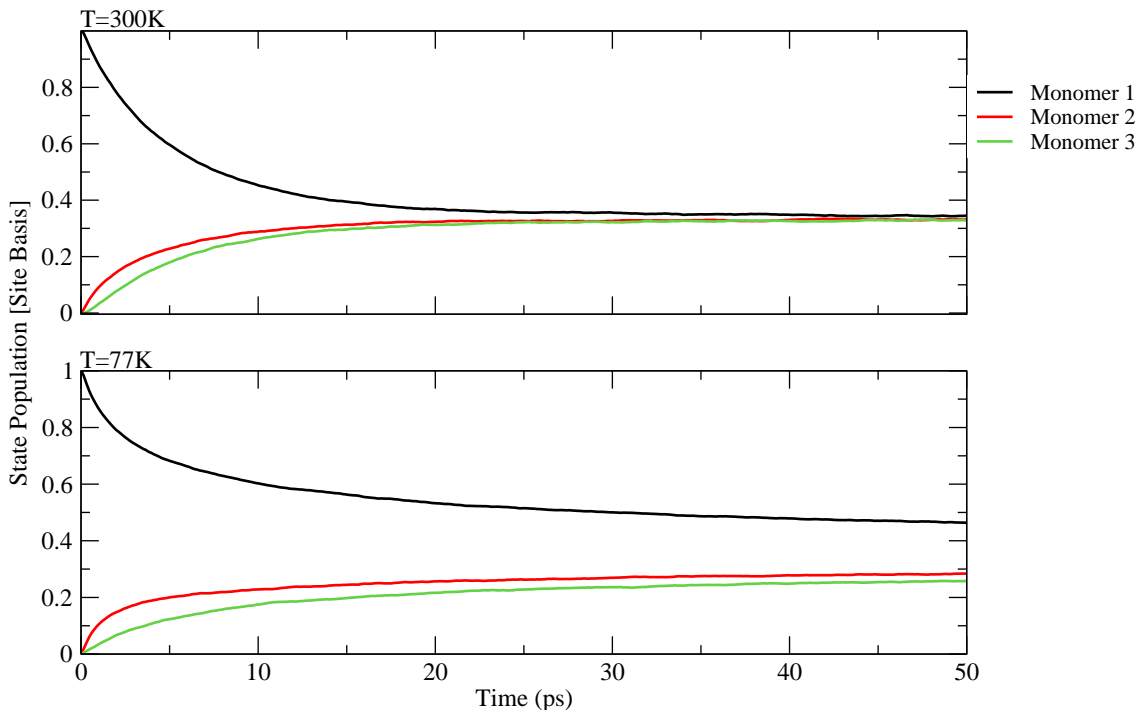
Figure 5.13: The real-time dynamics in the 24-site FMO model with an initial excitation on site 1 in monomer 1. The parameters describing the Debye spectral density are, for the characteristic bath frequency (ω_c), $106.18cm^{-1}$ and, for the reorganization energy (λ), $35cm^{-1}$. The top panel corresponds to the dynamics at room ($T = 300K$) temperature and the bottom panel is at cryogenic ($T = 77K$) temperature.

The FMO represents an important model to study using the FBTS method. This is because previous work exists which effectively compares this approximate method to exact results. This comparison revealed good agreement at shorter times and a deviation at the longer steady state populations. The study of the three different models allowed for an understanding of the excitation energy transfer with a selection of different initial conditions. Upon analysing the dynamics with a colder temperature, in this case $T = 77K$, the biggest difference is the change in the final populations of the sites.

5.2   Chlorosome

5.2.1   Description of the Structure and Construction of the Model

The study of the excitation energy transfer in the chlorosome is a collaborative effort
with the Celardo research group which provided the three structural models under
analysis in this thesis. These models belong to two groups, natural or artificial, but
all share a few core concepts. Each model is a cylinder composed of stacked rings
separated by a distance of 8.3 Å. A ring has a radius of 60 Å and contains sixty
pigments per ring, for a total of N_r rings. Each pigment is described as a dipole
which will have a particular position and orientation in space.

It is the orientation of the pigment dipoles that will primarily differentiate the
three models. For the model that represents the bchQRU triple mutant of the chloro-
some, now referred to as the MT model, the dipoles are alternatively angled into or
out of the ring by 4° and there is a slight twist between rings in the cylinder. The
other two models are created when the pigment dipoles in the stacked rings are ori-
entated to point in the direction of the next ring resulting in the parallel (PD) model
and when each dipole points to the next in the ring resulting in the tangential (TD)
model. Figure 5.2.1 provides a pictorial reference for the organisation of the dipoles
in the three models investigated.
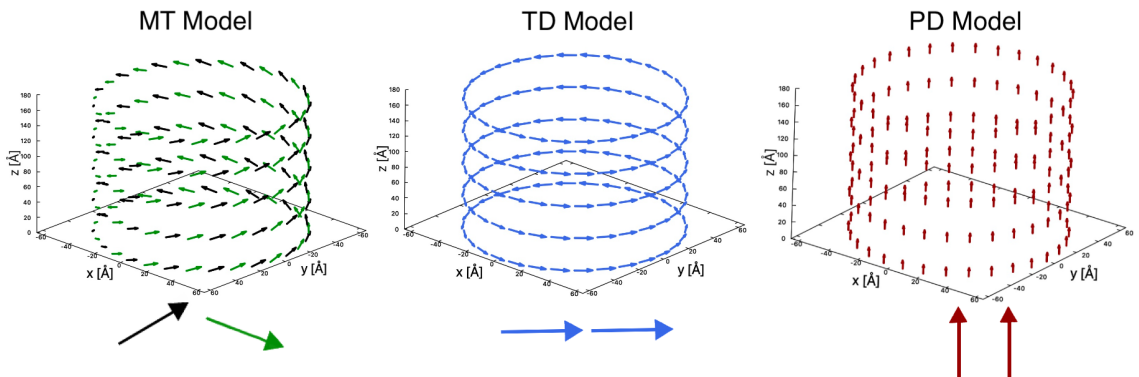
Figure 5.14: Representative picture of the three models studied in this thesis for the
chlorosome, the reader is referred to the work of Celardo et. al. for a full discussion
on the geometry within these models [45]. The number, length and angle (for the
MT model) of the dipoles were chosen to be easily viewed and do not represent the
models used in the simulations.

The description of the position and orientation of the pigment dipoles allows for the calculation of the intersite coupling strengths, that will have an effect on the excitation energy transfer in these models. These couplings will be different for each of the three models. The largest magnitude intersite coupling is provided in Table 5.1. This reveals that the MT model does not possess the strongest coupling between dipoles either in the ring or between rings, those belong to the TD and PD model, respectively. An additional model, termed in the nearest-neighbour (NN) model, is structurally the same to the MT model except the coupling strengths between the pigments that are more then 9 Å apart are artificially set to zero.

	Intersite Coupling in Ring (cm^{-1})	Intersite Coupling between Rings (cm^{-1})
MT	604.22	259.58
PD	834.29	528.27
TD	1251.45	264.12

Table 5.1: The largest magnitude coupling between pigments either in the ring or between the rings in the three models.

5.2.2 Excitation Energy Transfer Mechanisms

We begin the exploration of the excitation energy transfer in the chlorosome light harvesting complex with the real-time dynamics of a single MT model ring composed of sixty sites. Figure 5.15 displays the transfer when a single site in the middle of the ring (site 30) is excited. This system is already the largest presented in the thesis and instead of displaying the exciton population for each site as sixty lines on a graph, an alternative method to display the data is shown in Figure 5.15. The saturation of the colour indicates the magnitude of the population on that particular site at that time. From this figure the transport of the exciton is observed to flow quickly from the initial site to the neighbouring pigments and from there to the next neighbouring pigments. The exciton continues around the ring until the population is evenly spread out between all the sites, this all occurs in a short time frame.
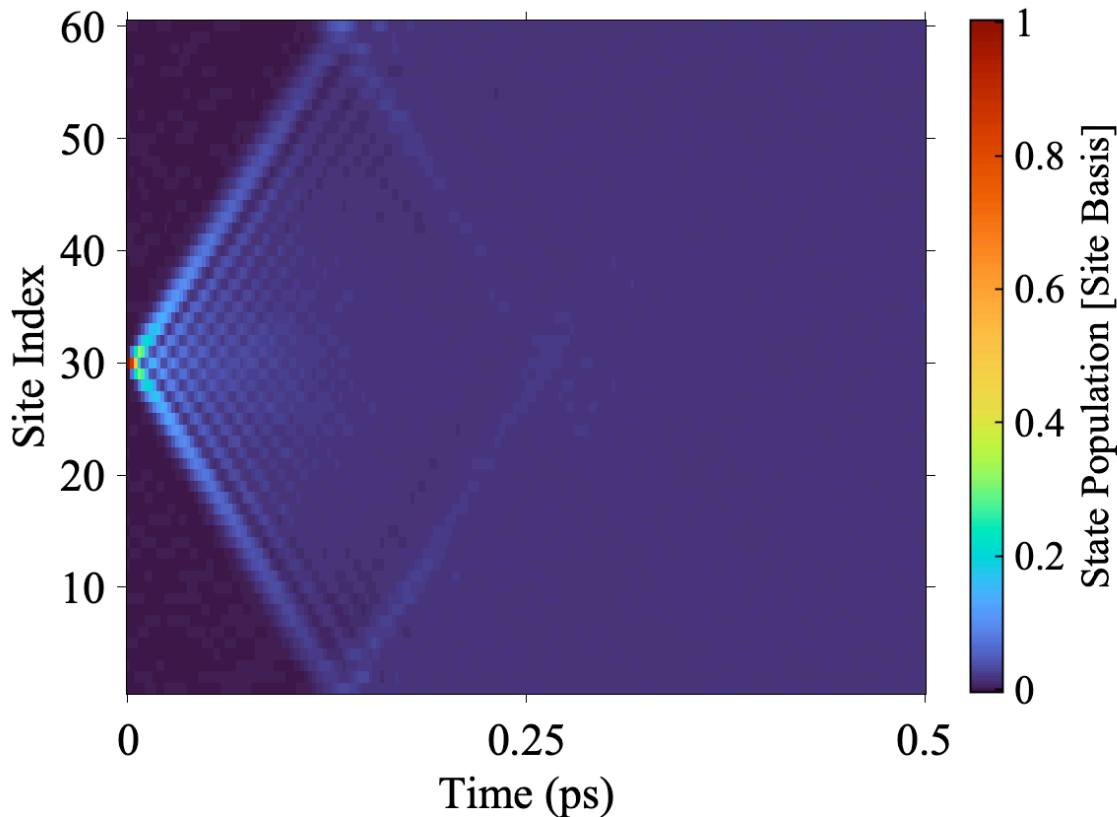
Figure 5.15: The real-time dynamics in a ring of the MT model with an initial excitation on site 30 at room temperature ($T = 300K$). The parameters describing the Debye spectral density are, for the characteristic bath frequency (ω_c), $200.cm^{-1}$ and, for the reorganization energy (λ), $100cm^{-1}$.

The addition of more rings is required in order to compose a cylinder, which will increase of the total number of pigments. A further approximation, known as focused sampling, is introduced to assist in the reduction of the computational strain brought on by the larger systems. Focused sampling affects the initial values of the two sets of coherent state variables $(x, x') = (q, p, q', p')$ that describe the subsystem. For the initially excited site, λ'', the values of $q_{\lambda''}, p_{\lambda''}, q'_{\lambda''}, p'_{\lambda''}$ are sampled from the coordinates of a circle such that: $q^2 + p^2 = 1$. The initial conditions of all other sites are set to zero.

Upon stacking more rings together in the model there will be two directions for the exciton to spread, in a ring and along the cylinder. In order to characterize and compare the excitation energy transfer for the three structural models under

consideration, this thesis focuses primarily on the spread of the exciton down the length of the cylinder. To this end, the Mean Squared Displacement (MSD) is related to this physical transport process and is calculated using equation 5.1 [79]. Wherein, $\rho_{rr}(t)$ is the cumulative population on a particular ring r; L denotes the distance between rings (8.3 Å), finally, r is the position of a particular ring in the cylinder in relation to the ring with the initial excitation.

$$\mathrm{MSD}(t) = \sum_{r}^{N_r} \rho_{rr}(t) r^2 L^2 - (\rho_{rr}(t) r L)^2 \tag{5.1}$$

Figure 5.16 depicts the MSD for a chain of 101 rings with 4 dipoles per ring with a radius of 4 Å orientated in the MT, PD and TD model with three different reorganization energies. The initial excitation is placed on a site in the middle of the cylinder and the spread of the exciton is quick in all three models. By increasing the reorganization energy the MSD curve decreases indicating that the spread of the exciton is slower. The reduction of the speed of the exciton through each cylinder with larger reorganization energies could be due to the localising effect of the bath. It was observed that between the three models, the PD model (with the strongest coupling between rings) has the fastest spread of the exciton.
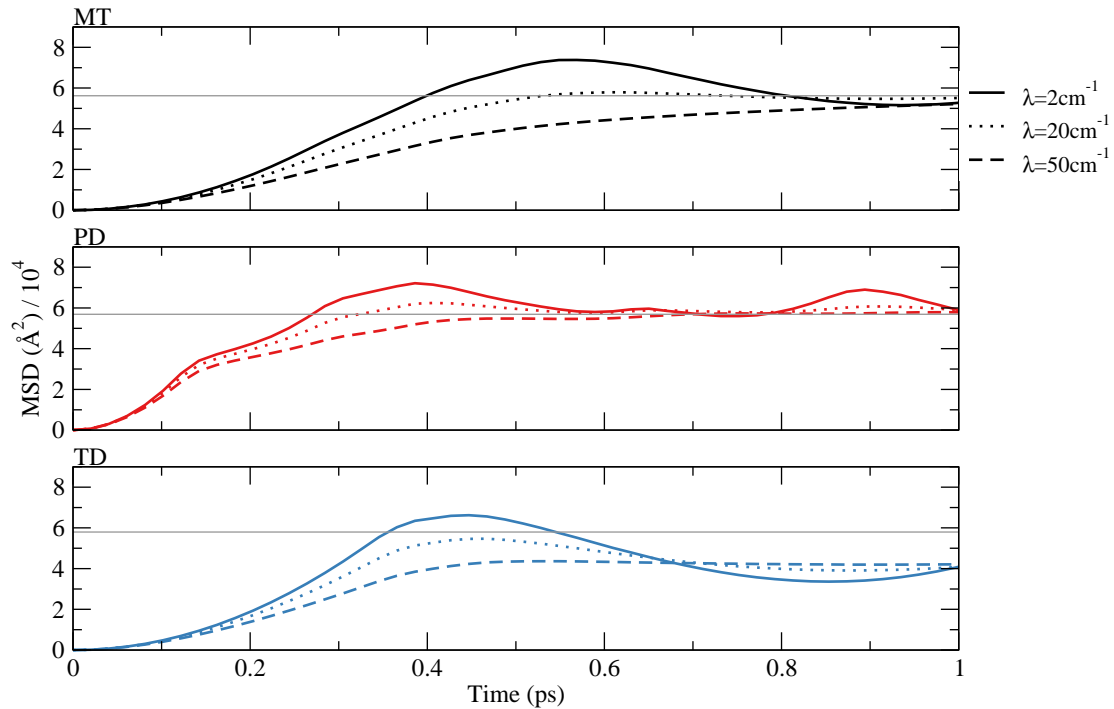
Figure 5.16: The real-time dynamics in three models: MT, PD, TD, in a cylinder with 101 rings with 4 dipoles per ring characterized by the MSD with an initial excitation on site 202 at room temperature ($T = 300K$). The parameters describing the Debye spectral density are, for the characteristic bath frequency (ω_c), $200cm^{-1}$. The straight line represents the MSD as calculated in the weak coupling limit.

From Figure 5.16 there is a departure from the larger radius as used by the Celardo group. The choice of the reduced radius allows for an easier extension of the length of the cylinder. This is relevant because the MSD calculation can be used to extract the diffusion constant of the exciton transport, if diffusive behaviour is shown as indicated when the MSD results are linear in time [79]. Even with a cylinder of 101 stacked rings, finite size effects can be observed. From the research completed by the Celardo group [45], it was observed that the natural (MT) model resulted in a larger coherence length in the weak coupling limit compared to the other models; determining the diffusion constant can provide succinct comparison if there is a relation to the transport in the models under study here. Since the dimension of the system is reduced (to just along

the length of the cylinder) in the study of the spread of the exciton, equation 5.2 is used for the calculation of the diffusion constant [79].

$$D = \frac{1}{2} \lim_{t \longrightarrow \infty} \frac{d\text{MSD}}{dt} \qquad (5.2)$$

Figure 5.17 depicts the MSD for the MT, TD and NN model for an increased system size of 401 rings, with an initial excitation on a single site in the middle of the cylinder. For the cylindrical models under study, with a radius of 4 Å, in the NN model each pigment will be coupled to the other pigments in the ring and, if applicable, will be coupled to one pigment from the ring above and below. A linear regime for the MSD is now observed for the transport of the exciton in these models and by extracting the first derivative, as shown in the bottom panel of Figure 5.17, the diffusion constant can be determined. Qualitatively, the MSD shows that the spread of the exciton is fastest in the TD model, followed by the MT and then the NN model, which has been artificially increased by a factor of 10 for better viewing on the plot. The NN model has the slowest spread of the exciton, emphasising the importance of the long-range coupling for the fast and efficient transfer of energy through the cylinder. This is supported by a similar trend in the diffusion constants from Table 5.2.

Model	Diffusion Constant ($\text{Å}^2/ps$)
MT	$3.69 \pm 0.07 \times 10^4$
TD	$4.6 \pm 0.1 \times 10^4$
NN	$1.68 \pm 0.05 \times 10^3$

Table 5.2: Diffusion constants for three cylindrical models composed of 401 rings with 4 dipoles per ring.

The lack of the PD model is explained with Figure 5.18. The spread of the exciton is fast within this model; even under these conditions, a cylinder with a length of 401 rings, finite size effects are observed within a simulation of 2 picoseconds. A reliable value for the diffusion constant was not able to be extracted due to the lack of an adequate linear regime in the first derivative of the MSD; a diffusion constant for the PD model is left for future simulations to reveal a more definitive and confident linear regime.
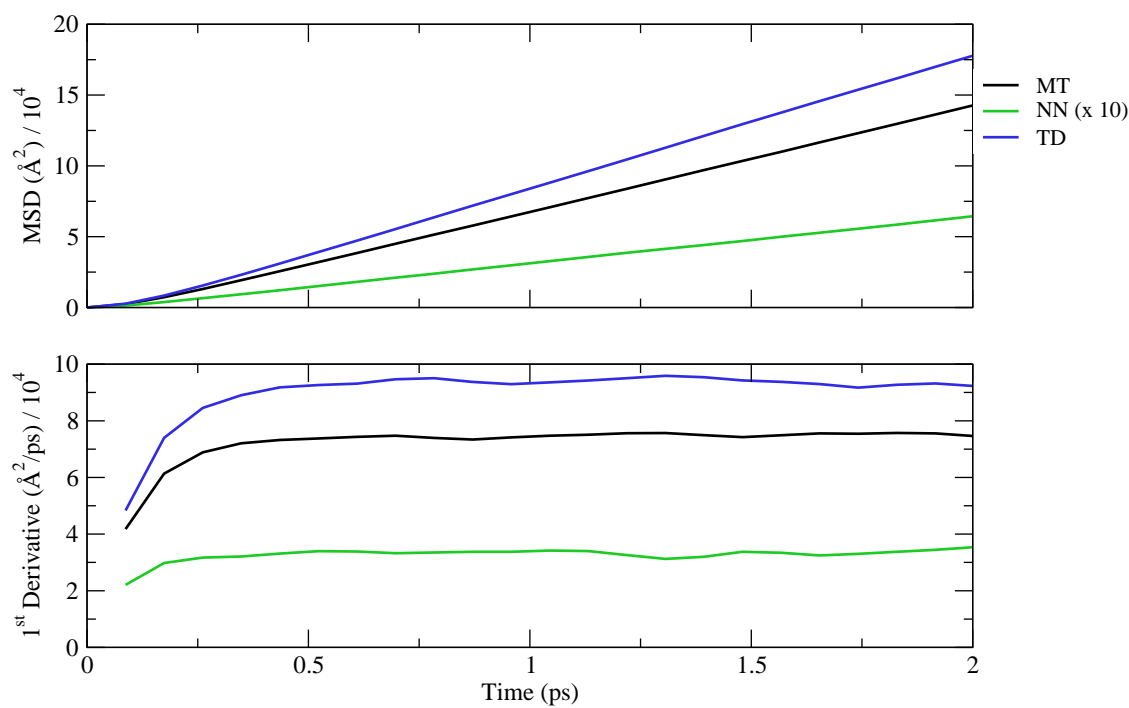
Figure 5.17: The real-time dynamics in three models: MT, NN, TD, in a cylinder with 401 rings with 4 dipoles per ring characterized by the MSD in the top panel with an initial excitation on site 802 at room temperature ($T = 300K$). The parameters describing the Debye spectral density are, for the characteristic bath frequency (ω_c), $200cm^{-1}$ and, for the reorganization energy (λ), $100cm^{-1}$. The bottom panel is the 1$^{\text{st}}$ derivative of the MSD for the three models. In the case of the NN model, these values have been scaled by 10 in order to provide easier viewing compared to the other models.
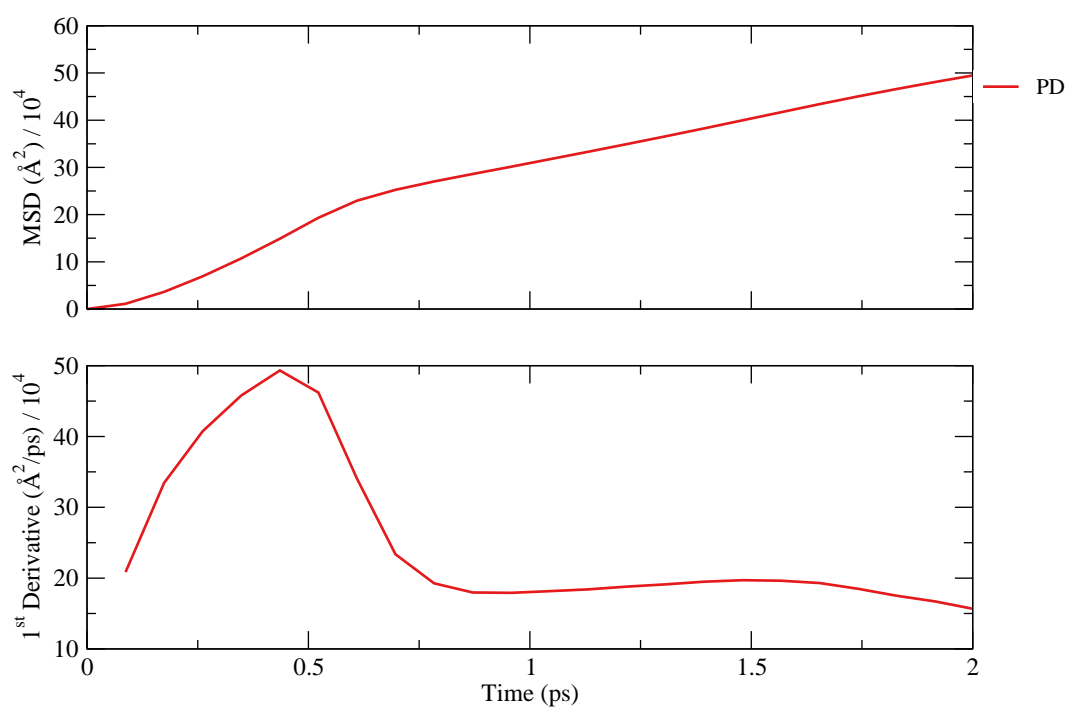
Figure 5.18: The real-time dynamics in the PD model, in a cylinder with 401 rings with 4 dipoles per ring characterized by the MSD in the top panel with an initial excitation on site 802 at room temperature ($T = 300K$. The bottom panel is the 1$^{\text{st}}$ derivative of the MSD for this model. The parameters describing the Debye spectral density are, for the characteristic bath frequency (ω_c), $200cm^{-1}$ and, for the reorganization energy (λ), $100cm^{-1}$.

The excitation energy transfer in the three arrangements of the pigments, along with the NN model, can be directly viewed in Figure 5.19, where the saturation of the colour indicates the population on a ring as a function of time. The populations are in the site basis but have undergone a log transformation for increased readability. The colourbar on the right shows only from 0 to -3 because this represents a population spread of between 1 and 0.001. The colours outside the scale correspond to ring populations of even smaller values. This alternative method for representing the data clearly reveals that the initial population on a single site in the ring quickly disperses in the next time step for all three models and is significantly slower for the NN model.

Out of the three arrangements of the dipoles (MT, TD or PD) the MT model has been demonstrated to exhibit the slowest spread of the exciton through the length of the cylinder. This result would indicate that speed is only one aspect in efficient and effective excitation energy transfer and that there are other benefits to this arrangement of dipoles not explored in this work, perhaps due to the lowest energy exciton state.

(a) MT Model

(b) TD Model

(c) PD Model

(d) NN Model
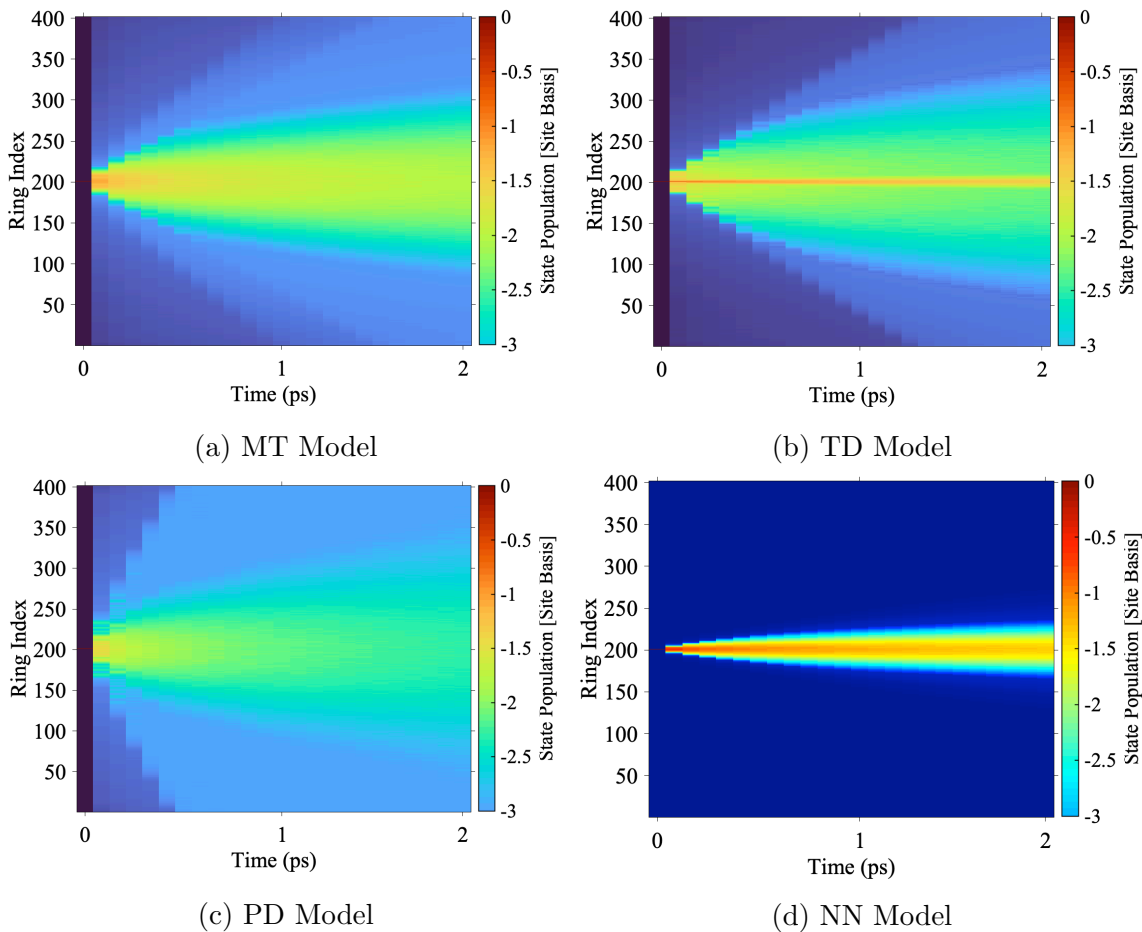
Figure 5.19: The real-time dynamics represented with colour in the four models: MT, TD, PD, and NN, in a cylinder with 401 rings with 4 dipoles per ring with an initial excitation on site 802 at room temperature ($T = 300K$). The parameters describing the Debye spectral density are, for the characteristic bath frequency (ω_c), $200cm^{-1}$ and, for the reorganization energy (λ), $100cm^{-1}$. The magnitude of the populations in log scale correspond to a particular colour. Instances where the population is zero or exceedingly small (as in the case of the NN model) are arbitrarily set to a very small negative value and represented by dark blue. The legend was chosen to focus on the rings with a significant population, values from 0 to -3 in log scale correspond to populations of 1 to 0.001; colour tones on the graphs not in the legend correspond to even smaller populations.

Figure 5.20 depicts the influence of the strength of the bath on the cylindrical system composed of 401 rings with 4 dipoles per ring. The affect of the larger reorganization energy is again shown to be effective in reducing the spread of the exciton even in a larger system. By increasing the number of rings in the system or the strength of the bath, to slow the dynamics, could result in observing the MSD as linear in time for the PD model.
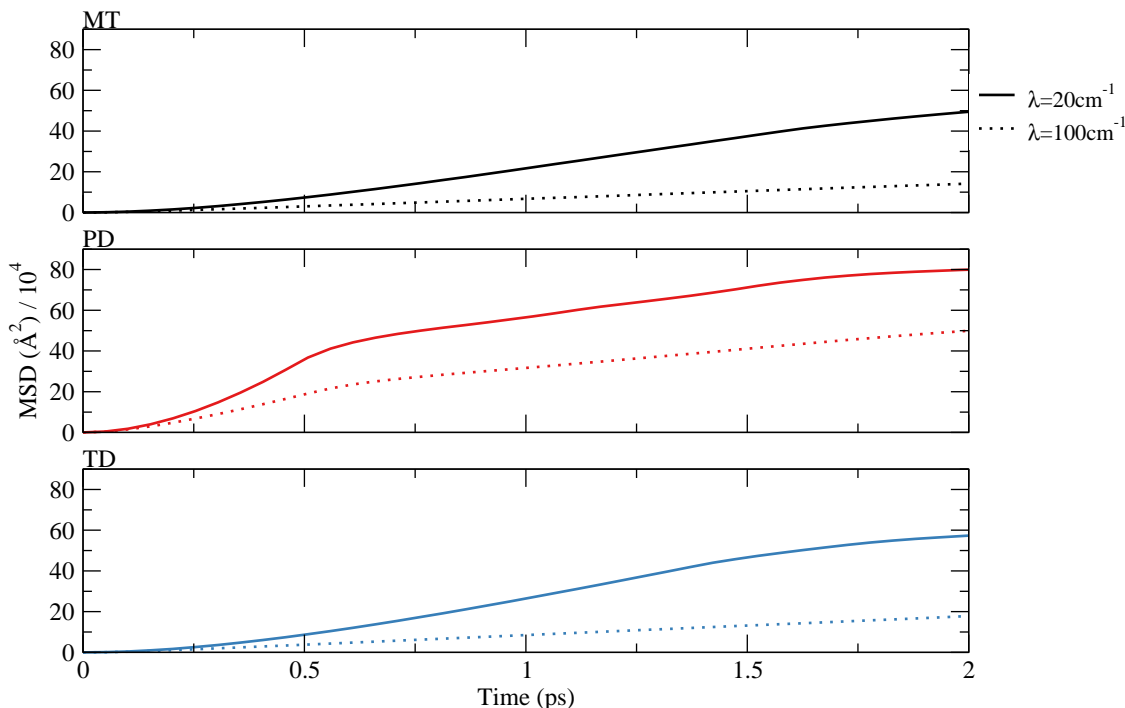
Figure 5.20: The real-time dynamics in three models: MT, PD, TD, in a cylinder with 401 rings with 4 dipoles per ring characterized by the MSD with an initial excitation on site 802 at room temperature ($T = 300K$). The parameters describing the Debye spectral density are, for the characteristic bath frequency (ω_c), $200cm^{-1}$.

From the application of the FBTS method to the three representative models for the chlorosome light harvesting complex the excitation energy transfer was studied and it was observed that the model representing the natural system resulted in the slowest spread of the exciton through the particular cylinder used. Again it can be observed that after the initial excitation on a single site of one ring the population

spreads the most to other rings in the PD model and continues to spread to more rings from there. The two systems studied in this chapter only represent a very simplified version of the chlorosome structure. However, it is clearly noted that the strength of the couplings between sites is a strong driver of the population dynamics of the system and increasing the influence of the bath slowed the spread. The excitation energy transfer depends clearly on the orientation and position of the dipoles. In order to more effectively make conclusions about the dynamics of excitation energy transfer in the chlorosome continued research must be made to expand the system under study, both in terms of the radius and the length of the cylinder.

Chapter 6

Conclusion And Outlook

In this thesis, the excitation energy transfer in a range of natural light harvesting complexes was explored and an analysis of the data provided by the FBTS method allowed for the mechanisms of transport to be detailed. In order to demonstrate that this method is capable of providing pertinent information about the real-time dynamics in these systems, a benchmark comparison was undertaken. The exciton dimer model provided a basis through which to understand how the physical parameters of the system affect the dynamics. This model was also used to support that the FBTS method provides an acceptable level of accuracy over a wide range of reorganisation energies at two characteristic bath frequencies. This was substantiated by an additional benchmark investigation completed on the 7-site FMO model, a natural light harvesting complex.

For the three light harvesting complexes that possess a protein scaffold, LHCII, CP26 and FMO, two initial excited sites at two temperatures were simulated. This allowed for the construction and comparison between the mechanisms of the excitation energy transfer. In general a flow from the highest to lowest energy sites for the exciton was observed. An alteration in the initial site resulted in a change in the sites involved in the transfer while a change in the temperature affected the magnitude in which sites were populated. Future directions would be to fully characterise the mechanisms that result from each initial site condition. It was observed that in the 7-site FMO model an initial excitation on site 1 resulted in a mechanism that involved a transient population on site 2, which possessed a higher site energy. An investigation on whether this behaviour is emulated in LHCII or CP26 could be conducted with an analysis of additional initial site conditions. Notably, for CP26 both initial conditions resulted in very similar mechanisms of transfer that lacked any significant participation from sites 3, 4, 5, 6 and 13; therefore, other site conditions could reveal instances where these sites are utilised for transfer. The excitation energy

transfer mechanisms presented in this thesis were based on an initial condition of a singly excited site. Changing the initial condition to an eigenstate of the system would present new mechanisms of transport to observe and compare.

The analysis of the excitation energy transfer in the chlorosome represents a promising application of this work. The spread of the exciton through three small cylindrical models were quantified. It was determined that the model based on a natural structure resulted in the slowest spread of the exciton. However, a model without long range coupling between pigments had even slower transfer. It would be important to ascertain whether or not this is observed for a model cylinder with a larger radius. In additional, another model representing a natural system, a representative cylindrical model of the wild type chlorosome, can provide an opportunity to further compare how the structure and orientation of the pigments affects the excitation energy transfer of the system.

The work on the chlorosome also served to demonstrate that the FBTS method can be used in the application of systems with many sites. Thus, it would be possible for future work to investigate a more realistic version of the system responsible for the primary steps of photosynthesis; to go beyond excitation energy transfer in isolated light harvesting complexes by linking multiple complexes together and incorporating the participation of reaction centre. As demonstrated from this thesis the bath has an important role in the excitation energy transfer in light harvesting systems. This work utilises the Debye spectral density approximation and the substitution of a more accurate bath will allow for the dynamics of the subsystem bath interaction to be captured more realistically. There are many avenues for further research to be completed using the FBTS method and the hope of this thesis is that an understanding of the excitation energy transfer in light harvesting complexes and the many different directions this work can continue to expand has been provided.

Appendix A

Code

An open source version of the code is available in the E-Cam repository at:

https://gitlab.e-cam2020.eu:10443/Quantum-Dynamics/FBTS_MPI

Appendix B

Numbering Scheme

In this thesis a simple numbering scheme was used to indicate specific sites in a light harvesting complex. Where this scheme differs from what is used in the literature (i.e. for LHCII and CP26), the following Tables contain the correlation between the two.

This Thesis	Literature
1	B601
2	A602
3	A603
4	A604
5	B605
6	B606
7	B607
8	B608
9	B609
10	A610
11	A611
12	A612
13	A613
14	A614

Table B.1: The intersection between the numbering schemes between this thesis and the literature for the LHCII monomer light harvesting complex [58].

This Thesis	Literature
1	B601
2	A602
3	A603
4	A604
5	B606
6	B607
7	B608
8	A609
9	A610
10	A611
11	A612
12	A613
13	A614

Table B.2: The intersection between the numbering schemes between this thesis and the literature for the CP26 light harvesting complex [59].

Appendix C

Subsystem Hamiltonian Data

In order to complete the simulations for the FBTS method the subsystem Hamiltonian corresponding to a particular light harvesting complex is required. This appendix collects the Hamiltonians used in the simulations for this thesis.

In this thesis the excitation energy transfer in the LHCII light harvesting complex was studied through a single monomer and in the full trimeric complex. The Hamiltonian used to calculate the dynamics in a monomer is provided in Table C.1. The H_{mono} and H_{inter} components used to construct the LHCII trimer Hamiltonian is provided in Tables C.2 and C.3.

	1	2	3	4	5	6	7	8	9	10	11	12	13	14
1	15889	49.64	-5.89	-2.51	0.77	-1.87	-2.49	2.78	3.79	-5.95	24.89	9.13	-10.79	3.59
2	49.64	15157	38.11	6.42	-0.71	5.6	7.13	-5.84	-19.25	-11.39	9.69	15.83	-4.96	0.69
3	-5.89	38.11	15287	-3.28	1.13	-8.89	1.23	6.72	96.66	12.97	-2.7	-0.76	2.68	-6.7
4	-2.51	6.42	-3.28	15460	3.35	104.56	35.93	-2.76	-7.28	-4.18	-3.8	4.67	2.12	-3.42
5	0.77	-0.71	1.13	3.35	15679	29.71	-4.47	-5.13	-0.77	1.61	1.33	-2.85	-1.4	0.37
6	-1.87	5.6	-8.89	104.56	29.71	15850	59.38	-4.99	-0.16	-3.28	-2.52	3.1	1.47	-2.16
7	-2.49	7.13	1.23	35.93	-4.47	59.38	15714	-4.43	-11.99	-0.14	-2.78	3.07	2.2	-3.25
8	2.78	-5.84	6.72	-2.76	-5.13	-4.99	-4.43	15761	36.07	61.97	4.35	-1.08	-2.01	1.3
9	3.79	-19.25	96.66	-7.28	-0.77	-0.16	-11.99	36.07	15721	3.86	4.3	-2.57	-2.92	2.33
10	-5.95	-11.39	12.97	-4.18	1.61	-3.28	-0.14	61.97	3.86	15073	-24.96	23.1	7.21	-1.55
11	24.89	9.69	-2.7	-3.8	1.33	-2.52	-2.78	4.35	4.3	-24.96	15112	126.92	-6.15	4.55
12	9.13	15.83	-0.76	4.67	-2.85	3.1	3.07	-1.08	-2.57	23.1	126.92	15094	-0.47	-0.18
13	-10.79	-4.96	2.68	2.12	-1.4	1.47	2.2	-2.01	-2.92	7.21	-6.15	-0.47	15174	-50.22
14	3.59	0.69	-6.7	-3.42	0.37	-2.16	-3.25	1.3	2.33	-1.55	4.55	-0.18	-50.22	15260

Table C.1: The subsystem Hamiltonian for the LHCII monomer light harvesting complex from Ref. [58], the units are cm^{-1}.

	2	3	10	11	12	8	9	1'	13	14	4	5	6	7
2	15157	38.11	-11.39	9.69	15.83	-5.84	-19.25	-0.35	-4.96	0.69	6.42	-0.71	5.60	7.13
3	38.11	15287	12.97	-2.70	-0.76	6.72	96.66	-0.71	2.68	-6.70	-3.28	1.13	-8.89	1.23
10	-11.39	12.97	15073	-24.96	23.10	61.97	3.86	-4.20	7.21	-1.55	-4.18	1.61	-3.28	-0.14
11	9.69	-2.70	-24.96	15112	126.92	4.35	4.30	-0.88	-6.15	4.55	-3.80	1.33	-2.52	-2.78
12	15.83	-0.76	23.10	126.92	15094	-1.08	-2.57	1.41	-0.47	-0.18	4.67	-2.85	3.10	3.07
8	-5.84	6.72	61.97	4.35	-1.08	15761	36.07	5.82	-2.01	1.30	-2.76	-5.13	-4.99	-4.43
9	-19.25	96.66	3.86	4.30	-2.57	36.07	15721	38.15	-2.92	2.33	-7.28	-0.77	-0.16	-11.99
1'	-0.35	-0.71	-4.20	-0.88	1.41	5.82	38.15	15889	0.90	0.17	2.69	-2.26	2.72	0.30
13	-4.96	2.68	7.21	-6.15	-0.47	-2.01	-2.92	0.90	15174	-50.22	2.12	-1.40	1.47	2.20
14	0.69	-6.70	-1.55	4.55	-0.18	1.30	2.33	0.17	-50.22	15260	-3.42	0.37	-2.16	-3.25
4	6.42	-3.28	-4.18	-3.80	4.67	-2.76	-7.28	2.69	2.12	-3.42	15460	3.35	104.56	35.93
5	-0.71	1.13	1.61	1.33	-2.85	-5.13	-0.77	-2.26	-1.40	0.37	3.35	15679	29.71	-4.47
6	5.60	-8.89	-3.28	-2.52	3.10	-4.99	-0.16	2.72	1.47	-2.16	104.56	29.71	15850	59.38
7	7.13	1.23	-0.14	-2.78	3.07	-4.43	-11.99	0.30	2.20	-3.25	35.93	-4.47	59.38	15714

Table C.2: The subsystem Hamiltonian for the LHCII monomer light harvesting complex from Ref. [52]. Used as H_{mono} in the construction of the Hamiltonian for the trimer. Due to the manner in which Ref. [52] organised this Hamiltonian a site in monomer 1, 2, 3 is indicated as site 1, 1', 1''. The units are cm^{-1}.

	2	3	10	11	12	8	9	1'	13	14	4	5	6	7
2"	1.11	5.22	0.76	-0.51	-0.51	-1.15	-2.33	0.22	-0.44	-2.51	1.15	-0.34	1.17	1.82
3"	8.14	-6.53	-2.05	-0.15	2.40	1.32	2.33	-1.45	-4.36	4.15	-0.50	0.50	-0.41	-0.97
10"	2.95	-0.91	-0.68	-1.13	1.14	0.50	0.68	-0.34	-1.19	0.70	-0.19	0.22	-0.23	-0.43
11"	0.55	-1.21	-0.36	-0.24	0.42	0.44	0.71	-0.09	0.22	0.81	-0.30	0.17	-0.36	-0.56
12"	-0.69	1.29	0.51	0.57	-0.29	-0.11	-0.41	0.35	-0.93	-0.76	-0.01	-0.04	0.10	0.20
8"	0.08	-0.54	0.54	2.70	-0.61	0.40	0.42	0.46	0.38	0.74	-0.59	0.04	-0.41	-0.47
9"	-10.66	0.23	2.25	4.63	-3.19	-0.23	-0.34	0.89	5.24	-4.57	-0.26	-0.23	-0.12	-0.00
1	49.64	-5.89	-5.95	24.89	9.13	2.78	3.79	-0.43	-10.79	3.59	-2.51	0.77	-1.87	-2.49
13"	-1.20	-0.48	0.07	0.45	-0.66	-0.17	-0.17	0.23	2.00	0.49	-0.25	-0.22	-0.23	0.22
14"	-0.86	-0.91	-0.01	0.29	-0.07	0.38	0.43	0.73	0.97	1.11	-0.68	0.12	-0.66	-0.68
4"	-0.90	2.56	0.54	0.27	-0.67	-0.71	-1.05	-0.25	-1.08	-3.91	0.87	-0.29	0.80	1.21
5"	0.66	-0.26	0.06	-0.32	0.48	0.22	0.18	0.16	-0.97	3.43	-0.49	0.07	-0.24	-0.34
6"	-0.82	2.80	0.25	-0.78	-0.36	-0.67	-0.99	-0.34	-0.89	-5.63	1.07	-0.20	0.82	1.20
7"	0.53	3.18	-0.20	-0.85	-0.43	-0.66	-0.94	-0.59	8.18	0.73	1.34	-0.20	0.88	1.51

Table C.3: The subsystem Hamiltonian for the intersite couplings between monomers in the LHCII light harvesting complex from Ref. [52]. Used as H_{inter} in the construction of the Hamiltonian for the trimer. Due to the manner in which Ref. [52] organised this Hamiltonian a site in monomer 1, 2, 3 is indicated as site 1, 1', 1". The units are cm^{-1}.

	1	2	3	4	5	6	7	8	9	10	11	12	13
1	15094	-57.22	7.04	2.56	2.08	-2.86	-3.19	5.18	3.54	-21.96	-1.49	4.46	0.20
2	-57.22	14593	40.94	6.15	6.53	-7.98	-7.46	26.86	-11.53	1.08	-12.46	-3.55	-0.75
3	7.04	40.94	14615	-6.15	-9.34	-5.05	2.37	-78.70	11.20	-1.91	2.71	5.10	5.76
4	2.56	6.15	-6.15	14734	36.87	-8.98	-1.96	4.97	-4.76	-4.56	-0.29	1.47	3.86
5	2.08	6.53	-9.34	36.87	14921	-14.14	-5.24	6.73	-2.02	-2.77	0.67	1.49	2.53
6	-2.86	-7.98	-5.05	-8.98	-14.14	14913	5.08	-19.25	-1.12	3.05	0.76	-4.47	-3.65
7	-3.19	-7.46	2.37	-1.96	-5.24	5.08	14951	-29.86	52.52	6.53	0.05	-2.77	-1.44
8	5.18	26.86	-78.70	4.97	6.73	-19.25	-29.86	14478	6.39	-6.29	-1.73	4.49	2.67
9	3.54	-11.53	11.20	-4.76	-2.02	-1.12	52.52	6.39	14636	-40.68	-20.16	6.20	0.66
10	-21.96	1.08	-1.91	-4.56	-2.77	3.05	6.53	-6.29	-40.68	14750	-95.75	-2.33	-2.89
11	-1.49	-12.46	2.71	-0.29	0.67	0.76	0.05	-1.73	-20.16	-95.75	14697	3.29	0.36
12	4.46	-3.55	5.10	1.47	1.49	-4.47	-2.77	4.49	6.20	-2.33	3.29	14492	58.97
13	0.20	-0.75	5.76	3.86	2.53	-3.65	-1.44	2.67	0.66	-2.89	0.36	58.97	14717

Table C.4: The subsystem Hamiltonian for the CP26 light harvesting complexes from Ref. [59], the units are cm^{-1}.

The subsystem Hamiltonian for the 7-site and 8-site FMO model is provided in Tables C.4 and C.6, respectively. The 8-site FMO model was used as the H_{mono} to construct the FMO trimer Hamiltonian and the intersite couplings (H_{inter}) between monomers in provided in Table C.7.

	1	2	3	4	5	6	7
1	12410	-87.7	5.5	-5.9	6.7	-13.7	-9.9
2	-87.7	12530	30.8	8.2	0.7	11.8	4.3
3	5.5	30.8	12210	-53.5	-2.2	-9.6	6.0
4	-5.9	8.2	-53.5	12320	-70.7	-17.0	-63.3
5	6.7	0.7	-2.2	-70.7	12480	81.1	-1.3
6	-13.7	11.8	-9.6	-17.0	81.1	12630	39.7
7	-9.9	4.3	6.0	-63.3	-1.3	39.7	12440

Table C.5: The subsystem Hamiltonian for the 7-site FMO monomer light harvesting complex as used in Ref. [28] and from Ref. [76], the units are cm^{-1}.

	1	2	3	4	5	6	7	8
1	186	-80.3	3.5	-4	4.5	-10.2	-4.9	21
2	-80.3	81	23.5	6.7	0.5	7.5	1.5	3.3
3	3.5	23.5	0	-49.8	-1.5	-6.5	1.2	0.7
4	-4	6.7	-49.8	113	-63.4	-13.3	-42.2	-1.2
5	4.5	0.5	-1.5	-63.4	65	55.8	4.7	2.8
6	-10.2	7.5	-6.5	-13.3	55.8	89	33	-7.3
7	-4.9	1.5	1.2	-42.2	4.7	33	492	-8.7
8	21	3.3	0.7	-1.2	2.8	-7.3	-8.7	218

Table C.6: The subsystem Hamiltonian for the 8-site FMO monomer light harvesting complex as used in Ref. [47] and from Ref. [77]. Used alone and as H_{mono} in the construction of the Hamiltonian for the FMO trimer. The units are cm^{-1}.

	1	2	3	4	5	6	7	8
1	1	3	-0.6	0.7	2.3	1.5	0.9	0.1
2	1.5	-0.4	-2.5	-1.5	7.4	5.2	1.5	0.7
3	1.4	0.1	-2.7	5.7	4.6	2.3	4	0.8
4	0.3	0.5	0.7	1.9	-0.6	-0.4	1.9	-0.8
5	0.7	0.9	1.1	-0.1	1.8	0.1	-0.7	1.3
6	0.1	0.7	0.8	1.4	-1.4	-1.5	1.6	-1
7	0.3	0.2	-0.7	4.8	-1.6	0.1	5.7	-2.3
8	0.1	0.6	1.5	-1.1	4	-3.1	-5.2	3.6

Table C.7: The subsystem Hamiltonian for the intersite couplings between monomers in the FMO light harvesting complex as used in Ref. [47] and from Ref. [78]. Used as H_{inter} in the construction of the Hamiltonian for the trimer. The units are cm^{-1}.

References

[1] L. A. Baker and S. Habershon, "Photosynthesis, pigment-protein complexes and electronic energy transport: simple models for complicated processes," *Sci. Prog.*, vol. 100, no. 3, pp. 313–330, 2017.

[2] R. E. Blankenship, *Molecular mechanisms of photosynthesis*. Oxford : Blackwell Science, 2002.

[3] R. Croce and H. van Amerongen, "Natural strategies for photosynthetic light harvesting," *Nat. Chem. Biol.*, vol. 10, no. 7, pp. 492–501, 2014.

[4] S. F. Huelga and M. B. Plenio, "Vibrations, quanta and biology," *Contemp. Phys.*, vol. 54, no. 4, pp. 181–207, 2013.

[5] S. J. Jang and B. Mennucci, "Delocalized excitons in natural light-harvesting complexes," *Rev. Mod. Phys.*, vol. 90, p. 035003, 2018.

[6] Y.-C. Cheng and G. R. Fleming, "Dynamics of light harvesting in photosynthesis," *Annu. Rev. Phys. Chem.*, vol. 60, no. 1, p. 241–262, 2009.

[7] F. Fassioli, R. Dinshaw, P. C. Arpin, and G. D. Scholes, "Photosynthetic light harvesting: excitons and coherence," *J. R. Soc. Interface*, vol. 11, no. 92, p. 20130901, 2014.

[8] J. Cao, R. J. Cogdell, D. F. Coker, H.-G. Duan, J. Hauer, U. Kleinekathöfer, T. L. C. Jansen, T. Mančal, R. J. D. Miller, J. P. Ogilvie, V. I. Prokhorenko, T. Renger, H.-S. Tan, R. Tempelaar, M. Thorwart, E. Thyrhaug, S. Westenhoff, and D. Zigmantas, "Quantum biology revisited," *Sci. Adv.*, vol. 6, no. 14, 2020.

[9] T. Mirkovic, E. E. Ostroumov, J. M. Anna, R. van Grondelle, Govindjee, and G. D. Scholes, "Light absorption and energy transfer in the antenna complexes of photosynthetic organisms," *Chem. Rev.*, vol. 117, no. 2, pp. 249–293, 2017.

[10] H. Scheer, *An Overview of Chlorophylls and Bacteriochlorophylls: Biochemistry, Biophysics, Functions and Applications*, pp. 1–26. Dordrecht: Springer Netherlands, 2006.

[11] H. K. Lichtenthaler, *[34] Chlorophylls and carotenoids: Pigments of photosynthetic biomembranes*, vol. 148, p. 350–382. Academic Press, 1987.

[12] X. Wei, X. Su, P. Cao, X. Liu, W. Chang, M. Li, X. Zhang, and Z. Liu, "Structure of spinach photosystem II-LHCII supercomplex at 3.2 Å resolution," *Nature*, vol. 534, no. 7605, pp. 69–74, 2016.

[13] Z. Liu, H. Yan, K. Wang, T. Kuang, J. Zhang, L. Gui, X. An, and W. Chang, "Crystal structure of spinach major light-harvesting complex at 2.72 Å resolution," *Nature*, vol. 428, no. 6980, pp. 287–292, 2004.

[14] P. Qian, C. A. Siebert, P. Wang, D. P. Canniffe, and C. N. Hunter, "Cryo-EM structure of the *Blastochloris viridis* LH1–RC complex at 2.9 Å," *Nature*, vol. 556, no. 7700, p. 203–208, 2018.

[15] E. Wientjes, G. Roest, and R. Croce, "From red to blue to far-red in Lhca4: how does the protein modulate the spectral properties of the pigments?," *Biochim. Biophys. Acta, Bioenerg.*, vol. 1817, no. 5, pp. 711–717, 2012.

[16] R. Saer, G. S. Orf, X. Lu, H. Zhang, M. J. Cuneo, D. A. Myles, and R. E. Blankenship, "Perturbation of bacteriochlorophyll molecules in Fenna–Matthews–Olson protein complexes through mutagenesis of cysteine residues," *Biochim. Biophys. Acta, Bioenerg.*, vol. 1857, no. 9, pp. 1455–1463, 2016.

[17] E. Wientjes, H. van Amerongen, and R. Croce, "Quantum Yield of Charge Separation in Photosystem II: Functional Effect of Changes in the Antenna Size upon Light Acclimation," *J. Phys. Chem. B.*, vol. 117, no. 38, pp. 11200–11208, 2013.

[18] V. May, *Charge and energy transfer dynamics in molecular systems.* Wiley-VCH, 2nd, rev.enl. edition.. ed., 2004.

[19] T. Förster, "Zwischenmolekulare energiewanderung und fluoreszenz," *Annalen der Physik*, vol. 437, no. 1-2, pp. 55–75, 1948.

[20] A. G. Redfield, "On the theory of relaxation processes," *IBM J. Res. Dev.*, vol. 1, no. 1, pp. 19–31, 1957.

[21] A. Redfield, "The Theory of Relaxation Processes," *Adv. Magn. Opt. Reson.*, vol. 1, no. C, pp. 1–32, 1965.

[22] V. I. Novoderezhkin and R. van Grondelle, "Physical origins and models of energy transfer in photosynthetic light-harvesting," *Phys. Chem. Chem. Phys.*, vol. 12, no. 27, p. 7352–7365, 2010.

[23] R. van Grondelle and V. I. Novoderezhkin, "Energy transfer in photosynthesis: experimental insights and quantitative models," *Phys. Chem. Chem. Phys.*, vol. 8, no. 7, p. 793–807, 2006.

[24] A. Ishizaki and G. R. Fleming, "On the adequacy of the Redfield equation and related approaches to the study of quantum dynamics in electronic energy transfer," *J. Chem. Phys.*, vol. 130, no. 23, p. 234110, 2009.

[25] A. Ishizaki and G. R. Fleming, "Unified treatment of quantum coherent and incoherent hopping dynamics in electronic energy transfer: Reduced hierarchy equation approach," *J. Chem. Phys.*, vol. 130, no. 23, p. 234111, 2009.

[26] M. Yang and G. R. Fleming, "Influence of phonons on exciton transfer dynamics: comparison of the Redfield, Förster, and modified Redfield equations," *Chem. Phys.*, vol. 275, no. 1, pp. 355–372, 2002.

[27] A. Ishizaki, T. Calhoun, G. Schlau-Cohen, and G. Fleming, "Quantum coherence and its interplay with protein environments in photosynthetic electronic energy transfer," *Phys. Chem. Chem. Phys.*, vol. 12, no. 27, p. 7319–7337, 2010.

[28] A. Ishizaki and G. R. Fleming, "Theoretical examination of quantum coherence in a photosynthetic system at physiological temperature," *PNAS*, vol. 106, no. 41, pp. 17255–17260, 2009.

[29] D. M. Wilkins and N. S. Dattani, "Why Quantum Coherence Is Not Important in the Fenna–Matthews–Olsen Complex," *J. Chem. Theory Comput.*, vol. 11, no. 7, pp. 3411–3419, 2015.

[30] C.-Y. Hsieh and R. Kapral, "Nonadiabatic dynamics in open quantum-classical systems: Forward-backward trajectory solution," *J. Chem. Phys.*, vol. 137, no. 22, p. 22A507, 2012.

[31] C.-Y. Hsieh and R. Kapral, "Analysis of the forward-backward trajectory solution for the mixed quantum-classical Liouville equation," *J. Chem. Phys.*, vol. 138, no. 13, p. 134110, 2013.

[32] A. Kelly, "Exciton dissociation and charge separation at donor–acceptor interfaces from quantum-classical dynamics simulations," *Faraday Discuss.*, vol. 221, pp. 547–563, 2020.

[33] M. Rätsep and A. Freiberg, "Electron–phonon and vibronic couplings in the FMO bacteriochlorophyll a antenna complex studied by difference fluorescence line narrowing," *J. Lumin.*, vol. 127, no. 1, pp. 251–259, 2007.

[34] M. K. Lee and D. F. Coker, "Modeling electronic-nuclear interactions for excitation energy transfer processes in light-harvesting complexes," *J. Phys. Chem. Lett.*, vol. 7, no. 16, pp. 3171–3178, 2016.

[35] M. K. Lee, P. Huo, and D. F. Coker, "Semiclassical path integral dynamics: Photosynthetic energy transfer with realistic environment interactions," *Annu. Rev. Phys. Chem.*, vol. 67, no. 1, pp. 639–668, 2016.

[36] S. Kundu and N. Makri, "Real-time path integral simulation of exciton-vibration dynamics in light-harvesting bacteriochlorophyll aggregates," *J. Phys. Chem. Lett.*, vol. 11, no. 20, pp. 8783–8789, 2020.

[37] A. Kell, X. Feng, M. Reppert, and R. Jankowiak, "On the Shape of the Phonon Spectral Density in Photosynthetic Complexes," *J. Phys. Chem. B*, vol. 117, no. 24, pp. 7317–7323, 2013.

[38] H. Wang, X. Song, D. Chandler, and W. H. Miller, "Semiclassical study of electronically nonadiabatic dynamics in the condensed-phase: Spin-boson problem with debye spectral density," *J. Chem. Phys.*, vol. 110, no. 10, pp. 4828–4840, 1999.

[39] G. Tao and W. H. Miller, "Semiclassical description of electronic excitation population transfer in a model photosynthetic system," *J. Phys. Chem. Lett.*, vol. 1, no. 6, pp. 891–894, 2010.

[40] R. Kapral and G. Ciccotti, "Mixed quantum-classical dynamics," *J. Chem. Phys.*, vol. 110, no. 18, pp. 8919–8929, 1999.

[41] R. Kapral, "Quantum dynamics in open quantum-classical systems," *J. Phys. Condens. Matter*, vol. 27, no. 7, p. 073201, 2015.

[42] C.-Y. Hsieh and R. Kapral, "Correlation Functions in Open Quantum-Classical Systems," *Entropy*, vol. 16, no. 1, pp. 200–220, 2014.

[43] G. Stock and M. Thoss, "Semiclassical Description of Nonadiabatic Quantum Dynamics," *Phys. Rev. Lett.*, vol. 78, pp. 578–581, 1997.

[44] F. Martinez and G. Hanna, "Assessment of approximate solutions of the quantum-classical Liouville equation for dynamics simulations of quantum subsystems embedded in classical environments," *Mol. Simul.*, vol. 41, no. 1-3, pp. 107–122, 2015.

[45] M. Gullì, A. Valzelli, F. Mattiotti, M. Angeli, F. Borgonovi, and G. L. Celardo, "Macroscopic coherence as an emergent property in molecular nanotubes," *New J. Phys.*, vol. 21, no. 1, p. 013019, 2019.

[46] K. Claridge, D. Padula, and A. Troisi, "On the arrangement of chromophores in light harvesting complexes: chance *versus* design," *Faraday Discuss.*, vol. 221, pp. 133–149, 2020.

[47] S. J. Cotton and W. H. Miller, "A symmetrical quasi-classical windowing model for the molecular dynamics treatment of non-adiabatic processes involving many electronic states," *J. Chem. Phys.*, vol. 150, no. 10, p. 104101, 2019.

[48] Y. Braver, L. Valkunas, and A. Gelzinis, "Benchmarking the forward–backward trajectory solution of the quantum-classical Liouville equation," *J. Chem. Phys.*, vol. 152, no. 21, p. 214116, 2020.

[49] X. Gao, M. A. C. Saller, Y. Liu, A. Kelly, J. O. Richardson, and E. Geva, "Benchmarking Quasiclassical Mapping Hamiltonian Methods for Simulating Electronically Nonadiabatic Molecular Dynamics," *J. Chem. Theory Comput.*, vol. 16, no. 5, pp. 2883–2895, 2020.

[50] G. S. Schlau-Cohen, T. R. Calhoun, N. S. Ginsberg, E. L. Read, M. Ballottari, R. Bassi, R. van Grondelle, and G. R. Fleming, "Pathways of Energy Flow in LHCII from Two-Dimensional Electronic Spectroscopy," *J. Phys. Chem. B*, vol. 113, no. 46, p. 15352–15363, 2009.

[51] J. Wu, Z. Tang, Z. Gong, J. Cao, and S. Mukamel, "Minimal Model of Quantum Kinetic Clusters for the Energy-Transfer Network of a Light-Harvesting Protein Complex," *J. Phys. Chem. Lett.*, vol. 6, no. 7, p. 1240–1245, 2015.

[52] V. Novoderezhkin, A. Marin, and R. van Grondelle, "Intra- and inter-monomeric transfers in the light harvesting LHCII complex: the Redfield–Förster picture," *Phys. Chem. Chem. Phys.*, vol. 13, pp. 17093–17103, 2011.

[53] V. I. Novoderezhkin, M. A. Palacios, H. van Amerongen, and R. van Grondelle, "Energy-Transfer Dynamics in the LHCII Complex of Higher Plants: Modified Redfield Approach," *J. Phys. Chem. B*, vol. 108, no. 29, p. 10363–10375, 2004.

[54] T. Renger, M. Madjet, A. Knorr, and F. Müh, "How the molecular structure determines the flow of excitation energy in plant light-harvesting complex II," *J. Plant Physiol.*, vol. 168, no. 12, p. 1497–1509, 2011.

[55] W. C. Pfalzgraff, A. Montoya-Castillo, A. Kelly, and T. E. Markland, "Efficient construction of generalized master equation memory kernels for multi-state systems from nonadiabatic quantum-classical dynamics," *J. Chem. Phys.*, vol. 150, no. 24, p. 244109, 2019.

[56] J. J. J. Roden, D. I. G. Bennett, and K. B. Whaley, "Long-range energy transport in photosystem II," *J. Chem. Phys.*, vol. 144, no. 24, p. 245101–245101, 2016.

[57] W. Humphrey, A. Dalke, and K. Schulten, "VMD – Visual Molecular Dynamics," *J. Mol. Graph.*, vol. 14, pp. 33–38, 1996.

[58] C. Kreisbeck, T. Kramer, and A. Aspuru-Guzik, "Scalable High-Performance Algorithm for the Simulation of Exciton Dynamics. Application to the Light-Harvesting Complex II in the Presence of Resonant Vibrational Modes," *J. Chem. Theory Comput.*, vol. 10, no. 9, pp. 4045–4054, 2014.

[59] D. V. Khokhlov, A. S. Belov, and V. V. Eremin, "Exciton states and optical properties of the CP26 photosynthetic protein," *Comput. Biol. Chem.*, vol. 72, pp. 105–112, 2018.

[60] J. T. Beatty, J. Overmann, M. T. Lince, A. K. Manske, A. S. Lang, R. E. Blankenship, C. L. V. Dover, T. A. Martinson, F. G. Plumley, and B. B. Buchanan, "An obligately photosynthetic bacterial anaerobe from a deep-sea hydrothermal vent," *PNAS*, vol. 102, no. 26, pp. 9306–9310, 2005.

[61] J. Overmann, H. Cypionka, and N. Pfennig, "An extremely low-light-adapted phototrophic sulfur bacterium from the black sea," *Limnol. Oceanogr.*, vol. 37, no. 1, pp. 150–155, 1992.

[62] G. S. Orf and R. E. Blankenship, "Chlorosome antenna complexes from green photosynthetic bacteria," *Photosynth. Res.*, vol. 116, no. 2, p. 315–331, 2013.

[63] G. T. Oostergetel, H. van Amerongen, and E. J. Boekema, "The chlorosome: a prototype for efficient light harvesting in photosynthesis," *Photosynth. Res.*, vol. 104, p. 245–255, Jun 2010.

[64] J. Dostál, J. Pšenčík, and D. Zigmantas, "In situ mapping of the energy flow through the entire photosynthetic apparatus," *Nat. Chem.*, vol. 8, no. 7, p. 705–710, 2016.

[65] D. Tronrud, J. Wen, L. Gay, and R. Blankenship, "The structural basis for the difference in absorbance spectra for the FMO antenna protein from various green sulfur bacteria," *Photosynth. Res.*, vol. 100, no. 2, pp. 79–87, 2009.

[66] S. Ganapathy, G. T. Oostergetel, P. K. Wawrzyniak, M. Reus, A. G. M. Chew, F. Buda, E. J. Boekema, D. A. Bryant, A. R. Holzwarth, H. J. M. de Groot, and E. Gantt, "Alternating *syn-anti* bacteriochlorophylls form concentric helical nanotubes in chlorosomes," *PNAS*, vol. 106, no. 21, pp. 8525–8530, 2009.

[67] N. P. D. Sawaya, J. Huh, T. Fujita, S. K. Saikin, and A. Aspuru-Guzik, "Fast Delocalization Leads To Robust Long-Range Excitonic Transfer in a Large Quantum Chlorosome Model," *Nano Lett.*, vol. 15, no. 3, p. 1722–1729, 2015.

[68] R. E. Fenna and B. W. Matthews, "Chlorophyll arrangement in a bacteriochlorophyll protein from Chlorobium limicola," *Nature*, vol. 258, no. 5536, pp. 573–577, 1975.

[69] A. Somoza Márquez, L. Chen, K. Sun, and Y. Zhao, "Probing ultrafast excitation energy transfer of the chlorosome with exciton–phonon variational dynamics," *Phys. Chem. Chem. Phys.*, vol. 18, no. 30, p. 20298–20311, 2016.

[70] T. Balaban, "Tailoring porphyrins and chlorins for self-assembly in biomimetic artificial antenna systems," *Acc. Chem. Res.*, vol. 38, no. 8, pp. 612–623, 2005.

[71] M. Schmidt am Busch, F. Müh, M. El-Amine Madjet, and T. Renger, "The Eighth Bacteriochlorophyll Completes the Excitation Energy Funnel in the FMO Protein," *J. Phys. Chem. Lett.*, vol. 2, p. 93–98, Jan 2011.

[72] J. Wen, H. Zhang, M. L. Gross, R. E. Blankenship, and G. R. Fleming, "Membrane orientation of the FMO Antenna Protein from *Chlorobaculum Tepidum* as determined by mass spectrometry-based footprinting," *PNAS*, vol. 106, no. 15, pp. 6134–6139, 2009.

[73] S. J. Cotton and W. H. Miller, "The Symmetrical Quasi-Classical Model for Electronically Non-Adiabatic Processes Applied to Energy Transfer Dynamics in Site-Exciton Models of Light-Harvesting Complexes," *J. Chem. Theory Comput.*, vol. 12, no. 3, p. 983–991, 2016.

[74] H. W. Kim, A. Kelly, J. W. Park, and Y. M. Rhee, "All-Atom Semiclassical Dynamics Study of Quantum Coherence in Photosynthetic Fenna–Matthews–Olson Complex," *J. Am. Chem. Soc.*, vol. 134, no. 28, p. 11640–11651, 2012.

[75] A. Kelly and Y. Rhee, "Mixed quantum-classical description of excitation energy transfer in a model fenna-matthews-olsen complex," *J. Phys. Chem. Lett.*, vol. 2, no. 7, pp. 808–812, 2011.

[76] J. Adolphs and T. Renger, "How Proteins Trigger Excitation Energy Transfer in the FMO Complex of Green Sulfur Bacteria," *Biophys. J.*, vol. 91, no. 8, pp. 2778–97, 2006.

[77] C. Olbrich, T. L. C. Jansen, J. Liebers, M. Aghtar, J. Strümpfer, K. Schulten, J. Knoester, and U. Kleinekathöfer, "From Atomistic Modeling to Excitation Transfer and Two-Dimensional Spectra of the FMO Light-Harvesting Complex," *J. Phys. Chem. B*, vol. 115, no. 26, p. 8609–8621, 2011.

[78] G. Ritschel, J. Roden, W. T. Strunz, A. Aspuru-Guzik, and A. Eisfeld, "Absence of Quantum Oscillations and Dependence on Site Energies in Electronic Excitation Transfer in the Fenna–Matthews–Olson Trimer," *J. Phys. Chem. Lett.*, vol. 2, no. 22, p. 2912–2917, 2011.

[79] L. Wang, D. Beljonne, L. Chen, and Q. Shi, "Mixed quantum-classical simulations of charge transport in organic materials: Numerical benchmark of the Su-Schrieffer-Heeger model," *J. Chem. Phys.*, vol. 134, no. 24, p. 244116, 2011.